UNIVERSITÀ DEGLI STUDI DI TRIESTE

UNIVERSITÀ DEGLI STUDI DI TRIESTE

XXXVIII CICLO DEL DOTTORATO DI RICERCA IN

PhD in Physics

Finanziato dall'Unione europea - NextGenerationEU
Funded by the European Union - NextGenerationEU

National Quantum Science and Technology Institute - PNRR

QUANTUM GRAVIMETERS FOR GEOPHYSICAL APPLICATIONS

Settore scientifico-disciplinare:02/PHYS-02

DOTTORANDO
IVALDEVINGLES RODRIGRES DE SOUZA JUNIOR

COORDINATORE

PROF. FRANCESCO LONGO

SUPERVISORE DI TESI

PROF. ANDREA TROMBETTONI

CO-SUPERVISORE DI TESI
PROF. CARLA BRAITENBERG

ANNO ACCADEMICO 2024/2025

Finanziato dall'Unione europea NextGenerationEU | Ministero dell'Università e della Ricerca | Italiadomani PIANO NAZIONALE DI RIPRESA E RESILIENZA | UNIVERSITÀ DEGLI STUDI DI TRIESTE

To all my friends, professors, and family,
who supported me throughout this journey.

- Rodrigues

Abstract

Quantum gravimeters based on atom interferometry represent a new generation of gravity sensors, combining absolute measurements, high long-term stability, and high sensitivity. These characteristics make them particularly attractive for geophysical applications, where the detection of small gravity variations is essential for investigating subsurface mass distributions and temporal processes. In this Thesis, the operating principles of quantum gravimeters are presented in a pedagogical manner, bridging the gap between the quantum mechanical description of atom interferometry and its practical use in geophysics. The Mach–Zehnder atom interferometer configuration is analyzed in detail, including the role of Raman laser pulses, phase accumulation, and the influence of gravitational acceleration on the interferometric signal. Finally, the applicability of quantum gravimeters to geophysical problems is investigated through forward gravimetric modeling and inverse methods for density estimation. Numerical simulations based on synthetic models are used to assess the capability of quantum gravimeters to resolve subsurface density variations, including scenarios involving fluid substitution and instrumental drift. The results demonstrate that quantum gravimeters have the potential to significantly enhance the resolution and reliability of gravity-based geophysical investigations, opening new perspectives for monitoring geological, hydrological, and environmental processes.

Keywords: Quantum gravimeter; Atom interferometry; Quantum sensing; Geophysical applications.

Contents

Chapter 1

Gravimeters: Evolution, Operating Principles and Classification

1.1 Introduction

A gravimeter is an instrument used to measure the local acceleration of the Earth's gravity with high precision. This acceleration is not constant, since the gravitational field varies from one location to another due to the influence of several factors, such as local topography, subsurface mass distribution, and ocean tides (Blakely, 1995; Telford et al., 1990).

The acceleration of gravity is traditionally expressed in meters per second squared ($\mathrm{m\,s^{-2}}$) in the International System of Units (SI). However, in geodesy and geophysics, the "Gal" from the CGS (centimeter–gram–second) system of units is commonly used, such that $1\,\mathrm{Gal} = 1\,\mathrm{cm\,s^{-2}}$. In practice, particularly in high-precision measurements, derived units are employed, most notably the milliGal ($1\,\mathrm{mGal} = 10^{-5}\,\mathrm{m\,s^{-2}}$) and the microGal ($1\,\mu\mathrm{Gal} = 10^{-8}\,\mathrm{m\,s^{-2}}$) (Niebauer, 2007; Pettersen, 2016).

Accuracy in gravity measurements is essential for a wide range of applications, including geophysics, geology, and environmental monitoring. High-precision gravimetric data enable the detection of geological anomalies, such as mineral deposits and hydrocarbon reservoirs (Chen et al., 2015; Doyle, 1990; Smith, 1985; Villalobos et al., 2008), as well as the investigation of plate tectonics, including plate motions and crustal deformations (Bowin, 1991; Mohieldain et al., 2025). Gravimetry also plays a fundamental role in monitoring environmental changes, such as sea-level rise and the melting of ice sheets (Kumar, 2011; Zemp et al., 2025). In addition, in civil engineering, accurate gravity measurements contribute to the assessment of load dis-

tribution and the stability of large-scale structures (Arzi, 2006; Perez-Gracia et al., 2016). Consequently, modern high-accuracy instruments, such as quantum gravimeters, enable the detection of minute variations in the gravitational field, thereby supporting more detailed and reliable investigations across multiple scientific and engineering disciplines.

1.2 Evolution of Gravimeters

The earliest gravity measurements throughout history were carried out in a rudimentary manner, and the understanding of gravity gradually consolidated with advances in theoretical and instrumental physics. Galileo Galilei was a pioneer in the experimental study of gravity, and Isaac Newton (17th century) established the universal law of gravitation; however, at that time, precise quantitative measurements of gravity were still very limited.

Accurate measurements of gravitational acceleration only became feasible from the nineteenth century onward. During this period, the gravitational pendulum became established as one of the first devices employed for the determination of g (Nabighian et al., 2005). Subsequently, the development of instruments based on static equilibrium, such as torsion balances, represented a major advancement for geophysical applications (Mohieldain et al., 2025).

The operating principle of the torsion balance is based on the twisting of a wire or elastic fiber when subjected to a torque, as classically demonstrated in the experiments of Henry Cavendish in the late eighteenth century (Cavendish, 1798). When an external force acts on an object suspended by a torsion wire, the wire twists in response to this force. The amplitude of the torsion is proportional to the magnitude of the applied force and can be quantified by measuring the torsion angle.

The basic configuration of a torsion balance consists of a very thin and flexible wire, typically made of metallic material, suspended at the center of a rigid support. The wire is fixed at its upper end, while a small mass or rigid bar (usually a metallic rod) is attached to its lower end. The torsional deflection of the bar is commonly measured using mirrors or optical systems, allowing high-precision determination of the torsion angle (Figure 1.1).

A historical milestone in the application of gravimetry to geophysical exploration was the discovery of the Nash Dome, located along the Texas coast. This event is regarded as the first geophysical identification of an oil and gas accumulation, achieved through surveys conducted with torsion balances (Lafehr, 1980).

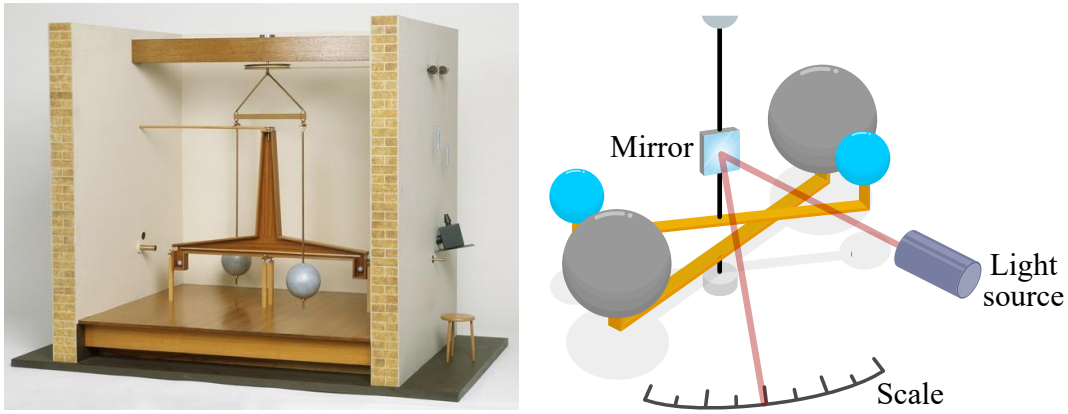

(a) (b)

Figure 1.1: Historical torsion balances used in early gravimetric measurements. (a) Model of Henry Cavendish's torsion balance (From Reich (2010)). (b) Schematic illustration of the torsion balance principle (Adapted from: S. Kelley – National Institute of Standards and Technology. Available at: https://www.nist.gov/image/cavendish-torsion-balance. Accessed August 21, 2025).

During the twentieth century, the development of spring gravimeters revolutionized gravity measurements. These instruments, which employ a mechanical spring to measure variations in local gravity, are significantly more portable and allow continuous field measurements, overcoming many of the limitations associated with pendulum-based devices (Nabighian et al., 2005; Telford et al., 1990). Spring gravimeters were progressively refined, with notable examples such as the Scintrex CG-5 and CG-6, which are widely used in gravity surveys for natural resource exploration. These instruments provide high precision and are capable of detecting gravimetric anomalies associated with geological structures or resource deposits.

In the 1960s, advances in electronic technology and the development of high-quality clocks made it technically feasible to construct gravimeters based on the free-fall time of a test mass (Niebauer, 2007). Naturally, significant technical challenges are involved in releasing (or launching upward) a test object and in accurately determining both the free-fall distance and the corresponding time interval.

Another important innovation in gravity measurement is the superconducting gravimeter. This device replaces conventional mechanical springs with the magnetic levitation of a superconducting sphere, suspended within a magnetic field generated by superconducting coils. Variations in the local gravitational field induce changes in the magnetic forces acting on the sphere, and the position of the test mass is monitored with extremely high precision (Goodkind, 1999).

In summary, the evolution of gravimeters reflects continuous advances in measurement technology and fundamental physics. From the earliest experiments with gravitational pendulums to modern high-precision superconducting gravimeters, each technological development has expanded the capabilities for measuring gravitational acceleration. Currently, one of the most promising innovations in gravimetry is the quantum gravimeter, which benefits from advances in quantum physics, particularly in the field of ultracold atom interferometry.

1.3 Classification of gravimeters

Gravimeters can be broadly classified into two categories: absolute and relative instruments (Nabighian et al., 2005). Absolute gravimeters provide the absolute value of the gravitational acceleration at a specific location. Relative gravimeters, in contrast, measure only gravity variations or differences between measurement stations, requiring calibration and reference to locations with known gravity values in order to obtain absolute gravity estimates (Niebauer, 2007; Telford et al., 1990).

1.3.1 Absolute gravimeters

Absolute gravimeters are instruments designed to directly determine the local value of gravitational acceleration, without the need for prior calibration with respect to a reference station.

Free-fall gravimeter

The most common operating principle of modern absolute gravimeters is based on measuring the free-fall motion of a test mass in a controlled environment, typically under vacuum conditions. The position of the mass is monitored as a function of time using laser interferometry, allowing for an extremely precise determination of gravitational acceleration from the equations of motion.

An example is the A10 absolute gravimeter, shown in Figure 1.2(a). This instrument combines a free-fall system with optical interferometry and highly stable clocks, achieving uncertainties on the order of a few μGal. Absolute gravimeters, however, present important operational limitations, such as high cost, greater instrumental complexity, and reduced portability, which restrict their use primarily to point measurements and fixed stations.

(a)

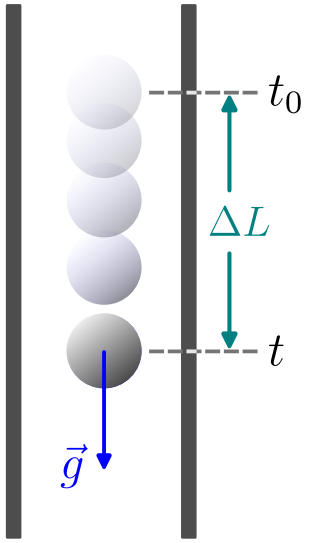

(b)

Figure 1.2: (a) The A10 free-fall absolute gravimeter (Source: reproduced from the official website of the manufacturer), and (b) its operating principle, which consists of measuring the time required for a body to fall a distance ΔL under free-fall conditions.

1.3.2 Relative gravimeters

The operation of a relative gravimeter is based on comparing variations in the gravitational field with respect to a reference measurement station, commonly referred to as a base station. These instruments are widely used in geophysical surveys due to their portability and rapid data acquisition capabilities.

Mass–spring gravimeters

The most common type of relative gravimeter is based on a mechanical mass–spring system, in which a proof mass is supported by a spring. The fundamental physical principle of this instrument is associated with the equilibrium between the gravitational force acting on the mass and the restoring force of the spring, in accordance with Hooke's law.

Prior to field operation, this type of gravimeter must be calibrated at a location where the gravitational acceleration is known, typically determined beforehand using

an absolute gravimeter. When the instrument is subsequently moved to a new measurement point, where the gravitational acceleration differs from the reference value by an amount $\Delta\vec{g}$, a change occurs in the gravitational force acting on the proof mass. This change results in an additional displacement of the spring relative to its initial equilibrium position (Figure 1.3). By measuring this deformation with high precision, it is possible to estimate the relative variation in gravitational acceleration between the two locations.

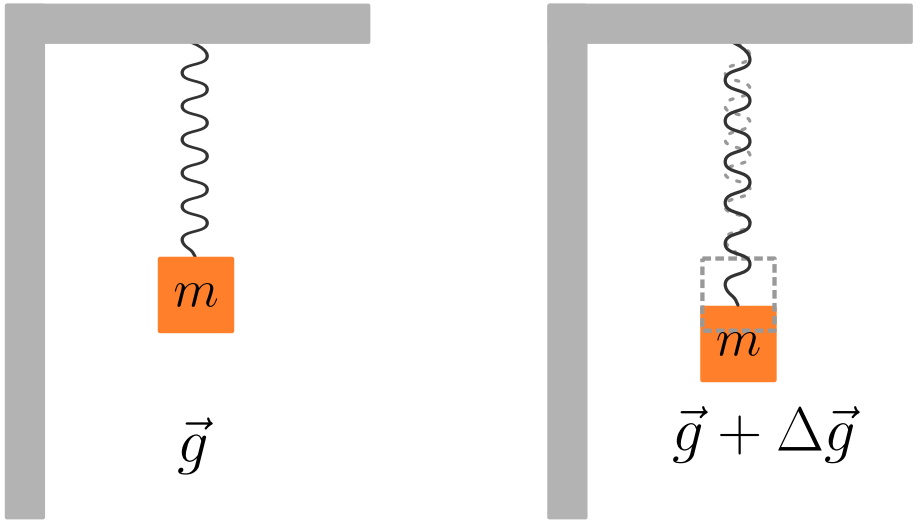

(a) (b)

Figure 1.3: Schematic and simplified representation of the operating principle of a mass–spring–based gravimeter. Illustration (a) shows the mass–spring system at a reference position where the gravitational acceleration $\vec{g}$ is known. In (b), when the instrument is moved to a location where the gravitational acceleration is $\vec{g}+\Delta\vec{g}$, the variation $\Delta\vec{g}$ can be estimated from the additional deformation of the spring relative to its initial position.

A representative example of this type of instrument is the Scintrex CG-6 gravimeter (Figure 1.4). This gravimeter employs a zero-length spring system combined with high-resolution sensors, allowing the detection of gravity variations on the order of $5\,\mu$Gal (Scintrex, 2019).

Figure 1.4: The Scintrex CG-6 gravimeter (Source: reproduced from the official website of the manufacturer).

Superconducting gravimeters

In a superconducting gravimeter, the mechanical spring is replaced by a superconducting sphere that levitates due to the magnetic field generated by a set of coils. This assembly is maintained at temperatures close to absolute zero, ensuring that the materials remain in the superconducting state (Figure 1.5) (Goodkind, 1999). When the local gravity increases or decreases, the gravitational force acting on the sphere changes, inducing a tendency for vertical displacement of the levitated mass. This displacement is detected by a feedback control system that injects an additional electric current into an auxiliary coil in order to restore the sphere to its equilibrium position. The magnitude of this current, or the associated voltage, is directly proportional to the gravity variation (Goodkind, 1999; Pendiuk et al., 2023).

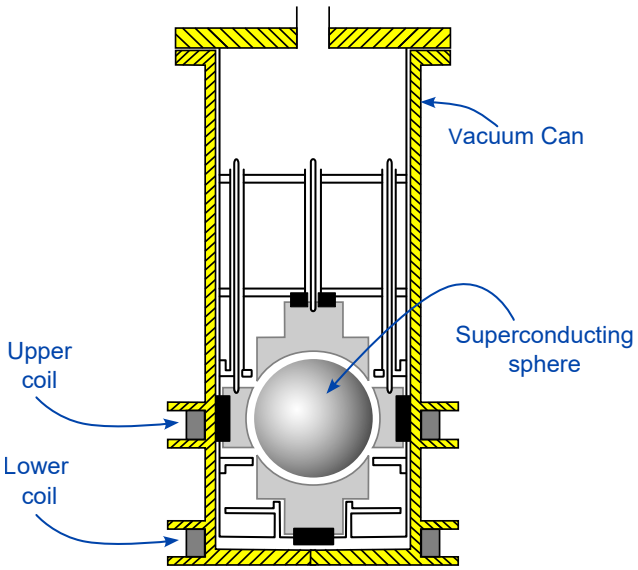

Figure 1.5: Schematic illustration of a superconducting gravimeter, showing the superconducting sphere and the set of coils responsible for the levitation and position control of the proof mass (Source: Adapted from Sun et al. (2001)).

Among the most recent advances in gravimetry, quantum gravimeters represent a paradigm shift, as they rely on atomic properties rather than macroscopic test masses. By exploiting matter-wave interferometry with ultracold atoms, these instruments offer high long-term stability, absolute measurements, and reduced sensitivity to mechanical drift.

In order to synthesize the main characteristics discussed throughout this chapter, Table 1.1 presents a comparative overview of representative gravimeter types, highlighting their operating principles, typical sensitivities, and instrumental drift levels. The selected instruments exemplify the major classes described previously, namely free-fall absolute gravimeters (A10), spring-based relative gravimeters (Scintrex CG-6), superconducting gravimeters (iGrav), and quantum gravimeters based on cold-atom interferometry.

As shown in Table 1.1, the Scintrex CG-6 exhibits drift rates on the order of $20\,\mu$Gal/day, which may be considered relatively high depending on the specific application. This level of drift is an intrinsic characteristic of mass-spring systems; if not properly corrected, such instrumental drift can significantly compromise the reliability of gravity measurements, particularly in studies involving subtle temporal variations. Absolute gravimeters, such as the A10, do not exhibit instrumental drift associated with mechanical components, which makes them particularly suitable for

applications requiring high temporal stability.

Table 1.1: Comparison between different types of gravimeters

Gravimeter	Operating Principle	Sensitivity	Drift
A10	Free-fall	10 μGal (Micro-g LaCoste, 2024)	–
Scintrex CG-6	Spring-mass	$5\mu Gal$ (Scintrex, 2019)	20 $\mu Gal/day$
iGrav	Superconductivity	$0.05\mu Gall$ (manufacturer's website)	1/2 $\mu Gal/month$
Quantum Grav.	Cold Atom Interferometry	$1\mu Gall$ (Exail, 2023)	–

It is important to note that, according to the values presented in Table 1.1, the superconducting gravimeter exhibits superior sensitivity. However, a higher sensitivity alone does not necessarily imply that this instrument is better, since the choice of gravimeter depends on the intended application. For instance, quantum gravimeters offer better portability and operational flexibility, making them applicable to mobile surveys. In contrast, the iGrav superconducting gravimeter is specifically designed for continuous measurements on fixed platforms, typically installed in permanent geophysical observatories. The operating principles and applications of quantum gravimeters are discussed in detail in the chapter 3.

Chapter 2

A reminder of quantum mechanical concepts

This chapter provides a brief review of fundamental quantum mechanical concepts required for the understanding of the operating principles of a quantum gravimeter. It is primarily intended for geoscientists who may not be routinely exposed to quantum mechanics and related formalisms. The purpose of this chapter is therefore to establish the minimum theoretical background necessary to follow the subsequent chapters, where quantum interferometric techniques are applied to gravity measurements.

We observe that the majority of devices for geoscientific applications used in the twentieth century are "classical", i.e., grounded in and exploiting concepts of classical physics. For instance, the seismometers used in modern seismology were developed in the early twentieth century, and seismology uses the formulation of the equations governing the propagation of seismic waves in elastic media (Love, 1911; Gutenberg, 1914), and, similarly, the magnetotelluric method is based on the principles of electromagnetism (Jackson, 1999). From this perspective, up to now a significant part of the academic background needed to work in geoscience remains rooted in classical physics, with few direct applications of quantum mechanical concepts. However, as previously discussed, reliable measurement instruments based on quantum principles that are sufficiently robust and portable for geophysical applications are now more and more becoming available for field and space-based measurements (Freier et al., 2016; Ménoret et al., 2018; Cooke et al., 2021; Weng et al., 2021; Bidel et al., 2023; Chen, 2023; Antoni-Micollier et al., 2024). Commercial instruments, such as (Glässel et al., 2025), are gaining applications not only for gravimeter,s but also for inertial navigation (Exail, 2025). Other devices measure the magnetic field (Rovny et al.,

2022) or the gravity vector in an optical lattice (LeDesma et al., 2025).

The availability and development of quantum gravimeters, and quantum sensors more generally, are part of the broader recent progress of quantum science and technologies, which has impacted a wide range of research fields and technological applications — from quantum computing and quantum simulation to quantum sensing. We are now witnessing a significant expansion of their practical applications. The quantum gravimeter, based on atomic interferometry, represents a remarkable example of this new generation of instruments (Kasevich and Chu, 1991; Ménoret et al., 2018).

These developments serve as a call to attention for the geoscientific community, encouraging explorations at the intersection between quantum physics and the geosciences. Since, regarding physics, the university background in geoscience and geophysics in bachelor and master formation often (but not always exclusively) has classical physics and electromagnetism as a core element, we think it is useful to provide an introduction of the essentials of quantum gravimeters which can be helpful for geophysicist readers more accustomed to the classical paradigm and for which many quantum concepts (and, perhaps even more, the notation used in quantum mechanics) may be rather counterintuitive. For the same reason, we do not discuss the geophysical applications of quantum gravimeters, since they are of course very well known to the geoscience and geophysics communities.

Throughout this chapter, the term quantum gravimeter refers to a quantum sensor designed to measure gravity by exploiting quantum resources, while ultracold denotes quantum gravimeters based on ultracold atoms. Standard textbooks on ultracold atoms may be consulted for further background (Pethick and Smith, 2008; Pitaevskij and Stringari, 2016). Here, only those properties of ultracold atoms that are directly relevant to the description of ultracold quantum gravimeters are discussed, with emphasis placed on the underlying quantum mechanical principles governing their operation.

2.1 The superposition principle

To illustrate a key mechanism of quantum mechanics, Schrödinger proposed a thought experiment that became widely known as the Schrödinger's cat (Schrödinger, 1983; Peres, 1995). The original motivation of Schrödinger was to discuss the situation in which the laws of quantum mechanics are applied to macroscopic systems. However, this discussion is not pursued here; instead, Schrödinger's cat is used as an example of quantum superposition. The experiment consists of placing a cat inside a sealed box together with: (i) a radioactive atom, which may or may not undergo

decay; (ii) a radiation detector, responsible for identifying the decay event; and (iii) a flask containing poison. If the atom decays, the detector activates a mechanism that breaks the flask, releasing the poison, which consequently leads to the death of the cat (Figure 2.1).

According to quantum mechanics, the radioactive atom exists in a superposition of states – "decayed" and "not decayed" – until the moment of observation. Since the fate of the cat is directly correlated with the quantum state of the atom, the cat itself is also in a superposition of the states "alive" and "dead".

Historically the two states are "alive" and "dead", but for kindness to cats presentation reasons, we prefer to think the flask has some substance which can make the cat falling asleep. Accordingly, the states will be referred to as "awake" and "sleeping". Thus, only when the box is opened and an observation is performed does the system collapse, yielding one of the possible classical outcomes: the cat is either awake or sleeping.

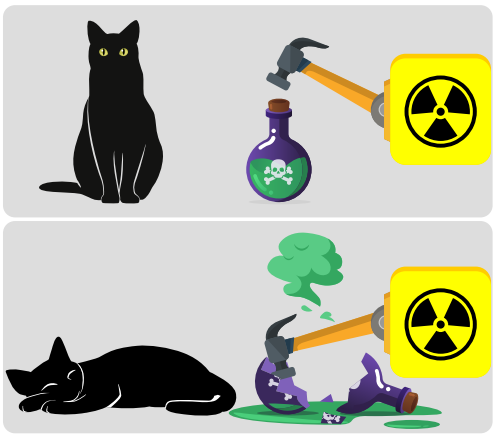

Figure 2.1: Schematic representation of the Schrödinger's cat. In the upper image, the case is illustrated where the radioactive atom has not decayed. In the lower image, the scenario is shown where the atom has decayed, triggering the mechanism that releases the substance, possibly resulting in the death or sleep of the cat.

2.2 The bra-ket notation

In the standard formulation of quantum mechanics (Dirac, 1930; Cohen-Tannoudji et al., 1977; Shankar, 1980), a notation known as the *bra–ket* notation is employed to represent vectors. In this formalism, a generic column vector $(a_1\ a_2\ a_3\ \ldots\ a_n)^T$,

with the a_i being complex numbers ($a_i \in \mathbf{C}$), is represented using the *ket* symbol $|\bullet\rangle$ as follows:

$$|a\rangle = \begin{pmatrix} a_1 \\ a_2 \\ a_3 \\ \vdots \\ a_n \end{pmatrix} . \tag{2.1}$$

Similarly, the vector corresponding to the conjugate transpose of $|a\rangle$ is called a *bra* and is represented by the symbol $\langle\bullet|$. Thus,

$$\langle a| = \begin{pmatrix} a_1^* & a_2^* & a_3^* & \cdots & a_n^* \end{pmatrix} . \tag{2.2}$$

The bra (2.1) can be written as $|a\rangle = \sum_{i=1}^{n} a_i |i\rangle$, with $\{|i\rangle\}$ with $i = 1, \cdots, n$. This means that $|1\rangle = (1\ 0\ 0\ \ldots\ 0)^T$, $|2\rangle = (0\ 1\ 0\ \ldots\ 0)^T$, and so on. The vectors $(1\ 0\ \cdots\ 0)^T$, ... $(0\ \cdots\ 1)^T$ are called basis states – or canonical basis vectors – and they form an orthonormal basis of the state space of the system. So therefore writing $|a\rangle = \sum_{i=1}^{n} a_i |i\rangle$ amounts to write the bra $|a\rangle$ in the basis $\{|i\rangle\}$. In the same way, we have $\langle a| = \sum_{i=1}^{n} a_i^* \langle i|$.

The combination of a bra and a ket defines an inner product, whereas the combination of a ket and a bra defines an outer product. Considering the *ket* $|b\rangle$ (with the same dimension as $|a\rangle$), the inner product between these two vectors is given by (Cohen-Tannoudji et al., 1977; Shankar, 1980)

$$\langle a|b\rangle = \begin{pmatrix} a_1^* & a_2^* & a_3^* & \cdots & a_n^* \end{pmatrix} \begin{pmatrix} b_1 \\ b_2 \\ b_3 \\ \vdots \\ b_n \end{pmatrix} = a_1^* b_1 + a_2^* b_2 + a_3^* b_3 + \cdot + a_n^* b_n \tag{2.3}$$

and the corresponding outer product takes the form

$$|a\rangle\langle b| = \begin{pmatrix} a_1 b_1^* & a_1 b_2^* & \cdots & a_1 b_n^* \\ a_2 b_1^* & a_2 b_2^* & \cdots & a_2 b_n^* \\ \vdots & \vdots & \ddots & \vdots \\ a_n b_1^* & a_n b_2^* & \cdots & a_n b_n^* \end{pmatrix} .$$

In the bra-ket notation, one can also compute expectation values of observables: if one has an observable $\mathcal{O}$, corresponding to an Hermitian operator $\hat{\mathcal{O}}$, one can write it – in the basis in which the bra (2.1) and ket (2.2) are written – as a matrix $O_{i,j} = \langle i|\hat{\mathcal{O}}|j\rangle$. The expectation value of the observable $\mathcal{O}$ on a state $|a\rangle$ and is given by $\langle a|\hat{\mathcal{O}}|a\rangle = \sum_{i,j=1}^{n} a_i^* O_{i,j} a_j$.

2.3 The description of quantum states

Let us assume that in Schrödinger's cat experiment the probability that the cat is awake when the box is opened is found to be $\frac{9}{10}$ (90%), and thus the probability that the cat is sleeping is found to be $\frac{1}{10}$ (10%). But how can we represent this "awake–sleeping" state mathematically? Considering that the quantum state is represented by $|\psi\rangle$, the simplest way to represent the state in which the cat finds itself is by using a column vector that stores the probability of "observing" each state, that is:

$\frac{1}{10} \rightarrow$ Probability that the cat is dead/sleeping

$\frac{9}{10} \rightarrow$ Probability that the cat is alive/awake

We can rewrite $|\psi\rangle$ as follows:

$$|\psi\rangle = \alpha \begin{pmatrix} 0 \\ 1 \end{pmatrix} + \beta \begin{pmatrix} 1 \\ 0 \end{pmatrix}, \tag{2.4}$$

where α and β are complex numbers. We can choose one of the two, say α, to be real.

The vectors $(1\ 0)^T$ and $(0\ 1)^T$ are the basis states and they represent the two possible situations for the cat:

$$\left| \text{  } \right\rangle \equiv \begin{pmatrix} 0 \\ 1 \end{pmatrix} \quad \rightarrow \text{ Cat awake} \tag{2.5}$$

$$\left| \text{  } \right\rangle \equiv \begin{pmatrix} 1 \\ 0 \end{pmatrix} \quad \rightarrow \text{ Cat sleeping} \tag{2.6}$$

Therefore, Eq. (2.4) can be written as

$$|\psi\rangle = \alpha \left| \text{  } \right\rangle + \beta \left| \text{  } \right\rangle \tag{2.7}$$

The quantum state $|\psi\rangle$ contains all the information about all the system. Consequently, from it we must be able to compute the probability associated with each outcome of the measurement whether the cat is live or sleeping. In the Schrödinger's cat example, the probabilities are real numbers (such as the values 9/10 and 1/10

in Eq. (2.7)). We have then to ensure that the total probability associated with all possible outcomes of the measurement is equal to 1.

Since $|\psi\rangle$ describes the superposition of all possible states (in this case, live or sleeping), the sum of the probabilities of all these states must necessarily be equal to 1. Mathematically, this condition is ensured by normalizing the state $|\psi\rangle$, imposing

$$\langle \psi_{\text{norm}} \mid \psi_{\text{norm}} \rangle = 1,$$

thereby guaranteeing that the sum of the squared moduli of the coefficients — possibly complex — is exactly equal to 1.

In other words, the coefficients appearing in the state representation are complex amplitudes, not the probabilities themselves. The probabilities are obtained from the square of the absolute value of these amplitudes:

$$P_{\text{awake}} = |\alpha|^2,$$
$$P_{\text{sleeping}} = |\beta|^2.$$

In the particular case we are looking at, the coefficient α associated with the "awake" state is

$$\alpha = \sqrt{\frac{9}{10}} = \frac{3}{\sqrt{10}}$$

while for the "sleeping" state one obtains

$$\beta = \sqrt{\frac{1}{10}}\, e^{i\theta} = \frac{1}{\sqrt{10}}\, e^{i\theta},$$

where θ is an arbitrary real number. Thus, the correct representation of the normalized quantum state is

$$|\psi_{\text{norm}}\rangle = \frac{3}{\sqrt{10}} \left| \text{  } \right\rangle + \frac{1}{\sqrt{10}} e^{i\theta} \left| \text{  } \right\rangle, \tag{2.8}$$

which is equivalent to:

$$|\psi_{\text{norm}}\rangle = \begin{pmatrix} \frac{1}{\sqrt{10}} \\ \\ \frac{3}{\sqrt{10}} e^{i\theta} \end{pmatrix}.$$

Note that now, when we compute

$$\langle \psi_{\text{norm}} | \psi_{\text{norm}} \rangle = \left(\frac{3}{\sqrt{10}} \right)^2 + \left(\frac{1}{\sqrt{10}} \right)^2 = 1.$$

From now on, we will omit the subscript $_{\text{norm}}$. Using this notation, in order to compute the probability of the state $|i\rangle$ (where the index i may refer to the live or sleeping states), it is then sufficient to evaluate

$$P_i = |\langle i \mid \psi \rangle|^2, \tag{2.9}$$

that is, for the state (2.8):

$$\left\langle \text{🐈} \middle| \psi \right\rangle = \begin{pmatrix} 0 & 1 \end{pmatrix} \begin{pmatrix} \frac{1}{\sqrt{10}} \\ \\ \frac{3}{\sqrt{10}} \end{pmatrix} = \frac{3}{\sqrt{10}} \qquad P_{awake} = \left| \left\langle \text{🐈} \middle| \psi \right\rangle \right|^2 = \frac{9}{10}$$

$$\left\langle \text{🐈‍⬛} \middle| \psi \right\rangle = \begin{pmatrix} 1 & 0 \end{pmatrix} \begin{pmatrix} \frac{1}{\sqrt{10}} \\ \\ \frac{3}{\sqrt{10}} \end{pmatrix} = \frac{1}{\sqrt{10}} \qquad P_{sleeping} = \left| \left\langle \text{🐈‍⬛} \middle| \psi \right\rangle \right|^2 = \frac{1}{10}$$

Crucially, the vector $|\psi\rangle$ can be expressed as a linear combination (or superposition) of different basis states $|i\rangle$, which correspond to the possible outcomes of a measurement. This can be then written as

$$|\psi\rangle = \sum_i C_i |i\rangle, \tag{2.10}$$

where C_i are complex numbers called probability amplitudes. The square of the absolute value of these amplitudes, $|C_i|^2$, gives the probability of obtaining the state $|i\rangle$ when performing a measurement of an observable having as eigenvalues exactly the states $\{|i\rangle\}$.

2.4 The energy levels

Particles such as electrons in an atom, when they have a negative energy and are in a bound state, cannot occupy just any energy level, but are restricted to discrete, or quantized, values. These particles occupy only certain allowed states, each with a well-defined energy value (Cohen-Tannoudji et al., 1977; Shankar, 1980; Griffiths, 2018; Sakurai and Napolitano, 2020).

An extremely useful model in atomic physics is the so-called *two-level system*. Although atoms have of course many possible energy levels (Foot, 2007), in many situations we can simplify their description using only two energy levels (Orszag, 2024): in other words, when only (or mostly) contributions from two energy levels enter the physical quantities, we can restrict the basis to the two energy levels

- a state $|a\rangle$ with energy E_a;
- a state $|b\rangle$ with energy E_b.

$|a\rangle$ and $|b\rangle$ are eigenstates of the Hamiltonian H:

$$H|a\rangle = E_a|a\rangle, \tag{2.11}$$
$$H|b\rangle = E_b|b\rangle. \tag{2.12}$$

We refer to $|a\rangle$ as the *ground state* and to $|b\rangle$ as the *excited state*. As an example, for a particle in a double well potential, having two energy minima well separated by an energy barrier, the state $|a\rangle$ and $|a\rangle$ can be really the two lowest energy states, and the $|a\rangle$ the state with minimum energy.

The energy difference between the two energies E_b and E_a defines the frequency of transition

$$\omega = \frac{E_b - E_a}{\hbar}$$

in the sense that a photon can be absorbed, if its angular frequency ω, is such that the atom may change its state from $|a\rangle$ to $|b\rangle$. Inversely, when the atom state decays spontaneously from $|b\rangle$ to $|a\rangle$, it emits a photon of the same energy.

An important point to be noticed is that all the parameters of the Hamiltonian of the system, such as the mass, are encoded in the energies E_a, E_b. If one wants to study the motion of the atoms, one has to include the kinetic energy term explicitly (see Section 3.2).

The average energy of the atom can be calculated as the average of the energies of the levels that constitute the system (E_a and E_b) weighted by the probabilities of each of these states (P_a and P_b), that is

$$\langle E \rangle = E_b\, P_b \,+\, E_a\, P_a.$$

By using Eq. (2.9), we can rewrite the average energy as

$$\begin{aligned}\langle E \rangle &= E_b\, |\langle b|\psi\rangle|^2 + E_a\, |\langle a|\psi\rangle|^2 \\ &= \langle\psi|(E_b|b\rangle\langle b| + E_a|a\rangle\langle a|)\,|\psi\rangle\end{aligned}$$

Based on the previous expression, we can define the Hamiltonian operator in the basis $\langle a|, \langle b|$ as:

$$H = E_b|b\rangle\langle b| + E_a|a\rangle\langle a|$$

which in turn can be rewritten in matrix form, see e.g. (Kok, 2018), as

$$H = \begin{pmatrix} E_b & 0 \\ 0 & E_a \end{pmatrix}.$$

2.5 The Schrödinger equation

The Hamiltonian not only encodes the energy of the system, but it is also related to the time evolution of the system. Thus, once the Hamiltonian of a quantum system is known, it becomes possible to determine how its state evolves over time (Cohen-Tannoudji et al., 1977; Shankar, 1980; Griffiths, 2018; Kok, 2018; Sakurai and Napolitano, 2020). Consider again the state of a two-level atom at time ($t = 0$). We write the initial state as a coherent superposition of the energy eigenstates as

$$|\psi(0)\rangle = C_a|a\rangle + C_b|b\rangle,$$

where C_a and C_b are complex amplitudes satisfying $|C_a|^2 + |C_b|^2 = 1$.

Since $|a\rangle$ and $|b\rangle$ are eigenstates of the Hamiltonian according to (2.12), the time evolution of the probability amplitudes C_a, C_b is simply a phase factor. The state at time t becomes

$$|\psi(t)\rangle = C_a e^{-iE_a t/\hbar}|a\rangle + C_b e^{-iE_b t/\hbar}|b\rangle.$$

This expression shows that each component of the state acquires a phase proportional to its energy. Importantly, the relative phase between the levels evolves as

$$\Delta\phi(t) = \frac{E_b - E_a}{\hbar}\, t = \omega t,$$

where ω is the transition frequency of the two-level system. Computing the time derivative of the state and using the eigenvalue equations of the Hamiltonian (2.12), we obtain the celebrated time-dependent Schrödinger equation:

$$i\hbar\frac{d}{dt}|\psi(t)\rangle = H|\psi(t)\rangle. \tag{2.13}$$

This is the central equation governing the quantum evolution of non-relativistic quantum systems. It tells us that once the Hamiltonian is known, the time dynamics of the system is completely determined. For the two-level atom with Hamiltonian (2.4), the Schrödinger equation describes how population and phase evolve between the ground and excited states. In the next sections, we will incorporate interactions such as laser fields, which modify the Hamiltonian and allow transitions between the levels, leading to the quantum dynamics fundamental to atomic interferometry and quantum sensing.

Chapter 3

Atom Interferometry

This chapter presents the theoretical foundations of the absolute quantum gravimeter. It derives the evolution of the atomic quantum state under gravitational acceleration and introduces the measurement principle in a form accessible to geophysicists. Inherent to the quantum mechanical treatment is the dual property of the atom, having both a mass and a wave nature of the probability amplitude of its position. The mathematical treatment includes the interaction of the atoms with the laser pulses, essential to the gravity measurement. The aim of this effort is to fill the gap between a physicist's description of the quantum gravimeter principle, as discussed e.g. in (Peters et al., 2001; Chu, 2001; Kasevich and Chu, 1991; Young et al., 1997; Freier et al., 2016; Junior et al., 2026), and the papers describing the applications of the gravimeter as e.g. (Ménoret et al., 2018; Wu et al., 2019). The former assumes the reader has the background basic quantum physics knowledge obvious for a physicist, the latter have the focus on the observational results. The benefit of the quantum gravimeter is the measurement of the absolute gravity field value, and in principle the absence of drift in the measured values, as explained and discussed in the selection of publications explained next.

Ménoret et al. (2018) demonstrated the stability and sensitivity of a transportable absolute quantum gravimeter at the level of $10\,\mathrm{nm\,s^{-2}}$ over a 1 month long measurement. Wu et al. (2019) illustrated observations of the tidal and ocean loading gravity signal, with a sensitivity of $20\,\mathrm{nm\,s^{-2}}$. They showed that the effect of the tidal signal is seen in the Allan deviation leading to peaks at long times (starting from several hours and beyond 24 hours) and in the the noise spectrum. The performance of the commercial gravimeter AQG#B01 of the company Muquans showed absence of instrumental drift over a period of 2 weeks, defined in the limits of the uncertainty range, and repeatability better than $50\,\mathrm{nm\,s^{-2}}$. The performance was tested com-

paring it to a classical optical interferometric absolute gravimeter (Micro-g-LaCoste, FG5#228), and a superconducting relative gravimeter (GWR, igrav#002) in the Larzac observatory in southern France and in a laboratory in Montpellier (Cooke et al., 2021). They studied geophysical signals comprised earth tides and hydrological signals, and atmospheric gravity and loading effects. The absence of drift is particularly important for acceleration measurements from space, as the useful spectral measurement bandwidth has no lower frequency limit, as is the case for the electrostatic accelerometer (Zingerle et al., 2024; Romeshkani et al., 2025; Rossi et al., 2023). The consequence is the increase of the observable spatial wavelength along the satellite orbit, beneficial for the determination of the low degrees in the spherical harmonic expansion of the gravity potential field (Migliaccio et al., 2019; Migliaccio et al., 2023; Rossi et al., 2023). The lowered noise spectrum leads further to improved spatial and temporal resolution of the retrieved field with improved resolution of hydrologic, oceanic and solid earth signals (Kusche et al., 2025; Braitenberg and Pastorutti, 2024; Pivetta et al., 2022). A comprehensive review of classical and atomic gravimetry, including airborne, marine, and space-based approaches, can be found in (Fang et al., 2024).

3.1 Two-Level

Quantum gravimeters use the principle of interferometry to perform precise measurements of gravitational acceleration. More specifically, they function as Mach-Zehnder interferometers that utilize the phenomenon of interference to measure the phase differences between two distinct paths traversed by a wave (Freier et al., 2016; Schilling et al., 2020; Müller and Wu, 2020). In these devices, a light source emits a beam that initially strikes a beam splitter, causing the wave to propagate through two different arms (paths). Each beam is then reflected by mirrors until they are recombined and, subsequently, split again by another beam splitter. Finally, two light intensity detectors measure the interference pattern generated by the recombination of the light beams, which is a function of the phase difference $\Delta\phi$ between the two light beams that traverse distinct paths (Figure 3.1.a).

A quantum Mach-Zehnder interferometer may probe also the interference of matter waves. In this case, there are no physical beam splitters or mirrors as for electromagnetic waves. Laser pulses act on atoms in a manner equivalent to a beam splitter or a mirror, depending on how the laser-atom interaction takes place. What determines whether the laser acts as a beam splitter or as a mirror is the relation between the frequencies involved and the duration of the pulse. This aspect will be discussed in more detail throughout this section. For the purposes of this work, a

$\pi/2$ pulse will be defined as the pulse that acts as a beam splitter, while a π pulse will be defined as the pulse that acts in a manner equivalent to a mirror.

In a quantum Mach-Zehnder interferometer, the atoms can be initially prepared in the same internal state $|a\rangle$ (the ground state) and, after a $\pi/2$ pulse, are "split" into two paths, which are described by atoms in the different internal states $|a\rangle$ and $|b\rangle$. Atoms in the state $|a\rangle$ follow a trajectory that is different from that followed by atoms in the state $|b\rangle$ (excited state). The atoms then propagate along two distinct paths of the interferometer and, after a time interval T, interact with a π pulse, which induces an inversion of the quantum states. Subsequently, after a further time interval T, the paths are recombined, and a third interaction with a $\pi/2$ laser pulse takes place, resulting in a cloud of atoms in a superposition of the states $|a\rangle$ and $|b\rangle$ (Figure 3.1.b).

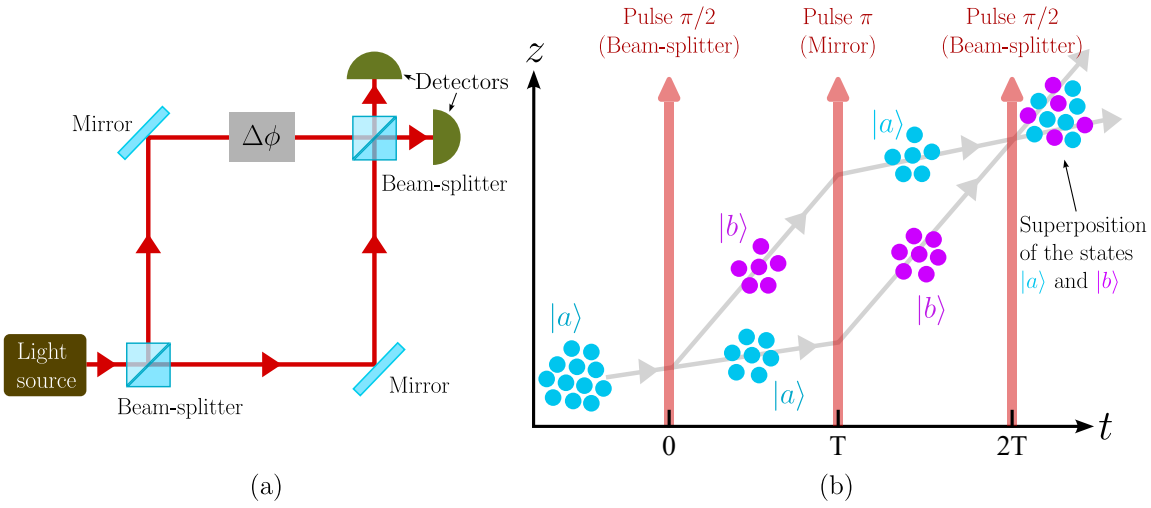

Figure 3.1: (a) Schematic representation of a Mach–Zehnder interferometer based on optical beams. (b) Illustration of a quantum Mach–Zehnder interferometer, in which matter waves are used.

To make contact with the the concepts presented in the previous section, a quantum gravimeter can be conceptually simplified as a two-level system, with two states: the ground state ($|a\rangle$) and the excited state ($|b\rangle$). It is important to note that this system exhibits two levels in a manner analogous to Schrödinger's cat thought experiment. By analogy, and strictly for didactic purposes, one may associate the level $|a\rangle$ with the atom being in the "awake" state, whereas $|b\rangle$ corresponds to what is the "sleeping" state.

In this context, the following question arises: what is the analogue of the "radiation detector" in the quantum gravimeter? In other words, what is the mechanism responsible for inducing transitions between the atomic levels in the quantum gravimeter? The answer is: a laser pulse. In the quantum gravimeter the particle is initially in the ground state, characterized by the energy E_a. After interacting with a laser pulse, the particle may absorb a photon and, consequently, undergo a transition to the excited state, with energy E_b.

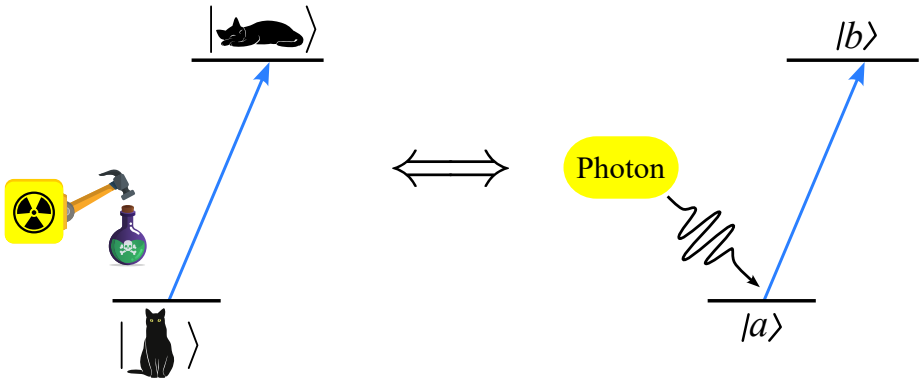

Figure 3.2: A pictorial comparison between the operating principles of a quantum gravimeter and the Schrödinger's cat thought experiment. The figure illustrates that the "alive" (or "awake") and "dead" (or "sleeping") states of the cat are conceptually analogous to the atomic energy levels. In this analogy, the laser photons play a role equivalent to that of the radiation detector in the cat experiment. Specifically, the absorption of a photon by the atom determines whether a transition between energy levels will occur, in the same way that poison/sleeping substance is released (or not) in the Schrödinger's cat thought experiment.

For the state transition to occur, the laser frequency ω must be resonant with the energy difference between the two levels, so that the photon provides the necessary energy to induce the transition (Orszag, 2024). Thus, the resonance condition requires that $\omega \approx \omega_{ba}$, where $\omega_{ba} = \omega_b - \omega_a$ is the frequency associated with the transition (Orszag, 2024; Young et al., 1997). The difference between the laser frequency and the transition frequency defines the *detuning*, given by

$$\delta = \omega - \omega_{ba} = \omega - (\omega_b - \omega_a)$$

(see figure 3.3).

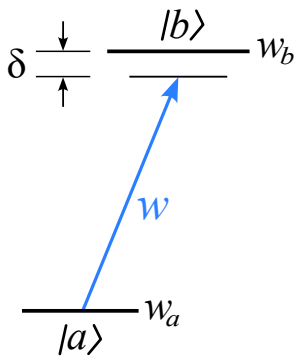

Figure 3.3: Schematic representation of the two levels with their associated frequencies.

The electric field of the laser can be written as:

$$\mathbf{E} = \mathbf{E}_0 \cos(\omega t + \phi) . \tag{3.1}$$

Since the dimension of atoms is on the order of angstroms ($\approx 10^{-10}$ m), while the wavelength of $\mathbf{E}$ is typically much larger, the amplitude of the field is essentially constant over the spatial extension of the atom. Consequently, the atom may be treated as a dipole of moment $\mathbf{d}$ under the influence of the electromagnetic field, and therefore the Hamiltonian describing the system can be written in matrix form as:

$$\hat{H}_{\text{int}} = -\mathbf{d}\cdot\mathbf{E} = \begin{pmatrix} 0 & \langle b|-\mathbf{d}\cdot\mathbf{E}|a\rangle \\ \langle a|-\mathbf{d}\cdot\mathbf{E}|b\rangle & 0 \end{pmatrix}, \tag{3.2}$$

Therefore the Hamiltonian of an atom interacting with an electromagnetic field can be written as the sum of two contributions:

$$\hat{H} = \hat{H}_0 + \hat{H}_{\text{int}},$$

where $\hat{H}_0$ corresponds to the time-independent Hamiltonian of the free atom given by

$$\hat{H}_0 = \hbar w_a |a\rangle\langle a| + \hbar w_b |b\rangle\langle b| = \begin{pmatrix} \hbar w_b & 0 \\ 0 & \hbar w_a \end{pmatrix}, \tag{3.3}$$

with $(0\ 1)^T = |a\rangle$ and $(1\ 0)^T = |b\rangle$ (of course, this choice is arbitrary and we could have choosen the opposite). The Hamiltonian $\hat{H}$ can be written as follows:

$$\hat{H} = \hbar w_a |a\rangle\langle a| + \hbar w_b |b\rangle\langle b| - \mathbf{d}\cdot\mathbf{E} \tag{3.4}$$

The time evolution of a general quantum state is described by

$$|\psi(t)\rangle = C_a(t)\, e^{-iw_a t}|a\rangle + C_b(t)\, e^{-iw_b t}|b\rangle, \tag{3.5}$$

with $C_a(t)$ and $C_b(t)$ complex amplitudes. This evolution is governed by the time-dependent Schrödinger equation:

$$i\hbar\frac{d}{dt}|\psi(t)\rangle = \left(\hat{H}_0 + \hat{H}_{\text{int}}\right)|\psi(t)\rangle \tag{3.6}$$

By differentiating (3.5) with respect to time, we obtain

$$\begin{aligned} i\hbar\frac{\partial}{\partial t}|\psi(t)\rangle =& \, i\hbar\dot{C}_a\, e^{-iw_a t}|a\rangle + \hbar w_a C_a(t)\, e^{-iw_a t}|a\rangle + \\ &+ i\hbar\dot{C}_b\, e^{-iw_b t}|b\rangle + \hbar w_b C_b(t)\, e^{-iw_b t}|b\rangle \end{aligned}$$

with

$$\hat{H}_{\text{int}}|\psi(t)\rangle = i\hbar\dot{C}_a\, e^{-iw_a t}|a\rangle + i\hbar\dot{C}_b\, e^{-iw_b t}|b\rangle.$$

To proceed, we project this expression onto the basis states $|a\rangle$ and $|b\rangle$. This yields

$$\begin{aligned} \langle a|\hat{H}_{\text{int}}|\psi(t)\rangle =& i\hbar\dot{C}_a\, e^{-iw_a t}, \\ \langle b|\hat{H}_{\text{int}}|\psi(t)\rangle =& i\hbar\dot{C}_b\, e^{-iw_b t}. \end{aligned}$$

Thus,

$$\langle a|\hat{H}_{\text{int}}|\psi(t)\rangle = \langle a|-\mathbf{d}\cdot\mathbf{E}|b\rangle C_b(t)e^{-iw_b t}, \tag{3.7}$$

$$\langle b|\hat{H}_{\text{int}}|\psi(t)\rangle = \langle b|-\mathbf{d}\cdot\mathbf{E}|a\rangle C_a(t)e^{-iw_a t}. \tag{3.8}$$

The electric field $\mathbf{E}$, given in Eq. (3.1) and appearing in the expressions, above can be decomposed as:

$$\mathbf{E} = \mathbf{E}_0\cos(\omega t + \phi) = \mathbf{E}_0\left(\frac{e^{i\omega t}e^{i\phi} + e^{-i\omega t}e^{-i\phi}}{2}\right). \tag{3.9}$$

This decomposition allows the application of the so-called Rotating Wave Approximation (RWA) in order to neglect the rapidly oscillating term (Orszag, 2024) and to retain only the slowly varying components of the field. This means that only one of the complex exponentials, either $e^{i\omega t}$ or $e^{-i\omega t}$, contributes significantly to the interaction, while the other may be discarded because it oscillates much faster than

the system dynamics. In the case of the transition $|g\rangle \to |e\rangle$, the rapidly oscillating component $e^{i\omega t}$ can be eliminated, and only $e^{-i\omega t}$ is retained, as it is responsible for photon absorption. Conversely, for the transition $|e\rangle \to |g\rangle$, the term to be kept is $e^{i\omega t}$, corresponding to the stimulated emission process.

With this simplification, Eqs. (3.7) and (3.8) take the form

$$\begin{aligned}
\langle a|-\mathbf{d}\cdot\mathbf{E}|b\rangle C_b(t)e^{-iw_b t} &= \frac{\langle a|-\mathbf{d}\cdot\mathbf{E}_0|b\rangle}{2}\, C_b(t)e^{-iw_b t}e^{i\omega t}e^{i\phi},\\
\langle b|-\mathbf{d}\cdot\mathbf{E}|a\rangle C_a(t)e^{-iw_a t} &= \frac{\langle b|-\mathbf{d}\cdot\mathbf{E}_0|a\rangle}{2}\, C_a(t)e^{-iw_a t}e^{-i\omega t}e^{-i\phi}.
\end{aligned}$$

Rewriting these equations, we obtain

$$\begin{aligned}
i\dot{C}_a &= \frac{\langle a|-\mathbf{d}\cdot\mathbf{E}_0|b\rangle}{2\hbar}\, C_b(t)e^{i[\omega-(w_b-w_a)]t}e^{i\phi}\\
i\dot{C}_b &= \frac{\langle b|-\mathbf{d}\cdot\mathbf{E}_0|a\rangle}{2\hbar}\, C_a(t)e^{-i[\omega-(w_b-w_a)]t}e^{-i\phi}.
\end{aligned}$$

Introducing the Rabi frequency (Scully and Zubairy, 1997)

$$\Omega_{ba} = \frac{\langle b|-\mathbf{d}\cdot\mathbf{E}_0|a\rangle}{\hbar},$$

one has

$$\Omega^*_{ba} = \Omega_{ab} = \frac{\langle a|-\mathbf{d}\cdot\mathbf{E}_0|b\rangle}{\hbar}. \tag{3.10}$$

Then, the system of coupled equations acquires the form:

$$\begin{aligned}
i\,\dot{C}_a &= \frac{\Omega^*_{ba}}{2}\, e^{+i(\delta\, t+\phi)}\, C_b,\\
i\,\dot{C}_b &= \frac{\Omega_{ba}}{2}\, e^{-i(\delta\, t+\phi)}\, C_a.
\end{aligned}$$

This allows us to define $\hat{H}_{\text{int}}$ as

$$\hat{H}_{\text{int}} = \frac{\hbar}{2}\begin{pmatrix} 0 & \Omega_{ba}\, e^{-i(\delta\, t+\phi)} \\ \Omega^*_{ba}\, e^{+i(\delta\, t+\phi)} & 0 \end{pmatrix} \tag{3.11}$$

The Hamiltonian can be made time-independent by adopting a rotating reference frame, expressing the physical idea that during a short pulse can be considered approximately constant. This is achieved by transforming the state ($|\psi\rangle$) into the

state in the rotating frame, ($|\psi\rangle_R$), defined by a rotation around the ($\hat{\boldsymbol{z}}$) axis with angle ($-\delta t$):

$$|\psi\rangle_R = \boldsymbol{D}\left(\hat{\boldsymbol{z}},\, -\delta t\right)|\psi\rangle$$

where $\boldsymbol{D}$ is defined as (Young et al., 1997):

$$\boldsymbol{D} = \begin{pmatrix} e^{+i\delta\, t/2} & 0 \\ 0 & e^{-i\delta\, t/2} \end{pmatrix}. \tag{3.12}$$

Applying the Schrödinger equation to the state expressed in the rotating frame yields:

$$i\hbar\frac{d}{dt}\left(\boldsymbol{D}^\dagger|\psi\rangle_R\right) = \hat{H}_{\text{int}}\left(\boldsymbol{D}^\dagger|\psi\rangle_R\right) \tag{3.13}$$

Rearranging the terms gives the time evolution equation for the state in the rotating frame:

$$i\hbar\frac{d|\psi\rangle_R}{dt} = \left(\boldsymbol{D}\hat{H}_{\text{int}}\boldsymbol{D}^\dagger - i\hbar\boldsymbol{D}\frac{d\boldsymbol{D}^\dagger}{dt}\right)|\psi\rangle_R. \tag{3.14}$$

Therefore, the Hamiltonian in the rotating reference frame is time-independent and it is given by:

$$\hat{H}_R = \boldsymbol{D}\hat{H}_{\text{int}}\boldsymbol{D}^\dagger - i\hbar\boldsymbol{D}\frac{d\boldsymbol{D}^\dagger}{dt} = \frac{\hbar}{2}\begin{pmatrix} -\delta & \Omega_{ba}\, e^{-i\phi} \\ \Omega_{ba}^*\, e^{+i\phi} & +\delta \end{pmatrix}. \tag{3.15}$$

The eigenvalues are

$$\lambda_\pm = \pm\frac{\hbar\Omega_R}{2}, \tag{3.16}$$

where Ω_R is the so-called (off-resonant) Rabi frequency given by

$$\Omega_R = \sqrt{\Omega_{ba}^2 + \delta^2}$$

(from now on, in the main text and in Figure 3.4, unless otherwise specified, we denote the modulus of Ω_{ba} simply by Ω_{ba}). Accordingly, we can express δ, Ω_{ba}, and Ω_R in terms of an angle θ, defined as follows (see Figure 3.4):

$$\sin\theta = \frac{\Omega_{ba}}{\Omega_R} \qquad\qquad \cos\theta = -\frac{\delta}{\Omega_R} \tag{3.17}$$

Note that, when $\delta \ll \Omega_{ba}$ we have $\Omega_{ba} \approx \Omega_R$. Therefore, under the resonant condition ($\delta = 0$), the angle θ becomes $\theta = \pi/2$, so that $\sin\theta = 1$ and $\cos\theta = 0$.

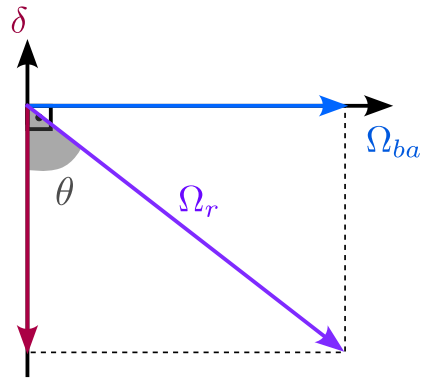

Figure 3.4: Geometric interpretation of the relationship between θ and the parameters δ, Ω_{ba} and Ω_R.

The Hamiltonian $\hat{H}_R$ is diagonalized in terms of the eigenvectors $|\lambda_+\rangle_R$ and $|\lambda_-\rangle_R$, which are associated with the eigenvalues λ_+ and λ_-, respectively (Appendix A). The eigenstates expressed in the rotating-frame basis $\{|a\rangle_R, |b\rangle_R\}$, where again $(0\ 1)^T = |a\rangle_R$ and $(1\ 0)^T = |b\rangle_R$, are given by

$$\begin{aligned} |\lambda_+\rangle &= \sin\left(\frac{\theta}{2}\right) e^{+i\frac{\phi}{2}} |a\rangle_R + \cos\left(\frac{\theta}{2}\right) e^{-i\frac{\phi}{2}} |b\rangle_R \\ |\lambda_-\rangle &= \cos\left(\frac{\theta}{2}\right) e^{+i\frac{\phi}{2}} |a\rangle_R - \sin\left(\frac{\theta}{2}\right) e^{-i\frac{\phi}{2}} |b\rangle_R \end{aligned} \tag{3.18}$$

The projectors $|\lambda_+\rangle\langle\lambda_+|$ and $|\lambda_-\rangle\langle\lambda_-|$ take the matrix forms given in Eqs. (3.19)–(3.20). Using Eqs. (3.12), (3.16)] and (3.21) gives:

$$|\lambda_+\rangle\langle\lambda_+| = \begin{pmatrix} \cos^2\left(\frac{\theta}{2}\right) & \frac{\sin\theta}{2} e^{-i\phi} \\ \frac{\sin\theta}{2} e^{+i\phi} & \sin^2\left(\frac{\theta}{2}\right) \end{pmatrix} \tag{3.19}$$

$$|\lambda_-\rangle\langle\lambda_-| = \begin{pmatrix} \sin^2\left(\frac{\theta}{2}\right) & -\frac{\sin\theta}{2} e^{-i\phi} \\ -\frac{\sin\theta}{2} e^{+i\phi} & \cos^2\left(\frac{\theta}{2}\right) \end{pmatrix} \tag{3.20}$$

The time evolution of the atomic state, in the rotating frame and during the interaction with a light pulse starting at time $t = t_0$, is given by

$$|\psi\left(t_0 + \tau\right)\rangle_R = \left(e^{-\frac{i\lambda_+\tau}{\hbar}} |\lambda_+\rangle\langle\lambda_+| + e^{-\frac{i\lambda_-\tau}{\hbar}} |\lambda_-\rangle\langle\lambda_-|\right) \boldsymbol{D}\left(\hat{\boldsymbol{z}}, -\delta t\right) |\psi\left(t_0\right)\rangle. \tag{3.21}$$

It follows

$$|\psi\left(t_0+\tau\right)\rangle = \begin{pmatrix} e^{-i\delta\tau/2}\left[\cos\left(\frac{\Omega_R\tau}{2}\right) - i\cos\theta\,\sin\left(\frac{\Omega_R\tau}{2}\right)\right] & -ie^{-i\delta\tau/2}e^{-i(\delta t_0+\phi)}\sin\theta\sin\left(\frac{\Omega_R\tau}{2}\right) \\ -ie^{i\delta\tau/2}e^{i(\delta t_0+\phi)}\sin\theta\sin\left(\frac{\Omega_R\tau}{2}\right) & e^{i\delta\tau/2}\left[\cos\left(\frac{\Omega_R\tau}{2}\right) + i\cos\theta\,\sin\left(\frac{\Omega_R\tau}{2}\right)\right] \end{pmatrix} \times \begin{pmatrix} C_b(t_0) \\ C_a(t_0). \end{pmatrix} \tag{3.22}$$

This gives the final result:

$$C_b(t_0+\tau) = e^{-i\delta\tau/2}\Bigg\{C_b(t_0)\left[\cos\left(\frac{\Omega_R\tau}{2}\right) - i\cos\theta\,\sin\left(\frac{\Omega_R\tau}{2}\right)\right] + \\ + C_a(t_0)e^{-i(\delta t_0+\phi)}\sin\theta\sin\left(\frac{\Omega_R\tau}{2}\right)\Bigg\}, \tag{3.23}$$

$$C_a(t_0+\tau) = e^{+i\delta\tau/2}\Bigg\{C_b(t_0)\left[-ie^{i(\delta t_0+\phi)}\sin\theta\sin\left(\frac{\Omega_R\tau}{2}\right)\right] + \\ + C_a(t_0)\left[\cos\left(\frac{\Omega_R\tau}{2}\right) + i\cos\theta\,\sin\left(\frac{\Omega_R\tau}{2}\right)\right]\Bigg\}. \tag{3.24}$$

For $|\delta| \ll \Omega_R$ one has

$$C_b(t_0+\tau) = e^{-i\delta\tau/2}\left[C_b(t_0)\cos\left(\frac{\Omega_R\tau}{2}\right) - i\,C_a e^{-i(\delta t_0+\phi)}\sin\left(\frac{\Omega_R\tau}{2}\right)\right]; \tag{3.25}$$

$$C_a(t_0+\tau) = e^{+i\delta\tau/2}\left[-iC_b(t_0)e^{i(\delta t_0+\phi)}\sin\left(\frac{\Omega_R\tau}{2}\right) + C_a(t_0)\cos\left(\frac{\Omega_R\tau}{2}\right)\right]. \tag{3.26}$$

For a pulse with duration $\tau = \pi/\Omega_R$ the evolution operator corresponds to a π-pulse (Sorrentino et al., 2014). In this regime, the pulse performs a complete population inversion between the two internal states $|a\rangle$ and $|b\rangle$, apart from well-defined phase factors that depend on the detuning δ, the laser phase ϕ, and the pulse start time t_0. Consequently, the amplitude evolution simplifies significantly, since $\cos\left(\frac{\Omega_R\tau}{2}\right) = \cos\left(\frac{\pi}{2}\right) = 0$ and $\sin\left(\frac{\Omega_R\tau}{2}\right) = \sin\left(\frac{\pi}{2}\right) = 1$. Substituting these values into the general expressions for the amplitudes yields the well-known inversion of the occupation of levels, associated with a pulse duration of τ:

$$C_b(t_0+\tau) = -i\,C_a(t_0)\,e^{-i(\delta t_0+\phi)}e^{-i\delta\tau/2}; \tag{3.27}$$

$$C_a(t_0+\tau) = -i\,C_b(t_0)\,e^{i(\delta t_0+\phi)}e^{i\delta\tau/2} \tag{3.28}$$

Eqs. 3.27 and 3.28 provide the evolution of the coefficients C_a and C_b. They must be applied individually to each pulse of the sequence that will be momentarily introduced, considering the $\pi/2 - \pi - \pi/2$ pulse sequence. Therefore, the time t_0 indicated in Eqs. 3.27 and 3.28 represents the moment when each pulse initiates. In this way, the evolution of the coefficients for each quantum state over time can be determined based on the starting times of each pulse, as described for the following pulse sequence.

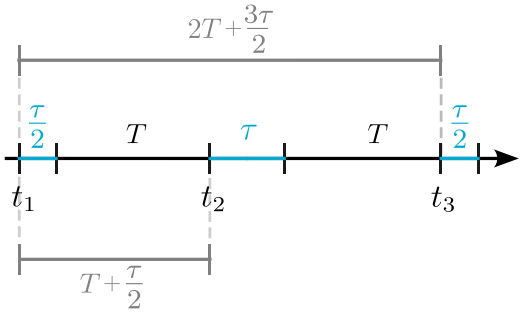

Figure 3.5: Pulse sequence discussed in the text. The first pulse, with a duration of $\tau/2$, starts at time t_1. The second pulse, with a duration of τ, starts at time $t_2 = t_1 + T + \tau/2$. The third pulse starts at $t_3 = t_1 + 2T + 3\tau/2$ with a duration of $\tau/2$.

The pulse sequence is defined as displayed in Figure 3.5. The first pulse, which has a duration of $\tau/2$ and a phase ϕ_1, occurs at time t_1. The second pulse, with a duration τ and phase ϕ_2, occurs at time $t_2 = t_1 + T + \tau/2$. Finally, the third pulse is again a $\pi/2$ pulse (with duration $\tau/2$ and phase ϕ_3), occurring at $t_3 = t_1 + 2T + 3\tau/2$. Based on this sequence, and using Eqs. (3.27) and (3.28), together with the initial conditions $C_a(t_1) = 1$ and $C_b(t_1) = 0$, the atomic state at time $t_1 + \tau/2$ can be determined as follows:

$$C_b\left(t_1 + \frac{\tau}{2}\right) = \frac{e^{-i\delta\tau/4}}{\sqrt{2}}\left[-i\, e^{-i(\delta t_1 + \phi_1)}\right];$$
$$C_a\left(t_1 + \frac{\tau}{2}\right) = \frac{e^{+i\delta\tau/4}}{\sqrt{2}}.$$

Assuming that the amplitude of the ground state at time t_2 ($C_a(t_2)$) is equal to the amplitude of the ground state at time $t_1 + \frac{\tau}{2}$, and similarly, the amplitude of the excited state at time t_2 ($C_b(t_2)$) is equal to the amplitude of the excited state at time

$t_1 + \frac{\tau}{2}$, we can deduce the following expressions for the excited state at time $t_2 + \tau$:

$$C_b(t_2+\tau) = -i\,\frac{e^{-i\delta\tau/4}e^{-i(\delta t_2+\phi_2)}}{\sqrt{2}}$$
$$C_a(t_2+\tau) = -\frac{e^{+i\delta\tau/4}}{\sqrt{2}}\left[e^{-i(\delta t_1+\phi_1)}e^{i(\delta t_2+\phi_2)}\right]$$

Similarly, considering that the amplitudes of the ground state at time t_3 ($C_a(t_3)$) and the excited state at the same time ($C_b(t_3)$) are equal to the corresponding amplitudes at time $t_2+\tau$, namely $C_a(t_2+\tau)$ and $C_b(t_2+\tau)$, respectively, it follows that:

$$C_b\left(t_3+\frac{\tau}{2}\right) = -\frac{ie^{-\delta\tau/2}}{2}\left[1-e^{+\delta\tau/2}e^{-i\Delta\phi}\right].$$

Finally, the probability of measuring the excited state, given by the amplitude $C_b(t_3+\frac{\tau}{2})$, is given by:

$$\left|C_b\left(t_3+\frac{\tau}{2}\right)\right|^2 = \frac{1}{2}\left[1-\cos\left(\Delta\phi-\delta\tau/2\right)\right] \tag{3.29}$$

where $\Delta\phi = \phi_1 - 2\phi_2 + \phi_3$. Note that (3.29) shows that the probability of the atom being in the excited state at the end of the $\pi/2-\pi-\pi/2$ pulse sequence depends on the phases associated with each of these pulses (ϕ_1, ϕ_2 and ϕ_3).

To summarize, the primary objective of this section was to introduce, in a possibly pedagogical manner, the basic physical principles governing the atom–light interaction. A two-level model was presented to elucidate the physical and mathematical concepts involved in the description of the interaction between light and atoms, which helps to clarify how laser pulses induce transitions between the internal states of atoms. However, the two-level framework does not take into account the kinetic energy of the atom nor the spatial dependence of the electric field and therefore does not fully describe the operation of a quantum gravimeter. In atomic interferometers, the motion of the atom as a whole is essential, since the laser field generates position-dependent phases and transfers momentum to the atoms. A complete understanding of the quantum gravimeter requires the inclusion of the kinetic energy term in the Hamiltonian, which is accomplished in the three-level model presented in the following section.

3.2 Three-level system

Let us consider a three-level system composed of two energy states ($|a\rangle$ and $|b\rangle$) and a metastable state ($|i\rangle$). The atom is initially in the ground state $|a\rangle$ with momentum $\mathbf{p}$.

Upon interacting with a pair of counter-propagating laser beams described by the electric field

$$\mathbf{E} = \mathbf{E}_1 \cos\left(\mathbf{k}_1 \cdot \mathbf{x} - \omega_1 t + \phi_1\right) + \mathbf{E}_2 \cos\left(\mathbf{k}_2 \cdot \mathbf{x} - \omega_2 t + \phi_2\right) \tag{3.30}$$

the atom absorbs a photon and is transiently driven to the intermediate state $|i\rangle$ (with momentum $\mathbf{p} + \hbar\mathbf{k}_1$) and subsequently emits a photon with momentum $\hbar\mathbf{k}_2$, while simultaneously reaching the excited state $|b\rangle$ with momentum $\mathbf{p} + \hbar(\mathbf{k}_1 - \mathbf{k}_2)$. For counter-propagating lasers, we assume that the wave vectors satisfy the condition $\mathbf{k}_1 \approx -\mathbf{k}_2$ (Lamporesi et al., 2008). As a result, the effective wavevector of the photon interaction is given by

$$\mathbf{k}_{\text{eff}} = \mathbf{k}_1 - \mathbf{k}_2 \approx 2\mathbf{k}_1.$$

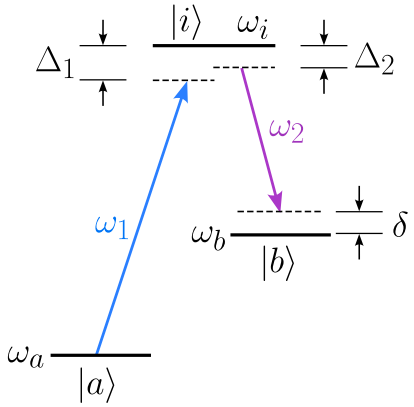

Figure 3.6: Schematic representation of a three-level system.

Each atomic state can be described as a tensor product between the Hilbert space of the internal degrees of freedom (energy levels) and the Hilbert space of the external degrees of freedom (momentum):

$$\mathcal{H}_{\text{total}} = \mathcal{H}_{\text{internal}} \otimes \mathcal{H}_{\text{external}}$$

and, according to the orthonormality of the internal bases, we have (Young et al., 1997)

$$\begin{aligned} |a,\, \mathbf{p}\rangle &= |a\rangle \otimes |\mathbf{p}\rangle, \\ |i,\, \mathbf{p} + \hbar\mathbf{k}_1\rangle &= |i\rangle \otimes |\mathbf{p} + \hbar\mathbf{k_1}\rangle, \\ |b,\, \mathbf{p} + \hbar\mathbf{k}\rangle &= |b\rangle \otimes |\mathbf{p} + \hbar\left(\mathbf{k_1} - \mathbf{k_2}\right)\rangle. \end{aligned}$$

The presence of three energy levels is not the only difference with respect to the previous section. In the present case, the e.m. field depends explicitly on position, as evidenced by the terms proportional to $\mathbf{k}_1 \cdot \mathbf{x}$ and $\mathbf{k}_2 \cdot \mathbf{x}$ appearing in Eq. (3.30). As a result, the Hamiltonian describing the system becomes

$$\hat{H} = \frac{\hat{\mathbf{p}}^2}{2m} + \hbar w_a |a\rangle\langle a| + \hbar w_i |i\rangle\langle i| + \hbar w_b |b\rangle\langle b| - \mathbf{d} \cdot \mathbf{E}. \tag{3.31}$$

This Hamiltonian includes two additional terms compared with the two-level case: the kinetic contribution $\hat{\mathbf{p}}^2/2m$, and the term $\hbar w_i |i\rangle\langle i|$". The former represents the kinetic energy of the particle, with momentum operator $\hat{\mathbf{p}}$ and mass m, whereas the latter corresponds to the internal energy associated with the metastable state $|i\rangle$.

The quantum state at time t can be written as:

$$\begin{aligned} |\psi(t)\rangle = & C_{a,\mathbf{p}}\, e^{-i\left(w_a + \frac{|\mathbf{p}|^2}{2m\hbar}\right)t} |a,\, \mathbf{p}\rangle + \\ & + C_{i,\mathbf{p}+\hbar\mathbf{k}_1}\, e^{-i\left(\omega_i + \frac{|\mathbf{p}+\hbar\mathbf{k}_1|^2}{2m\hbar}\right)t} |i,\, \mathbf{p} + \hbar\mathbf{k}_1\rangle + \\ & + C_{b,\mathbf{p}+\hbar(\mathbf{k}_1-\mathbf{k}_2)}\, e^{-i\left(w_b + \frac{|\mathbf{p}+\hbar\mathbf{k}|^2}{2m\hbar}\right)t} |b,\, \mathbf{p} + \hbar\,(\mathbf{k}_1 - \mathbf{k}_2)\rangle. \end{aligned}$$

Multiplying $|\dot{\psi}(t)\rangle$ by $i\hbar$ and caluclating its time derivative one gets

$$\begin{aligned} i\hbar\frac{\partial}{\partial t}|\psi(t)\rangle = & i\hbar\,\dot{C}_{a,\mathbf{p}}\, e^{-i\left(w_a + \frac{|\mathbf{p}|^2}{2m\hbar}\right)t} |a,\, \mathbf{p}\rangle + \\ & + i\hbar\,\dot{C}_{i,\mathbf{p}+\hbar\mathbf{k}_1}\, e^{-i\left(\omega_i + \frac{|\mathbf{p}+\hbar\mathbf{k}_1|^2}{2m\hbar}\right)t} |i,\, \mathbf{p} + \hbar\mathbf{k}_1\rangle + \\ & + i\hbar\,\dot{C}_{b,\mathbf{p}+\hbar(\mathbf{k}_1-\mathbf{k}_2)}\, e^{-i\left(w_b + \frac{|\mathbf{p}+\hbar\mathbf{k}|^2}{2m\hbar}\right)t} |b,\, \mathbf{p} + \hbar\,(\mathbf{k}_1 - \mathbf{k}_2)\rangle + \\ & + \left(\hat{H}_0 + \frac{\hat{\mathbf{p}}^2}{2m}\right) |\psi(t)\rangle, \end{aligned}$$

where $\hat{H}_0$ is given by (3.3). Taking into account Eq. (3.31) and using the Schrödinger equation, one finds

$$\begin{aligned} \hat{H}_{\text{int}}|\psi(t)\rangle = & i\hbar\,\dot{C}_{a,\mathbf{p}}\, e^{-i\left(w_a + \frac{|\mathbf{p}|^2}{2m\hbar}\right)t} |a,\, \mathbf{p}\rangle + \\ & + i\hbar\,\dot{C}_{i,\mathbf{p}+\hbar\mathbf{k}_1}\, e^{-i\left(\omega_i + \frac{|\mathbf{p}+\hbar\mathbf{k}_1|^2}{2m\hbar}\right)t} |i,\, \mathbf{p} + \hbar\mathbf{k}_1\rangle + \\ & + i\hbar\,\dot{C}_{b,\mathbf{p}+\hbar(\mathbf{k}_1-\mathbf{k}_2)}\, e^{-i\left(w_b + \frac{|\mathbf{p}+\hbar\mathbf{k}|^2}{2m\hbar}\right)t} |b,\, \mathbf{p} + \hbar\,(\mathbf{k}_1 - \mathbf{k}_2)\rangle. \end{aligned}$$

By multiplying the previous equation by $\langle a|$, $\langle b|$ and $\langle i|$, one obtains, respectively:

$$\langle a|\hat{H}_{\text{int}}|\psi(t)\rangle = i\hbar\,\dot{C}_{a,\mathbf{p}}\,e^{-i\left(w_a+\frac{|\mathbf{p}|^2}{2m\hbar}\right)t}|\mathbf{p}\rangle \tag{3.32}$$

$$\langle i|\hat{H}_{\text{int}}|\psi(t)\rangle = i\hbar\,\dot{C}_{i,\mathbf{p}+\hbar\mathbf{k}_1}\,e^{-i\left(\omega_i+\frac{|\mathbf{p}+\hbar\mathbf{k}_1|^2}{2m\hbar}\right)t}|\mathbf{p}+\hbar\mathbf{k_1}\rangle \tag{3.33}$$

$$\langle b|\hat{H}_{\text{int}}|\psi(t)\rangle = i\hbar\,\dot{C}_{b,\mathbf{p}+\hbar(\mathbf{k}_1-\mathbf{k}_2)}\,e^{-i\left(w_b+\frac{|\mathbf{p}+\hbar\mathbf{k}|^2}{2m\hbar}\right)t}|\mathbf{p}+\hbar\left(\mathbf{k_1}-\mathbf{k_2}\right)\rangle \tag{3.34}$$

The single-photon detunings Δ_1 and Δ_2, corresponding to the frequencies ω_1 and ω_2 (Figure 3.6), are defined as (Chu, 2001; Tinsley, 2019):

$$\Delta_1 \equiv \omega_1-(w_i-w_a)+\frac{|\mathbf{p}|^2-|\mathbf{p}+\hbar\mathbf{k}_1|^2}{2m\hbar}, \tag{3.35}$$

$$\Delta_2 \equiv \omega_2-(w_i-w_b)+\frac{|\mathbf{p}+\hbar\left(\mathbf{k}_1-\mathbf{k}_2\right)|^2-|\mathbf{p}+\hbar\mathbf{k}_1|^2}{2m\hbar}. \tag{3.36}$$

Applying – as in the previous section – the RWA, which disregards the terms with rapidly oscillating exponentials in Eqs. (3.32), (3.33) and (3.34), we obtain the following differential equations:

$$i\dot{C}_{a,\mathbf{p}} = \frac{\Omega_{ai}^*}{2}C_{i,\mathbf{p}+\hbar\mathbf{k}_1}\,e^{+i\Delta_1 t}e^{-i\phi_1} \tag{3.37}$$

$$i\dot{C}_{b,\mathbf{p}+\hbar(\mathbf{k}_1-\mathbf{k}_2)} = \frac{\Omega_{bi}^*}{2}C_{i,\mathbf{p}+\hbar\mathbf{k}_1}\,e^{+i\Delta_2 t}e^{-i\phi_2} \tag{3.38}$$

$$i\dot{C}_{i,\mathbf{p}+\hbar\mathbf{k}_1} = \frac{\Omega_{ai}}{2}C_{a,\mathbf{p}}\,e^{-i\Delta_1 t}e^{+i\phi_1}+\frac{\Omega_{bi}}{2}C_{b,\mathbf{p}+\hbar(\mathbf{k}_1-\mathbf{k}_2)}\,e^{-i\Delta_2 t}e^{+i\phi_2} \tag{3.39}$$

where $\Omega_{bi}=\frac{\langle i|-\mathbf{d}\cdot\mathbf{E}_2|b\rangle}{\hbar}$ and $\Omega_{ai}=\frac{\langle i|-\mathbf{d}\cdot\mathbf{E}_1|a\rangle}{\hbar}$.

If we assume that the amplitude terms decay much more slowly than the exponential terms, then the amplitudes can be considered time-independent and, therefore, removed from the integral (Tinsley, 2019):

$$i\int_{t_0}^{t}\dot{C}_{i,\mathbf{p}+\hbar\mathbf{k}_1}dt' = \frac{\Omega_{ai}}{2}C_{a,\mathbf{p}}\,e^{+i\phi_1}\int_{t_0}^{t}e^{-i\Delta_1 t}+\frac{\Omega_{bi}}{2}C_{b,\mathbf{p}+\hbar(\mathbf{k}_1-\mathbf{k}_2)}\,e^{+i\phi_2}\int_{t_0}^{t}e^{-i\Delta_2 t}dt'.$$

Integrating, we obtain:

$$i\dot{C}_{b,\mathbf{p}+\hbar(\mathbf{k}_1-\mathbf{k}_2)} = \frac{\Omega_{ai}\Omega_{bi}^*}{4\Delta_1}\left(e^{-i(\Delta_1-\Delta_2)t}-e^{i\Delta_2 t}\right)e^{i\phi}+\frac{|\Omega_{bi}|^2}{4\Delta_2}\left(1-e^{i\Delta_2 t}\right)C_{b,\mathbf{p}+\hbar(\mathbf{k}_1-\mathbf{k}_2)} \tag{3.40}$$

By substituting (3.40) into Eqs. (3.37) and (3.38), the latter become independent of the coefficient $C_{i,\mathbf{p}+\hbar\mathbf{k}_1}$, resulting in a system of coupled differential equations depending on two variables: ($C_{a,\mathbf{p}}$ and $C_{b,\mathbf{p}+\hbar(\mathbf{k}_1-\mathbf{k}_2)}$):

$$i\dot{C}_{a,\mathbf{p}} = \frac{|\Omega_{ai}|^2}{4\Delta_1}\left(1-e^{i\Delta_1 t}\right)C_{a,\mathbf{p}} + \frac{\Omega_{bi}\Omega_{ai}^*}{4\Delta_2}\left(e^{i(\Delta_1-\Delta_2)t}-e^{i\Delta_1 t}\right)e^{-i(\phi_1-\phi_2)}C_{b,\mathbf{p}+\hbar(\mathbf{k}_1-\mathbf{k}_2)} \tag{3.41}$$

$$i\dot{C}_{b,\mathbf{p}+\hbar(\mathbf{k}_1-\mathbf{k}_2)} = \frac{\Omega_{ai}\Omega_{bi}^*}{4\Delta_1}\left(e^{-i(\Delta_1-\Delta_2)t}-e^{i\Delta_2 t}\right)e^{i(\phi_1-\phi_2)} + \frac{|\Omega_{bi}|^2}{4\Delta_2}\left(1-e^{i\Delta_2 t}\right)C_{b,\mathbf{p}+\hbar(\mathbf{k}_1-\mathbf{k}_2)} \tag{3.42}$$

Unlike the case discussed in Section 3.1, the detuning δ is a function of momentum and can be defined as (Young et al., 1997; Tinsley, 2019):

$$\delta = \Delta_1 - \Delta_2 = \omega_1 - \omega_2 + \left(\omega_{ba} + \frac{\mathbf{p}\cdot\mathbf{k}_{\text{eff}}}{m} + \frac{\hbar|\mathbf{k}_{\text{eff}}|^2}{2m}\right).$$

Using this definition, and applying the RWA once again, the expressions (3.41) and (3.42) become:

$$i\dot{C}_{b,\mathbf{p}+\hbar(\mathbf{k}_1-\mathbf{k}_2)} = \frac{\Omega_{ai}\Omega_{bi}^*}{4\Delta_1}e^{-i\delta t}e^{i(\phi_1-\phi_2)} + \frac{|\Omega_{bi}|^2}{4\Delta_2}C_{b,\mathbf{p}+\hbar(\mathbf{k}_1-\mathbf{k}_2)} \tag{3.43}$$

$$i\dot{C}_{a,\mathbf{p}} = \frac{|\Omega_{ai}|^2}{4\Delta_1}C_{a,\mathbf{p}} + \frac{\Omega_{bi}\Omega_{ai}^*}{4\Delta_2}e^{i\Delta_1 t}e^{-i(\phi_1-\phi_2)}C_{b,\mathbf{p}+\hbar(\mathbf{k}_1-\mathbf{k}_2)} \tag{3.44}$$

For nearly-resonant Raman transitions, the terms Δ_1 and Δ_2 become approximately equal, as both laser interactions involve very close internal levels and small momentum differences. Therefore, $\Delta_1 \approx \Delta_2 = \Delta$. With this approximation, Eqs. (3.43) and (3.44) can be written in matrix form as

$$i\hbar\begin{pmatrix}\dot{C}_{b,\mathbf{p}+\hbar(\mathbf{k}_1-\mathbf{k}_2)}\\ \\ \dot{C}_{a,\mathbf{p}}\end{pmatrix} = \hbar\begin{pmatrix}\Omega_b^{AC} & \Omega_{\text{eff}}\,e^{-i(\delta\,t+\phi)}/2\\ \\ \Omega_{\text{eff}}^*\,e^{+i(\delta\,t+\phi)}/2 & \Omega_a^{AC}\end{pmatrix}\begin{pmatrix}C_{b,\mathbf{p}+\hbar(\mathbf{k}_1-\mathbf{k}_2)}\\ \\ C_{a,\mathbf{p}}\end{pmatrix}, \tag{3.45}$$

with the parameters defined as:

$$\begin{aligned}\Omega_b^{AC} &= \frac{\Omega_{ai}\Omega_{bi}^*}{4\Delta}\\ \Omega_a^{AC} &= \frac{\Omega_{bi}\Omega_{ai}^*}{4\Delta_2}\\ \Omega_{\text{eff}} &= \frac{\Omega_{ai}\Omega_{bi}^*}{4\Delta}\\ \phi &= \phi_2 - \phi_1\end{aligned}$$

Therefore, from Eq. (3.78), the interaction Hamiltonian ($\hat{H}_{\text{int}}$) can be written as:

$$\hat{H}_{\text{int}} = \hbar \begin{pmatrix} \Omega_b^{AC} & \Omega_{\text{eff}}\, e^{-i(\delta\, t+\phi)}/2 \\ \Omega_{\text{eff}}^*\, e^{+i(\delta\, t+\phi)}/2 & \Omega_a^{AC} \end{pmatrix}. \tag{3.46}$$

Subtracting a constant energy term $(\Omega_b^{AC}+\Omega_a^{AC})/2$ (of course multiplied by the 2×2 identity matrix) from the Hamiltonian (3.46), one gets:

$$\hat{H}_{\text{int}} = \frac{\hbar}{2} \begin{pmatrix} (\Omega_b^{AC} - \Omega_a^{AC}) & \Omega_{\text{eff}}\, e^{-i(\delta\, t+\phi)} \\ \Omega_{\text{eff}}^*\, e^{+i(\delta\, t+\phi)} & -(\Omega_b^{AC} - \Omega_a^{AC}) \end{pmatrix}. \tag{3.47}$$

Defining $\delta^{AC} = \Omega_b^{AC} - \Omega_a^{AC}$, and applying the rotating frame transformation given by (3.14), we get:

$$\hat{H}_R = \frac{\hbar}{2} \begin{pmatrix} -\left(\delta - \delta^{AC}\right) & \Omega_{\text{eff}}\, e^{-i\phi} \\ \Omega_{\text{eff}}^*\, e^{+i\phi} & \left(\delta - \delta^{AC}\right) \end{pmatrix}. \tag{3.48}$$

The eigenvalues of this matrix are given by:

$$\lambda \equiv \pm\frac{\hbar\Omega_R}{2} \equiv \pm\frac{\hbar\sqrt{|\Omega_{\text{eff}}|^2 + (\delta - \delta^{AC})^2}}{2} \tag{3.49}$$

Proceeding as in Section 3.1 and using Eq. (3.21), we obtain the following equations

for the time evolution of $C_{b,\mathbf{p}+\hbar\mathbf{k}_{\text{eff}}}$ and $C_{a,\mathbf{p}}$:

$$C_{b,\mathbf{p}+\hbar\mathbf{k}_{\text{eff}}}(t_0+\tau) = e^{-i\left(\Omega_b^{AC}+\Omega_a^{AC}\right)\tau/2}\, e^{-i\delta\tau/2}\Bigg\{C_{b,\mathbf{p}+\hbar\mathbf{k}_{\text{eff}}}(t_0)\left[\cos\left(\frac{\Omega_R\tau}{2}\right) - i\cos\theta\,\sin\left(\frac{\Omega_R\tau}{2}\right)\right] + \\ + C_{a,\mathbf{p}}(t_0)e^{-i(\delta t_0+\phi)}(-i)\sin\theta\sin\left(\frac{\Omega_R\tau}{2}\right)\Bigg\}; \tag{3.50}$$

$$C_{a,\mathbf{p}}(t_0+\tau) = e^{-i\left(\Omega_b^{AC}+\Omega_a^{AC}\right)\tau/2}\, e^{+i\delta\tau/2}\Bigg\{C_{b,\mathbf{p}+\hbar\mathbf{k}_{\text{eff}}}(t_0)\left[-ie^{i(\delta t_0+\phi)}\sin\theta\sin\left(\frac{\Omega_R\tau}{2}\right)\right] + \\ + C_{a,\mathbf{p}}(t_0)\left[\cos\left(\frac{\Omega_R\tau}{2}\right) + i\cos\theta\,\sin\left(\frac{\Omega_R\tau}{2}\right)\right]\Bigg\}. \tag{3.51}$$

Therefore, for a π-pulse of duration τ, we obtain:

$$C_{b,\mathbf{p}+\hbar\mathbf{k}_{\text{eff}}}(t_0+\tau) = -ie^{-i\left(\Omega_b^{AC}+\Omega_a^{AC}\right)\tau/2}\, e^{-i\delta\tau/2}e^{-i(\delta t_0+\phi)}C_{a,\mathbf{p}}(t_0), \tag{3.52}$$

$$C_{a,\mathbf{p}}(t_0+\tau) = -ie^{-i\left(\Omega_b^{AC}+\Omega_a^{AC}\right)\tau/2}\, e^{+i\delta\tau/2}\, e^{i(\delta t_0+\phi)}C_{b,\mathbf{p}+\hbar\mathbf{k}_{\text{eff}}}(t_0), \tag{3.53}$$

while for a $\pi/2$-pulse of duration $\tau/2$ one gets:

$$C_{b,\mathbf{p}+\hbar\mathbf{k}_{\text{eff}}}(t_0+\tau/2) = e^{-i\left(\Omega_b^{AC}+\Omega_a^{AC}\right)\tau/2}\, e^{-i\delta\tau/2}\left[C_{b,\mathbf{p}+\hbar\mathbf{k}_{\text{eff}}}(t_0) \;-\; iC_{a,\mathbf{p}}(t_0)e^{-i(\delta t_0+\phi)}\right]/\sqrt{2}, \tag{3.54}$$

$$C_{a,\mathbf{p}}(t_0+\tau/2) = e^{-i\left(\Omega_b^{AC}+\Omega_a^{AC}\right)\tau/2}\, e^{+i\delta\tau/2}\left[-iC_{b,\mathbf{p}+\hbar\mathbf{k}_{\text{eff}}}(t_0)e^{i(\delta t_0+\phi)} + C_{a,\mathbf{p}}(t_0)\right]/\sqrt{2}. \tag{3.55}$$

Assuming that at time t_1 we have $C_{a,\mathbf{p}}(t_1) = 1$ and $C_{b,\mathbf{p}+\hbar\mathbf{k}_{\text{eff}}}(t_1) = 0$, and considering that the first $\pi/2$ pulse has duration $\tau/2$, acting from t_1 to $t_1+\tau/2$, we obtain the time evolution of $C_{b,\mathbf{p}+\hbar\mathbf{k}_{\text{eff}}}$ and $C_{a,\mathbf{p}}$ after the application of this pulse:

$$C_{b,\mathbf{p}+\hbar\mathbf{k}_{\text{eff}}}(t_1+\tau/2) = -ie^{-i\left(\Omega_b^{AC}+\Omega_a^{AC}\right)\tau/4}\, e^{-i\delta\tau/4}e^{-i(\delta t_1+\phi_1)}/\sqrt{2}, \tag{3.56}$$

$$C_{a,\mathbf{p}}(t_1+\tau/2) = e^{-i\left(\Omega_b^{AC}+\Omega_a^{AC}\right)\tau/4}\, e^{+i\delta\tau/4}/\sqrt{2}. \tag{3.57}$$

If we assume that no additional phase shift is accumulated along the propagation of the pulses (as we will discuss in the next section), then at time t_2 we have $C_{b,\mathbf{p}+\hbar\mathbf{k}_{\text{eff}}}(t_2) = C_{b,\mathbf{p}+\hbar\mathbf{k}_{\text{eff}}}(t_1+\tau/2)$ and $C_{a,\mathbf{p}}(t_2) = C_{a,\mathbf{p}}(t_1+\tau/2)$. Therefore, the time

evolution of the amplitudes after the second $\pi/2$ pulse, which takes place between t_2 and $t_2+\tau$, is given by:

$$C_{b,\mathbf{p}+\hbar\mathbf{k}_{\text{eff}}}(t_2+\tau) = -ie^{-i\left(\Omega_b^{AC}+\Omega_a^{AC}\right)3\tau/4}\, e^{-i\delta\tau/4} e^{-i(\delta t_2+\phi_2)}/\sqrt{2}, \tag{3.58}$$

$$C_{a,\mathbf{p}}(t_2+\tau) = -\, e^{-i\left(\Omega_b^{AC}+\Omega_a^{AC}\right)3\tau/4}\, e^{+i\delta\tau/4}\, e^{i(\delta t_2+\phi_2)} e^{-i(\delta t_1+\phi_1)}/\sqrt{2}. \tag{3.59}$$

Finally, considering the last $\pi/2$ pulse, with duration $\tau/2$, applied from t_3 to $t_3+\tau/2$, we obtain the final evolution of $C_{b,\mathbf{p}+\hbar\mathbf{k}_{\text{eff}}}$ after this pulse:

$$C_{b,\mathbf{p}+\hbar\mathbf{k}_{\text{eff}}}(t_3+\tau/2) = -\frac{i}{2} e^{-i\left(\Omega_b^{AC}+\Omega_a^{AC}\right)\tau}\, e^{-i\delta\tau/2}\left[1 - e^{+i\delta\tau/2}\, e^{\Delta\phi}\right]. \tag{3.60}$$

It follows that the probability of finding the system in the excited state ($C_{b,\mathbf{p}+\hbar\mathbf{k}_{\text{eff}}}$) after the third pulse is given by:

$$\left|C_{b,\mathbf{p}+\hbar\mathbf{k}_{\text{eff}}}(t_3+\tau/2)\right|^2 = \frac{1}{2}\left[1-\cos\left(\Delta\phi-\delta\tau/2\right)\right]. \tag{3.61}$$

It is noteworthy that Eq. (3.61) is identical to (3.29), obtained in the two-level case (Section 3.1). This indicates that the population probabilities in the three-level system in the considered approximations the same as those predicted by the two-level approximation.

3.3 Gravity Measurement

In the previous section, it was shown that the probability of detecting the atom in the excited state after the sequence of $\pi/2-\pi-\pi/2$ pulses is given by Eq. (3.61). Up to this point, the effect of gravitational acceleration had not been taken into account. Therefore, the interferometric phase $\Delta\phi$ is determined by the phases (ϕ_1, ϕ_2 and ϕ_3) of the $\pi/2-\pi-\pi/2$ pulse sequence. The final contribution – in absence of gravity (i.e., $g=0$) – arises from the following sum of the phases generated by the three laser pulses:

$$\Delta\phi_{\text{laser}} = \phi_1 - 2\phi_2 + \phi_3. \tag{3.62}$$

However, in the presence of a gravitational potential, the particle undergoes a continuous variation in its transition frequency, which introduces an additional phase shift at the output of the interferometer. In other words, the total measured phase ($\Delta\phi_{\text{tot}}$) does not depend only on the pulse phases ϕ_1, ϕ_2, and ϕ_3 and there is a phase

shift $\Delta\phi_{\text{grav}}$ induced by the action of gravity on the trajectory of the particle. Thus, for pedagogical clarity, the total phase can be written as

$$\Delta\phi_{\text{tot}} = \Delta\phi_{\text{laser}} + \Delta\phi_{\text{grav}}, \tag{3.63}$$

where $\Delta\phi_{\text{laser}}$ is given by (3.62).

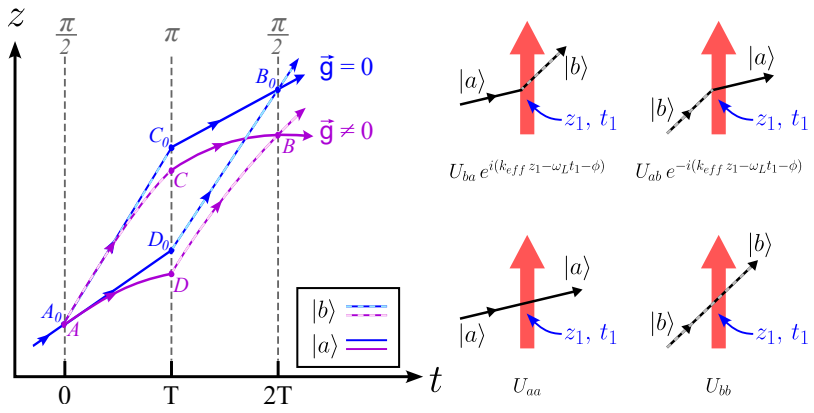

Figure 3.7: Left: an illustration is shown of the trajectory described by the atoms in the interferometer, subjected to the $\pi/2 - \pi - \pi/2$ pulse sequence, considering the cases of absence (blue lines) and presence (purple lines) of a gravitational field. Right: a representation is provided of the four types of interaction between an atom and the laser beam (red arrows) with frequency ω_L and wavevector k_{eff} (this interaction occurring at a time t_1 in a position z_1): (top left) the atom absorbs a photon, gaining momentum $\hbar k_{\text{eff}}$ and transitioning from state $|a\rangle$ to state $|b\rangle$; (top right) the atom emits a photon, losing momentum $\hbar k_{\text{eff}}$ and decaying from state $|b\rangle$ to state $|a\rangle$; (bottom left) the atom remains in state $|a\rangle$; (bottom right) the atom remains in state $|b\rangle$.

To understand how to determine $\Delta\phi_{\text{grav}}$ we can proceed in the following way. In the absence of gravity, the trajectories described by the atoms are straight lines, since they maintain constant velocity in each arm of the interferometer. The only velocity changes arise from the absorption or emission of photons during the Raman pulses. Nevertheless, in the presence of a gravitational field, the atomic velocities vary continuously along their trajectories due to the gravitational acceleration experienced by the atoms. As a consequence, the paths become curved in the "depth × time" diagram (Figure 3.7). This curvature introduces an additional phase shift, denoted by $\Delta\phi_{\text{path}}$ (Storey and Cohen-Tannoudji, 1994; Bhardwaj et al., 2024), which can be

determined by

$$\Delta\phi_{\text{path}} = \frac{S_{cl}}{\hbar}, \tag{3.64}$$

where S_{cl} represents the action evaluated along the classical trajectories (Chu, 2001). A derivation of (3.64) is in Appendix B and in the next discussion we closely follow Storey and Cohen-Tannoudji (1994).

The classical action from a point z_1 (at a time t_1) to a point z_2 (at a time t_2) is defined as the time integral of the Lagrangian $L(z, \dot{z})$ along the atomic trajectory:

$$S_{cl}\left(z_2\, t_2, z_1\, t_1\right) = \int_{t_1}^{t_2} L(z, \dot{z})\, dt.$$

The Lagrangian $L(z, \dot{z})$ is written as

$$L(z(t), \dot{z}(t)) = \frac{1}{2} m\dot{z}(t)^2 - mgz(t),$$

where $z(t)$ and $\dot{z}(t)$ are the equations of motion of the particle, which initially (at time t_1) has velocity v_1 at position z_1:

$$\begin{aligned} z(t) &= z_1 + v_1(t - t_1) - \frac{1}{2} g(t - t_1)^2, \\ \dot{z}(t) &= v_1 - g(t - t_1). \end{aligned}$$

Based on this, the solution for the classical action $S_{cl}\left(z_2\, t_2, z_1\, t_1\right)$, is given by (Storey and Cohen-Tannoudji, 1994)

$$S_{cl}\left(z_2\, t_2, z_1\, t_1\right) = \frac{m}{2} \frac{\left(z_2 - z_1\right)^2}{\left(t_2 - t_1\right)} - \frac{m\, g}{2} \left(t_2 - t_1\right) \left(z_2 + z_1\right) - \frac{mg^2}{24} \left(t_2 - t_1\right)^3. \tag{3.65}$$

Therefore, the total contribution to the phase difference between the two arms due to propagation, according to the geometry described in the left part of Figure 3.7 is (Storey and Cohen-Tannoudji, 1994):

$$\begin{aligned} \Delta\phi_{\text{path}} &= \left\{\left[S_{cl}\left(AC\right) - S_{cl}\left(AD\right)\right] + \left[S_{cl}\left(CB\right) - S_{cl}\left(DB\right)\right]\right\} / \hbar \\ &= \frac{m}{T\hbar} \left(z_C - z_D\right) \left[z_C + z_D - z_A - z_B - g\, T^2\right] \end{aligned}$$

Notice that we are denoting with z_A, z_B, z_C, z_D the positions in which the atom is at the different pulses according their location in Figure 3.7, while the corresponding

quantities in absence of gravity with a further index $_0$, also indicated in Figure 3.7. By geometric considerations

$$z_{D_0} - z_D = (1/2)gT^2 = z_{C_0} - z_C,$$

$$z_{B_0} - z_B = 2gT^2.$$

Moreover, since $A_0B_0C_0D_0$ is a parallelogram, this implies that the phase difference along the two arms in absence of gravity has to be vanishing. It follows

$$z_C + z_D - z_A - z_B - g\,T^2 = z_{C_0} + z_{D_0} - z_{A_0} - z_{B_0} = 0,$$

from which $\Delta\phi_{\text{path}} = 0$ and

$$g\,T^2 = z_C + z_D - z_A - z_B. \tag{3.66}$$

The fact that $\Delta\phi_{\text{path}} = 0$ does not imply that $\Delta\phi_{\text{grav}}$, as defined in (3.63) with $\Delta\phi_{\text{laser}}$ given by Eq. (3.62), is vanishing as well, as we are going to discuss now.

Let analyze the state transitions induced by the laser pulses. The interactions between the atom and the Raman pulses can occur in four distinct ways (right part of Figure 3.7):

- The atom absorbs a photon, acquiring a momentum $\hbar k$ and undergoing a transition from the state $|a\rangle$ to the state $|b\rangle$;
- The atom emits a photon, losing a momentum $\hbar k$ and decaying from the state $|b\rangle$ to the state $|a\rangle$;
- The atom remains in the state $|a\rangle$ during the laser interaction;
- The atom remains in the state $|b\rangle$ during the laser interaction.

These four processes determine the accumulated phase associated with each interaction with the laser pulses. The accumulated phase resulting from the pulses can be calculated from the transition operators U_{ij} associated with each Raman pulse according Table 3.1.

Given the information contained in Table 3.1, the final amplitudes and phase for the upper arm are:

$$U_{aa}U_{bb}\,e^{+i[k_{\text{eff}}z_C - \phi_2]},$$

while for the lower arm we obtain

$$U_{bb}\,U_{aa}\,e^{+i(k_{\text{eff}}(z_A - z_D + z_B) - \phi_1 + \phi_2 - \phi_3)}.$$

Table 3.1: Amplitude and phase associated with each transition.

Time	**Pulse**	**Upper arm**	**Lower arm**
$t = 0$	$\pi/2$	U_{aa}	$U_{ba}e^{+i(k_{\rm eff}z_A-\phi_1)}$
$t = T$	π	$U_{ba}e^{+i(k_{\rm eff}z_C-\phi_2)}$	$U_{ab}e^{-i(k_{\rm eff}z_D-\phi_2)}$
$t = 2T$	$\pi/2$	U_{bb}	$U_{ba}e^{+i(k_{\rm eff}z_B-\phi_3)}$

The difference between the accumulated phases in the two arms results therefore in:

$$\begin{aligned}\Delta\phi_{tot} &= k_{\rm eff}\,(z_C - z_B) + \omega_L T - \phi_2 + \phi_3 - [k_{\rm eff}\,(z_A - z_D) + \omega_L T - \phi_1 + \phi_2] = \\ &= k_{\rm eff}\,(z_C - z_B - z_A + z_D) + \phi_1 - 2\phi_2 + \phi_3,\end{aligned}$$

where the presence of $k_{\rm eff}$ follow from the phases in the operators U's written in Table 3.1.

Using Eq. (3.66), we arrived at the main result of primary interest for gravity measurements: The total accumulated phase can be expressed as

$$\Delta\phi_{tot} = k_{\rm eff} g T^2 + \phi_1 - 2\phi_2 + \phi_3. \tag{3.67}$$

In other words, $\Delta\phi_{\rm grav}$, as defined in (3.63) with $\Delta\phi_{\rm laser}$ given by Eq. (3.62), is given by $\Delta\phi_{\rm grav} = k_{\rm eff} g T^2$.

The effect of gravitational acceleration acts continuously along the entire atomic trajectory, such that the term $k_{\rm eff} g T^2$ represents the total phase accumulated at $t = 2T$. However, gravitational acceleration also shifts the atomic resonance frequency; i.e., an atom that is initially in resonance with the first $\pi/2$ pulse will no longer remain resonant with the subsequent pulses if the laser frequencies are kept fixed.

To compensate for this effect, a linear chirp may be applied to the Raman frequency difference (Young et al., 1997). Consequently, the time-dependent phase, which we denote by $\Phi(t)$, evaluated at each pulse is given by

$$\Phi_1(t_1) = \omega_1 t_1 - k_{\rm eff} g\, t_1^2 + \phi_1, \tag{3.68}$$
$$\Phi_2(t_2) = (\omega_1 + \omega_m) t_2 - k_{\rm eff} g\, t_2^2 + \phi_2, \tag{3.69}$$
$$\Phi_3(t_3) = (\omega_1 + 2\omega_m) t_3 - k_{\rm eff} g\, t_3^2 + \phi_3. \tag{3.70}$$

Substituting $t_1 = 0$, $t_2 = T$, and $t_3 = 2T$, one obtains

$$\begin{aligned}\Delta\Phi &= \Phi_1(0) - 2\Phi_2(T) + \Phi_3(2T) \\ &= 2\,\omega_m T - k_{\rm eff}\, g\, T^2 + \Delta\phi_{\rm laser},\end{aligned} \tag{3.71}$$

where ω_m is a frequency to be determined.

Resonance can be maintained by applying a single continuous chirp to the Raman frequency difference: one obtains

$$\Delta\Phi = (\beta - k_{\text{eff}} g)T^2, \tag{3.72}$$

where $\beta = \omega_m/T$. When the rate of variation of the Raman frequency (chirp) satisfies the condition

$$\beta = k_{\text{eff}}\, g,$$

the total interferometric phase becomes zero, that is, $\Delta\Phi = 0$. In this situation, the Doppler shift associated with the gravitational acceleration of the atoms is completely compensated by the chirp applied to the Raman beams. Thus, the phase cancellation condition can be written as

$$\beta - k_{\text{eff}}\, g = 0, \tag{3.73}$$

from which one directly obtains (Ménoret et al., 2018)

$$g = \frac{\beta}{k_{\text{eff}}}. \tag{3.74}$$

The experimental parameters τ, T, and $\Delta\phi_0$ are controlled and therefore known. With these values fixed, the total phase accumulated over the three-pulse Raman interferometric sequence can be inferred from the transition probability to the excited state, as described by Eqs. (3.29) and (3.61). Experimentally, this probability is determined by the ratio between the number of atoms detected in the excited state and the total number of atoms after the application of the three laser pulses. Therefore, by varying the frequency chirp β, the interferometric phase is modified and, consequently, the final population in the excited state is changed. In this manner, the phase associated with the interference can be continuously tuned through the control of β. The value of the local gravitational acceleration g is then determined by identifying the value of β that cancels the interferometric phase and by applying the relation given in Eq. (3.74).

3.4 Analysis of the Quantum Gravimeter Stability

The precision and stability of quantum gravimeters rely on the ability to characterize the various noise sources that affect the phase measurement, as the signals obtained from these instruments often exhibit non-Gaussian and non-stationary noise. As seen in the previous sections, the output of an atomic interferometer is a phase

accumulated by the atoms (sensitive to local gravity), but also to various sources of noise, among which the laser noise and phase fluctuations caused by mechanical vibrations of the experimental platform (Le Gouët et al., 2008).

In this context, the Allan deviation (Allan, 1966; Riley and Howe, 2008) arises as a tool to quantify the stability of signals over different time scales. Additionally, a complementary description can be obtained in the frequency domain, where the phase variance is calculated from the power spectral density (PSD).

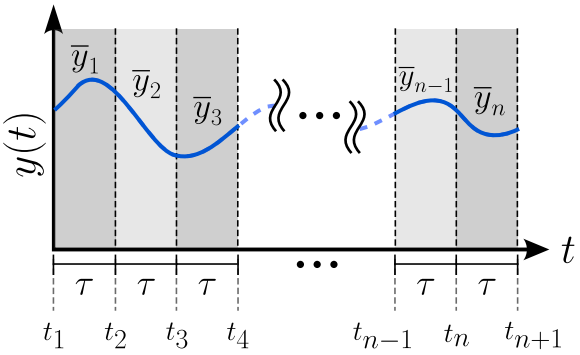

Figure 3.8: Illustration of the sampling of the data $y(t)$ into n intervals of duration τ, where, for each interval, the mean of the values contained within it is calculated. That is, for the i-th interval, the mean $\bar{y}_i$ of all the y samples within that interval is computed.

The computation of the Allan deviation for a time series $y(t)$ is based on the statistical comparison of successive averages of the signal over windows of duration τ. For a given value of τ, the total observation interval is partitioned into n adjacent blocks, each covering the interval $[t_i,\, t_{i+1}]$(Rubiola, 2008), as shown in Figure 3.8. The average of the signal in each block is then defined as

$$\bar{y}_i(\tau) = \frac{1}{\tau} \int_{t_i}^{t_{i+1}} y(t)\, dt \tag{3.75}$$

where $i = 1, 2, 3, \ldots, n$. The corresponding Allan variance is given by

$$\sigma_y^2(\tau) = \frac{1}{2(n-1)} \sum_{i=1}^{n} \left[\bar{y}_{i+1}(\tau) - \bar{y}_i(\tau)\right]^2, \tag{3.76}$$

and the Allan deviation is simply $\sigma_y = \sqrt{\sigma_y^2}$.

In practice, $y(t)$ is not continuous but sampled, such that each interval τ contains m samples. Therefore, the average over the i-th window is given by

$$\bar{y}_i = \frac{1}{m}\sum_{k=1}^{m} y_k,$$

where the index k runs over all samples contained within the i-th window.

Since the phase accumulated by the system does not exhibit a uniform response to temporal perturbations, the interferometer displays a dynamics that depends on the instant at which such perturbations are applied. This behavior is formally described by the sensitivity function, which establishes the connection between phase fluctuations, acceleration noise, and the experimentally observed phase variance, thereby constituting the fundamental link with the Allan deviation.

To make this relationship explicit, the following sections introduce the formalism of the interferometer sensitivity function, derived from the evolution of the atomic state during the pulse sequence. Subsequently, the Allan variance is expressed in terms of the noise power spectral density and the transfer function associated with the interferometer.

3.4.1 Sensitivity to Phase Variations

The final phase Φ measured in an interferometer is not acquired instantaneously, but accumulated throughout the operation of the instrument. Thus, any temporal fluctuation $\delta\phi(t)$ in the phase affects the final measured value. However, the interferometer does not respond uniformly to disturbances applied at different moments. The sensitivity to these fluctuations depends on the time at which they occur, and this temporal dependence is described by the sensitivity function $g_s(t)$.

Consider an infinitesimal perturbation $\delta\phi(t)$ applied to the phase of the Raman lasers at time t. This perturbation generates a corresponding variation δP in the transition probability P (given by Eqs. (3.29) and (3.61)). The sensitivity function is defined as the limit of the ratio between these two quantities (Le Gouët et al., 2008; Cheinet et al., 2008; Tinsley, 2019):

$$g_s = 2\lim_{\delta\phi\to 0}\frac{\delta P}{\delta\phi}. \tag{3.77}$$

In order to determine the explicit temporal dependence of $g_s(t)$, it is necessary to analyze how an infinitesimal phase jump, applied at an arbitrary instant during the interferometric sequence, propagates through the coherent evolution of the atomic

system. The dynamics of the probability amplitudes can be expressed in matrix form based on the solutions of the system of equations (3.50) and (3.51):

$$\begin{pmatrix} C_b(t_0+\tau) \\ \\ C_a(t_0+\tau) \end{pmatrix} = M(t_0,\phi,\Omega_R,\tau) \begin{pmatrix} C_b(t_0) \\ \\ C_a(t_0) \end{pmatrix}, \tag{3.78}$$

where $M(t_0,\phi,\Omega_R,\tau)$ is the transfer matrix given by (Cheinet et al., 2008)

$$M(t_0,\phi,\Omega_R,\tau) = \begin{pmatrix} \cos\left(\frac{\Omega_R\tau}{2}\right) e^{-i\omega_b\tau} & -ie^{-i[(\omega_1-\omega_2)t_0+\phi]} \sin\left(\frac{\Omega_R\tau}{2}\right) e^{-i\omega_b\tau} \\ \\ -ie^{i[(\omega_1-\omega_2)t_0+\phi]} \sin\left(\frac{\Omega_R\tau}{2}\right) e^{-i\omega_a\tau} & \cos\left(\frac{\Omega_R\tau}{2}\right) e^{-i\omega_a\tau} \end{pmatrix} \tag{3.79}$$

.

The quantum state at the output of the interferometer is obtained by sequentially applying the evolution operators associated with each stage of the interferometric sequence. These stages consist of three Raman pulses interleaved with two free-evolution intervals of duration T. The total evolution operator is therefore constructed as the ordered product of five transfer matrices, each describing either a laser interaction or a free propagation period. Assuming that phase fluctuations during the finite pulse durations can be neglected, the Raman phases are defined at the central times of the three pulses and denoted by ϕ_1, ϕ_2, and ϕ_3. For convenience, the time origin is chosen at the midpoint of the central π-pulse. With this convention, the complete evolution operator of the interferometer can be written as

$$M_{\text{interf}} = M(T+\tau,\phi_3,\Omega_{\text{R}},\tau)\, M(T)\, M(-\tau,\phi_2,\Omega_{\text{R}},2\tau)\, M(T)\, M(-T-2\tau,\phi_1,\Omega_{\text{R}},\tau).$$

$M(T)$ corresponds to the transfer matrix associated with the free evolution intervals. It is obtained from the previous matrix in the limit where the effective coupling tends to zero, that is, by taking $\Omega_R \to 0$. In this case, the coupling terms vanish and the matrix reduces to a diagonal form given by

$$M(T) = \begin{pmatrix} e^{-i\omega_b T} & 0 \\ 0 & e^{-i\omega_a T} \end{pmatrix}.$$

The final state amplitudes are obtained by applying the total evolution matrix to this initial condition. The probability of finding the atom in state $|b\rangle$ at the output is then determined from the squared modulus of the corresponding amplitude, yielding

$$P = |C_e(T+2\tau)|^2 = \frac{1-\cos(\phi_1-2\phi_2+\phi_3)}{2}.$$

This expression is consistent with the results obtained for the two-level and three-level systems presented in the initial sections of this chapter (Eqs. (3.29) and (3.61)).

For maximum sensitivity, the interferometer is assumed to operate at the point of maximum fringe slope, i.e., under the condition in which the total phase is $\Phi = \pi/2$ (Cheinet et al., 2008; Tinsley, 2019). In this regime, the transition probability is $P = 1/2$, and small phase perturbations generate linear and symmetric variations around the operating point. The transition probability may be written as

$$P = \frac{1}{2}\left[1 - \cos\left(\frac{\pi}{2} \pm \delta\Phi(t)\right)\right]. \tag{3.80}$$

Using $\cos\left(\frac{\pi}{2} \pm \delta\Phi\right) = \mp \sin\left(\delta\Phi\right)$ and $\sin\delta\Phi \approx \delta\Phi$, we obtain $P \approx \frac{1\mp\delta\Phi(t)}{2}$, from which $\delta P = \frac{\delta\Phi(t)}{2}$ and, $g_s = \lim_{\delta\phi\to 0}\frac{\delta\Phi(t)}{\delta\phi}$. Following Cheinet et al. (2008), to which we refer for more details, one finds that g_s is given by

$$g_s(t) = \begin{cases} \sin(\Omega_R t), & 0 < t < T/2 \\ 1, & T/2 < t < T + T/2 \\ \sin(\Omega_R(t-T)), & T + T/2 < t < T + T \end{cases} \tag{3.81}$$

.

A noise component $\delta\phi$ applied between the first and the second pulses induces a variation $\delta\Phi = -\delta\phi$ in the accumulated phase Φ, resulting in $\delta P \simeq -\delta\phi/2$. Consequently, the sensitivity function assumes the value -1 within this temporal interval, while between the second and the third pulses it assumes the value $+1$ (Cheinet et al., 2008), as shown in Figure 3.9.

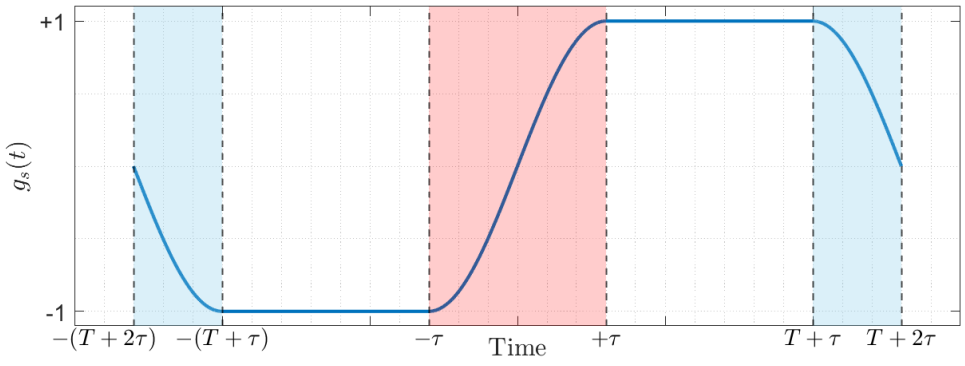

Figure 3.9: Sensitivity function: The regions shaded in blue represent the intervals during the operation of the $\pi/2$ pulses, while the red region corresponds to the interval during the operation of the π pulse.

The sensitivity function establishes a direct relationship between the temporal phase fluctuations and the total phase accumulated in the interferometer. Thus, any noise source affecting the phase, whether originating from the laser, mechanical vibrations of the experimental platform, or other sources, can be incorporated into the sensitivity function to estimate its impact on the gravity measurement.

In the frequency domain, the sensitivity function also allows calculating the contribution of noise to the instability of the accumulated phase using the noise power spectral density $S(\omega)$, with the Allan variance of the accumulated phase being expressed as (Le Gouët et al., 2008):

$$\sigma_\Phi^2 = \int_0^\infty \Big[\omega |G(\omega)|\Big]^2 S_\phi(\omega)\, d\omega, \tag{3.82}$$

where $G(\omega)$ is the Fourier transform of the sensitivity function $g_s(t)$. In addition, σ_Φ^2 can also be described in the frequency domain as (Peters et al., 2001; Rubiola, 2008):

$$\sigma_\Phi^2 = \int_0^\infty |H(\omega)|^2 S_\Phi(\omega)\, d\omega, \tag{3.83}$$

where $H(\omega)$ is the frequency-dependent transfer function of the interferometer. This formulation provides a powerful framework for quantifying the influence of different noise components – white noise, phase noise, mechanical vibrations, among others.

3.4.2 Noise Contributions to the Quantum Gravimeter Sensitivity

The sensitivity of a quantum gravimeter is affected by any noise source capable of generating perturbations in the measured interferometric phase. Temporal phase fluctuations couple to the total accumulated phase through the sensitivity function, resulting in a phase variance that degrades the precision of the gravity measurement. This formalism provides a unified framework to describe the influence of different noise sources, both internal and external to the interferometric system.

A particularly relevant example is the noise arising from mechanical vibrations of the platform on which the gravimeter is installed. When the platform vibrates, the freely falling atoms do not follow this motion. However, when adopting the reference frame defined by the interferometer structure – in particular, the retroreflection mirror of the Raman beams – such vibrations are equivalent to an acceleration imposed on the atoms. Consequently, this relative motion between the atoms and the interferometer reference frame manifests itself as an effective acceleration fluctuation, which couples directly to the measured interferometric phase (Miffre et al., 2006).

As described in Cheinet et al. (2008), this effect can be modeled by introducing a spurious acceleration $\delta a(t)$, which couples to the interferometric phase through the effective wave vector k_{eff}. The corresponding variation of the accumulated phase can then be written as

$$\delta\Phi = k_{\text{eff}} \int g_a(t)\, \delta a(t)\, dt, \tag{3.84}$$

where $g_a(t)$ is the interferometer sensitivity function to accelerations. This function is directly related to the phase sensitivity function $g_s(t)$ through the relation

$$g_a(t) = \frac{1}{k_{\text{eff}}} \frac{d^2 g_s(t)}{dt^2}. \tag{3.85}$$

In the frequency domain, this relation allows the Allan variance associated with vibration noise to be expressed in terms of the power spectral density of the acceleration noise $S_a(\omega)$. For an integration time τ, the resulting Allan variance can be written as (Le Gouët et al., 2008; Cheinet et al., 2008)

$$\sigma_a^2(\tau) = \frac{k_{\text{eff}}^2}{\tau_m} \int_0^\infty \left| \frac{G(\omega)}{\omega^2} \right|^2 S_a(\omega)\, d\omega, \tag{3.86}$$

where the factor $1/\omega^2$ strongly suppresses the contribution of high-frequency vibrations. As a consequence, low-frequency components of $S_a(\omega)$ dominate the measurement variance, while high-frequency vibrations have a significantly reduced impact on the estimation of the gravitational acceleration.

3.5 Conclusion

In this work, we present a pedagogical description of the operating principle of ultracold quantum gravimeters, with the objective of providing content specifically directed to geoscientists. We start with a brief presentation of the fundamental concepts of quantum mechanics, such as the superposition principle, the bra–ket notation, and the time evolution described by the Schrödinger equation. These constitute the basis for the modeling of two- and three-level atomic systems interacting with laser fields.

In addition, we discuss how laser pulses can play roles analogous to splitters and mirrors for electromagnetic waves, culminating in the realization of a Mach–Zehnder–type atomic interferometer. In this context, we elucidate how the phase accumulated along the different arms of the interferometer is directly related to the gravitational

acceleration and how this information can be experimentally retrieved from the final populations of the atomic states after the interferometric pulse sequence.

A central point of the analysis lies in the fact that for the three-level Raman scheme employed in quantum gravimeters the final expression for the transition probability exhibits the same functional form as that obtained in an effective two-level model. This equivalence highlights the robustness of the underlying interferometric principle and justifies the recurrent use of simplified two-level descriptions in theoretical studies and practical applications.

We further discuss how gravity contributes to the interferometric phase through the classical action associated with the atomic trajectories and how the introduction of a frequency chirp in the Raman lasers allows compensation of the Doppler shift induced by gravitational acceleration. This procedure leads to the phase dependence proportional to $k_{\text{eff}} g T^2$ which constitutes the basis of absolute gravity measurements performed with atomic interferometers.

Additionally, we analyze the stability of the quantum gravimeter using the Allan variance, emphasizing its role as a statistical tool for characterizing the instrument performance over different time scales. Both time-domain and frequency-domain formulations are presented. We show how the interferometer sensitivity function acts as the link between temporal phase fluctuations and the variance of the accumulated phase, enabling a quantitative assessment of the contribution of different noise sources, with particular emphasis on mechanical vibration noise.

By presenting the theoretical foundations in a detailed manner, we intend to make this work an useful reference for geoscientists interested in understanding, employing, or improving quantum gravimeters. As quantum sensors become increasingly commercially accessible, their impact on field measurements, long-term monitoring, and gravimetric applications is expected to expand. In this context, knowledge of the underlying quantum principles becomes an increasingly indispensable competence.

Accordingly, we view this contribution as an invitation to the geoscience community for deeper engagement with measurement techniques based on quantum physics, fostering interdisciplinary research at the interface between fundamental physics and the Earth sciences.

Chapter 4

Geophysical Applications

4.1 Introduction

Geophysics constitutes a branch of the geosciences dedicated to the study of the structure, composition, and physical processes that govern the Earth's interior. It is characterized by the application of physical principles to investigate subsurface properties in an indirect manner, providing essential information for the understanding of terrestrial dynamics and supporting a wide range of applications, such as the exploration of natural resources, including iron, gold, petroleum, natural gas, among others.

In general, geophysics is subdivided into different methods, which are classified according to the type of physical property investigated (Telford et al., 1990). Among the main geophysical methods, the gravimetric, magnetic, seismic, and electromagnetic methods stand out. Each of these methods evaluates distinct physical properties, such as density, magnetic susceptibility, elastic wave propagation velocity, and electrical conductivity, respectively. The selection of the most appropriate method depends on the objective of the study, the scale of investigation, and the geological characteristics of the area of interest.

The relationship between gravimetric anomalies and geology is associated with variations in the density of subsurface rocks. Different lithologies present distinct average densities, as illustrated in Figure 4.1. For example, sedimentary rocks generally exhibit lower densities when compared to igneous and metamorphic rocks. Lithological variations generate density contrasts, which are associated with variations in the gravitational field. Such variations constitute the physical basis for the interpretation of gravimetric anomalies.

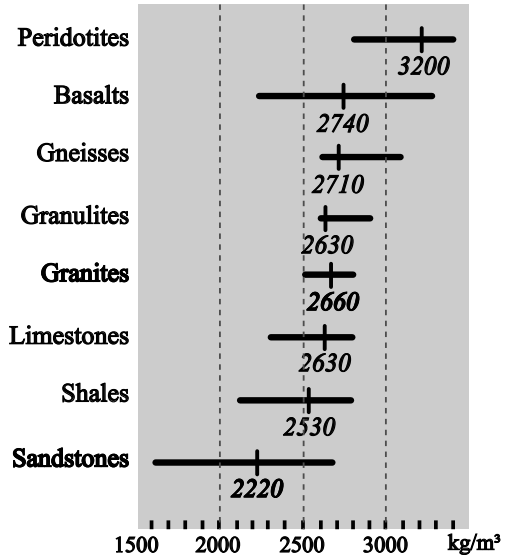

Figure 4.1: Average density of rocks associated with different lithological types (From Teixeira et al. (2009)).

4.2 Forward gravimetric modeling

The quantitative interpretation of gravimetric data requires the establishment of mathematical models capable of relating the subsurface density distribution to the anomalies observed in the gravitational field. This process, known as gravimetric modeling, can be conducted in both the forward and inverse senses. In the forward problem, a known geometry and density distribution are assumed, and the corresponding gravimetric response is calculated. In contrast, the inverse problem seeks to estimate the density distribution from the measured anomalies.

One of the most widely used models in applied gravimetry is the representation of the subsurface by means of rectangular prisms with constant density (Tan et al., 2021). This approach presents computational advantages, since it allows complex geometries to be approximated through the discretization of the volume of interest into regular prismatic elements (Blakely, 1995). In addition, the gravimetric response of a rectangular prism can be calculated analytically (Nagy et al., 2000).

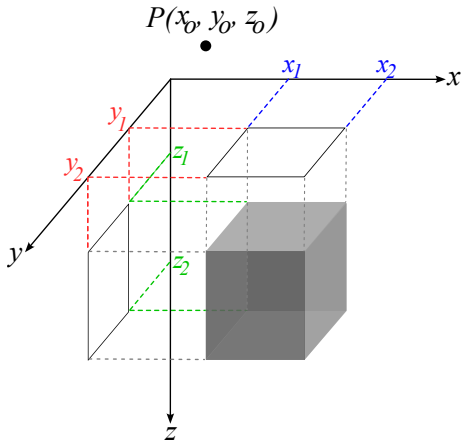

Figure 4.2: Geometry of a rectangular prism with which the subsurface is discretized. The gravity value is calculated in point P (modified from Nagy et al. (2000)).

Figure 4.2 illustrates the geometry of a rectangular prism, defined by its boundaries along the x, y, and z directions, and by an observation point located at (x_o, y_o, z_o). The vertical component of gravitational acceleration, g_z, generated by a homogeneous prism of density ρ, can be expressed, according to (Nagy et al., 2000), by the following equation:

$$g_z = \gamma\,\rho \sum_{i=1}^{2}\sum_{j=1}^{2}\sum_{k=1}^{2} \mu_{ijk}\left[Z_k \arctan\left(\frac{X_i\,Y_j}{Z_k\,R_{ijk}}\right) - X_i \ln\left(R_{ijk}+Y_j\right) - Y_j \ln\left(R_{ijk}+X_i\right)\right], \tag{4.1}$$

where

$$\mu_{ijk} = (-1)^i(-1)^j(-1)^k. \tag{4.2}$$

The geometric variables are given by

$$X_i = x_i - x_o, \quad Y_j = y_j - y_o, \quad Z_k = z_k - z_o, \tag{4.3}$$

and R_{ijk} is defined as

$$R_{ijk} = \sqrt{X_i^2 + Y_j^2 + Z_k^2}. \tag{4.4}$$

Equation (4.1) provides an exact solution for calculating the vertical component of the gravitational field generated by a homogeneous rectangular prism. In practical applications, more complex gravimetric models are constructed through the linear superposition of the contributions from multiple prisms.

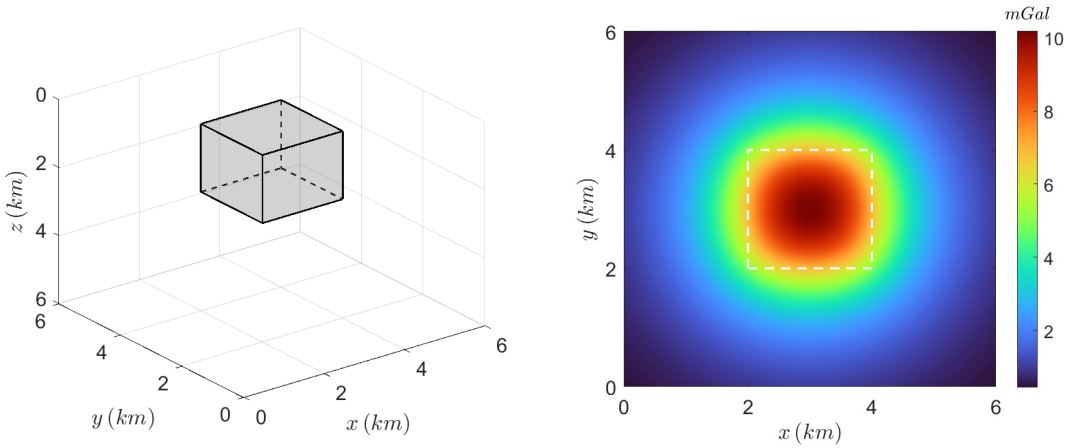

Figure 4.3: (a) Cube with a 2 km edge length, density of 440 kg/m^3, and top located at a depth of 500 m. (b) Gravimetric anomaly generated by this cube at height z=0.

For example, suppose a cube with a density of 440 $\mathrm{kg/m^3}$, located at a depth of 500 m. The solution provided by Nagy et al. (2000) allows the calculation of the vertical component of the gravitational field (g_z) at an observation point. This enables the determination of the gravimetric anomaly generated by the cube, which is useful for modeling and interpreting gravimetric data.

4.3 Gravimeter sensitivity and the geophysical information contained in the measured signal.

As discussed previously, the sensitivity of the quantum gravimeter considered in this study is approximately 1 μGal (Exail, 2023), which is superior to that of most classical gravimeters, such as the Scintrex CG-6, whose sensitivity is about 5 μGal (Scintrex, 2019). Moreover the quantum gravimeter measures the absolute value of acceleration and is not limited to its relative variation with respect to reference point in which the value of acceleration g is known.

Consider the cube illustrated in Figure 4.3(a), the maximum amplitude of the anomaly is located directly above the geometric center of the prism, at the surface point $(3, 3, 0)$. If the depth of the prism is increased while keeping its geometry and density contrast constant, the amplitude of the resulting gravimetric anomaly decreases. This attenuation reflects the well-known decay of the gravitational field

with distance from the source. The evolution of the maximum anomaly amplitude at $(3, 3, 0)$ as a function of the prism depth is shown in Figure 4.4 (black curve).

For this specific model, when the prism reaches a depth of approximately 67.45 km, the value of the vertical gravity component g_z at the surface point $(3, 3, 0)$ decreases to $5\,\mu Gal$. This value corresponds to the nominal sensitivity of the Scintrex CG-6 gravimeter and therefore defines, for this configuration, its practical limit of detectability. At greater depths, the gravitational signal produced by the prism falls below the instrumental sensitivity and becomes indistinguishable from measurement noise. In other words, for depths exceeding this threshold, the Scintrex CG-6 would no longer be capable of resolving the presence of the subsurface body.

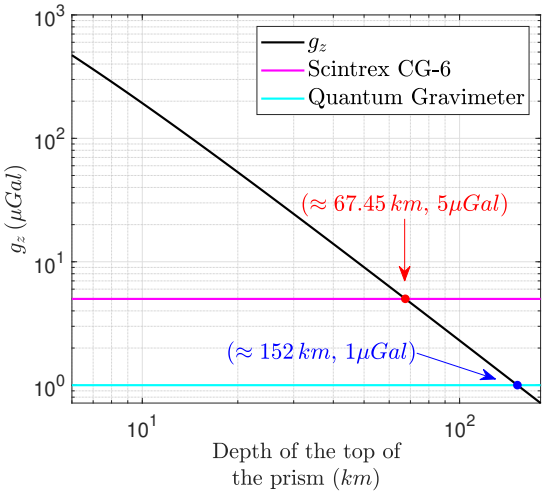

Figure 4.4: Gravitational signal g_z as a function of depth of the top of a subsurface prism. The black curve represents the theoretical vertical gravity component generated by the prism, showing the attenuation of the signal with increasing depth. The horizontal magenta line indicates the sensitivity limit of a Scintrex CG-6 gravimeter $\sim 5\,\mu$Gal), while the cyan line corresponds to the sensitivity of a quantum gravimeter ($\sim 1\,\mu$Gal). The highlighted points mark the maximum detectable depths for each instrument, approximately 67.45 km for the CG-6 and 152 km for the quantum gravimeter.

An analogous analysis can be performed for the quantum gravimeter. Owing to its higher sensitivity of approximately $1\,\mu Gal$, the corresponding detectability limit for the same prism occurs at a significantly greater depth, estimated to be on the order of $152\,km$. This simple comparison highlights how improvements in instrumental

sensitivity translate directly into an enhanced ability to detect small variations in the gravitational field. However, it is important to emphasize that the instrumental sensitivity values considered correspond to ideal operating conditions, typically associated with controlled environments and low levels of external disturbances. In real-world applications, the gravimetric signal is often contaminated by various noise sources, such as seismic vibrations and instrumental noise, which significantly degrade the signal-to-noise ratio and, consequently, reduce the effective detectability of the instruments.

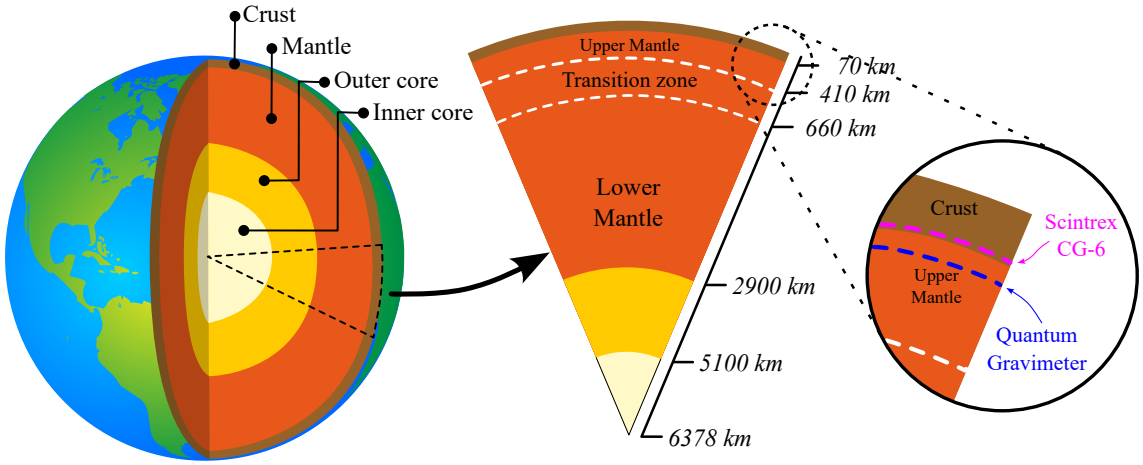

Figure 4.5: Slice through the Earth with the principal compositional shells it is divided into. The zoom sets the depth-context of the sensitivity to the 2 km sized cube mentioned above.

This experiment also demonstrates that the measured gravity variations are directly associated with subsurface density contrasts, which in many cases reflect lithological variations. Therefore, it can be stated that the gravimetric signal contains relevant information about the geological structure of the investigated region, although this relationship is indirect and subject to geophysical ambiguities.

Mathematically, the relationship between the subsurface density distribution, represented by the parameter vector $\mathbf{p}$, and the observed gravity values, $\mathbf{g}_{\text{obs}}$, can be expressed by the linear system

$$\mathbf{A}\mathbf{p} = \mathbf{g}_{\text{obs}}, \tag{4.5}$$

where $\mathbf{A}$ is the sensitivity matrix (or kernel matrix), which describes the response of the gravitational field to density variations in the model. Each element of the matrix

$\mathbf{A}$ is defined as

$$A_{ij} = \frac{\partial g_{z,i}}{\partial \rho_j}, \tag{4.6}$$

representing the contribution of the density variation of element j to the gravitational observation i.

Under the assumption of a linear and well-conditioned problem, the density parameters can be estimated using a least-squares solution, yielding

$$\mathbf{p} = \left(\mathbf{A}^T\mathbf{A}\right)^{-1}\mathbf{A}^T\mathbf{g}_{\text{obs}}. \tag{4.7}$$

In practice, however, this system is often ill-posed or ill-conditioned, making regularization techniques necessary to obtain stable and physically plausible solutions.

4.3.1 Density estimation: Tikhonov regularization

In gravimetric inversion, the estimation of the subsurface density distribution is typically affected by ill-posedness and ill-conditioning, which may lead to unstable or non-unique solutions. To obtain a stable and physically meaningful estimate of the parameter vector $\mathbf{p}$, the inverse problem is formulated as a Tikhonov-regularized least-squares minimization problem:

$$\min_{\mathbf{p}} \left(|\mathbf{A}\mathbf{p} - \mathbf{g}_{\text{obs}}|^2 + \lambda\, \mathbf{p}^T\Theta\mathbf{p} \right). \tag{4.8}$$

The first term of the objective function quantifies the data misfit, ensuring consistency between the predicted and observed gravity data, while the second term introduces a stabilizing constraint through the regularization matrix Θ. This matrix is commonly chosen to impose smoothness or other a priori structural assumptions on the model. The scalar parameter λ controls the trade-off between data fitting and model regularity.

By expanding the objective function, taking the gradient with respect to $\mathbf{p}$, and setting it equal to zero, the following system of normal equations is obtained:

$$\mathbf{A}^T\mathbf{A}\,\mathbf{p} + \lambda\,\Theta\,\mathbf{p} = \mathbf{A}^T\mathbf{g}_{\text{obs}}. \tag{4.9}$$

The corresponding regularized solution can therefore be written in closed form as

$$\mathbf{p}_{\text{est}} = \left(\mathbf{A}^T\mathbf{A} + \lambda\Theta\right)^{-1}\mathbf{A}^T\mathbf{g}\text{obs} \tag{4.10}$$

This formulation highlights the role of Tikhonov regularization in stabilizing the inversion by mitigating the amplification of noise associated with small singular values of the sensitivity matrix.

Global Smoothness Constraint

In certain geophysical inversion problems, it may be physically reasonable to assume that the properties of the medium vary smoothly and continuously in space, based on geological information. The global smoothness constraint is introduced precisely to incorporate this *a priori* information into the inverse problem.

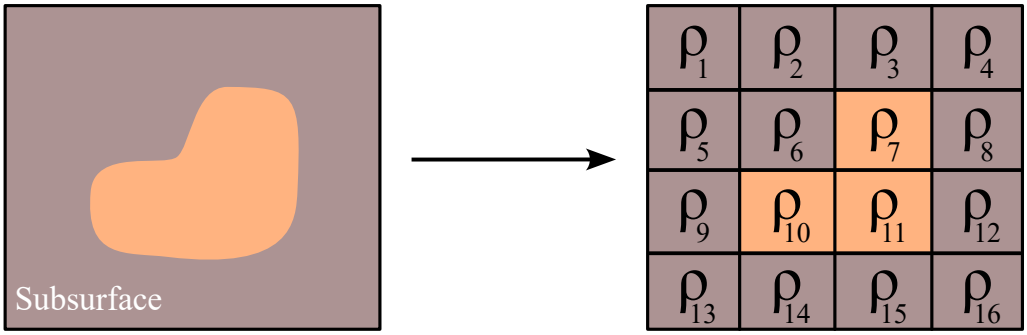

Figure 4.6: Two-dimensional model discretized with 16 parameters. On the left, representation of the surface of the geophysical model. On the right, discretization of the subsurface into rectangular cells, associated with the parameters used in the inversion process.

The first step of the inversion process consists of discretizing the domain of interest. Considering the discretized two-dimensional model presented in Figure 4.6, in which the subsurface is subdivided into cells or parameters, the smoothness functional is defined as

$$\Theta = \mathbf{R}^T\mathbf{R}.$$

The matrix $\mathbf{R}$ is characterized by rows that contain exactly two nonzero entries, 1 and -1, whose column positions correspond to pairs of spatially adjacent parameters. In this way, the matrix $\mathbf{R}$ represents the discrete first-derivative operator, constructed using finite differences and acting along the horizontal and vertical directions of the two-dimensional model (Tikhonov and Arsenin, 1977; Barbosa et al., 1999).

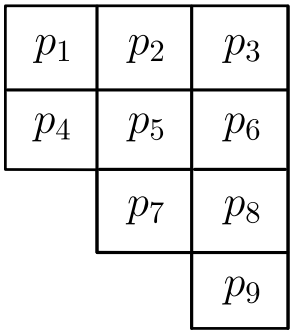

Figure 4.7: Two-dimensional grid composed of nine parameters p_i, illustrating their spatial arrangement and adjacency relationships. The corresponding matrix $\mathbf{R}$, defined in equation 4.11, encodes the connectivity between neighboring parameters.

For example, given the two-dimensional grid illustrated in Figure 4.7, the corresponding matrix $\mathbf{R}$ associated with this grid is given by

$$\mathbf{R} = \begin{bmatrix} 1 & -1 & 0 & 0 & 0 & 0 & 0 & 0 & 0 \\ 0 & 1 & -1 & 0 & 0 & 0 & 0 & 0 & 0 \\ 0 & 0 & 0 & 1 & -1 & 0 & 0 & 0 & 0 \\ 0 & 0 & 0 & 0 & 1 & -1 & 0 & 0 & 0 \\ 0 & 0 & 0 & 0 & 0 & 0 & 1 & -1 & 0 \\ 1 & 0 & 0 & -1 & 0 & 0 & 0 & 0 & 0 \\ 0 & 1 & 0 & 0 & -1 & 0 & 0 & 0 & 0 \\ 0 & 0 & 1 & 0 & 0 & -1 & 0 & 0 & 0 \\ 0 & 0 & 0 & 0 & 1 & 0 & -1 & 0 & 0 \\ 0 & 0 & 0 & 0 & 0 & 1 & 0 & -1 & 0 \\ 0 & 0 & 0 & 0 & 0 & 0 & 0 & 1 & -1 \end{bmatrix} \tag{4.11}$$

Note that each row of this matrix contains exactly two nonzero entries, equal to $+1$ and -1. The columns in which these entries appear correspond to the indices of the neighboring parameters that share the edge associated with the respective row.

Therefore, in the example considered, the first row is associated with edge 1 (highlighted in blue in Figure 4.8). In this row, the values $+1$ and -1 appear in columns 1 and 2, respectively, indicating that the parameters p_1 and p_2 share this edge. Similarly, row 11 is associated with edge 11 (highlighted in green in Figure 4.8). The values $+1$ and -1 appear in columns 6 and 8, respectively, indicating that the parameters p_6 and p_8 are adjacent along this edge.

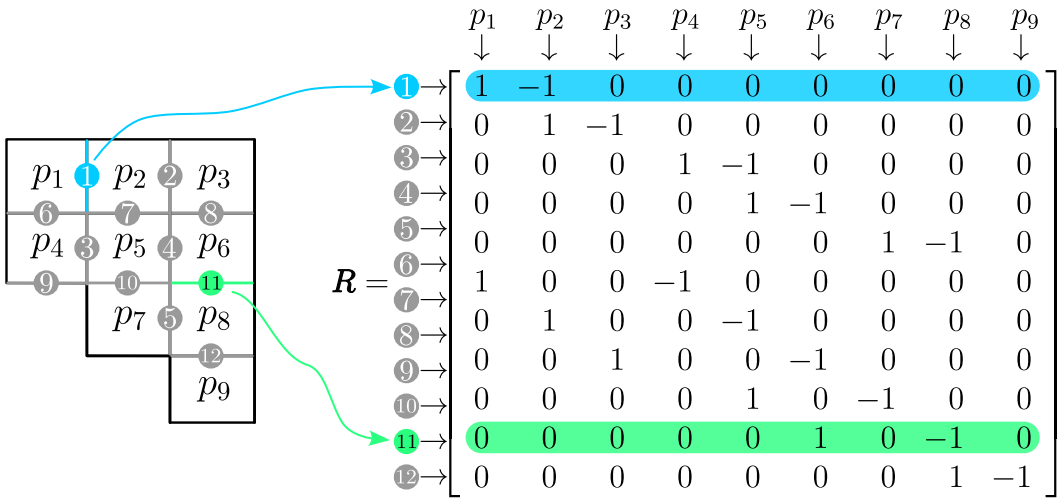

Figure 4.8: Schematic illustration of the structure of matrix $\mathbf{R}$. Each column corresponds to a specific parameter, while each row represents an edge shared by two neighboring parameters.

In the horizontal direction the smoothness operator imposes proximity relationships between parameters located side by side within the same row, such as $p_1 \approx p_2$, $p_2 \approx p_3$, $p_4 \approx p_5$, $p_5 \approx p_6$ and $p_7 \approx p_8$, for the example illustrated in Figure 4.7. In the vertical direction, the constraint enforces smoothness between parameters associated with vertically adjacent cells in consecutive rows of the mesh, resulting in relationships such as $p_1 \approx p_4$, $p_2 \approx p_5$, $p_3 \approx p_6$, $p_5 \approx p_7$; $p_6 \approx p_8$ and $p_8 \approx p_9$.

From a physical standpoint, the application of the operator $\mathbf{R}$ to the parameter vector results in a vector containing the local variations between neighboring cells. The minimization of the functional Θ penalizes abrupt variations in these differences, promoting spatially smooth and more stable solutions. Consequently, the global smoothness regularizer enforces similarity between parameters associated with adjacent cells. In particular, differences between neighboring parameters in the horizontal and vertical directions of the mesh are penalized.

4.3.2 Density estimation: generalized inverse method

Another approach employed for parameter estimation is the generalized inverse method, which is based on the Singular Value Decomposition (SVD). This technique constitutes a robust tool of linear algebra that enables the efficient analysis and manipulation of matrices.

For the application of this method, it is assumed that the sensitivity matrix $\mathbf{A}$ can be decomposed as follows:

$$\mathbf{A} = \mathbf{U}\,\mathbf{S}\,\mathbf{V}^T,$$

where $\mathbf{U}$ is an orthogonal matrix of dimension $m \times m$, whose columns correspond to the left singular vectors of $\mathbf{A}$; $\mathbf{V}$ is an orthogonal matrix of dimension $n \times n$, whose columns represent the right singular vectors; and $\mathbf{S}$ is a diagonal matrix of dimension $m \times n$, which contains the singular values of $\mathbf{A}$, arranged in decreasing order along the main diagonal.

From the singular value decomposition, the estimation of the model parameters can be obtained through the generalized inverse of the sensitivity matrix, also known as the Moore–Penrose pseudoinverse, here denoted by $\mathbf{A}^+$ (Wang et al., 2018). This inverse is constructed from the SVD of the matrix $\mathbf{A}$ and is expressed as

$$\mathbf{A}^+ = \mathbf{V}\,\mathbf{S}^{-1}\,\mathbf{U}^T. \tag{4.12}$$

Accordingly, considering the relationship presented in (4.7) and the definition of the pseudoinverse, the estimate of the model parameters can be written as

$$\mathbf{p}_{\text{est}} = \mathbf{A}^+\,\mathbf{g}_{\text{est}} = \mathbf{V}\,\mathbf{S}^{-1}\,\mathbf{U}^T\,\mathbf{g}_{\text{obs}}. \tag{4.13}$$

In this methodology, regularization is introduced through the modification of the inversion of the singular values of the sensitivity matrix. Instead of directly using the inverse of each singular value, which would lead to a strong amplification of noise associated with singular values of small magnitude and cause numerical indeterminacies, a damping factor controlled by the regularization parameter λ is employed. This factor is applied to the diagonal elements of the matrix $\mathbf{S}^{-1}$, such that, for each singular value s_i, the regularized inversion is defined as

$$\frac{s_i}{s_i^2 + \lambda^2}.$$

This modification limits the contribution of small singular values to the solution, thereby reducing numerical instability.

4.3.3 Projected Gradient Method

Gravimetric inversion for the estimation of density contrasts associated with geological structures constitutes an inherently ill-posed inverse problem, characterized by non-uniqueness of the solution and sensitivity to noise present in the observational data. In addition, in geophysical applications it is often possible to incorporate a

priori geological information into the inversion process. Such information may be expressed, for example, through the imposition of physical bounds on the admissible values of the density contrast, contributing to the derivation of models that are more realistic and consistent with the geological context of the problem.

Classical unconstrained inversion methods, such as the direct least-squares solution, do not guarantee the satisfaction of these physical constraints and may therefore produce mathematically admissible but physically inconsistent models. In this context, the Projected Gradient Method emerges as a natural and efficient choice, as it allows the explicit treatment of constraints imposed on the model parameters while preserving the convexity of the optimization problem.

The Projected Gradient Method is based on the formulation of a regularized least-squares objective functional, defined as

$$\mathbf{J}(\mathbf{p}) = \| \mathbf{A}\mathbf{p} - \mathbf{g}_{\text{obs}} \|^2 + \lambda \, \mathbf{p}^T \Theta \, \mathbf{p}, \tag{4.14}$$

where the first term quantifies the misfit between the observed data and the data predicted by the model, whereas the second term corresponds to spatial smoothness regularization. The data misfit term can be expanded as

$$\| \mathbf{A}\mathbf{p} - \mathbf{g}_{\text{obs}} \|^2 = \mathbf{p}^T \mathbf{A}^T \mathbf{A}\mathbf{p} - 2\mathbf{p}^T \mathbf{A}^T \mathbf{g}_{\text{obs}} + \mathbf{g}_{\text{obs}}^T \, \mathbf{g}_{\text{obs}}, \tag{4.15}$$

which allows the objective functional to be rewritten in quadratic form as

$$\mathbf{J}(\mathbf{p}) = \mathbf{p}^T \left(\mathbf{A}^T \mathbf{A} + \lambda \, \Theta \right) \mathbf{p} - 2\mathbf{p}^T \mathbf{A}^T \mathbf{g}_{\text{obs}} + \mathbf{g}_{\text{obs}}^T \, \mathbf{g}_{\text{obs}}. \tag{4.16}$$

The exact gradient of the objective functional with respect to the model parameters is obtained by direct differentiation, yielding (Boyd and Vandenberghe, 2004)

$$\nabla \mathbf{J}(\mathbf{p}) = 2 \left[\left(\mathbf{A}^T \mathbf{A} + \lambda \, \Theta \right) \mathbf{p} - \mathbf{A}^T \mathbf{g}_{\text{obs}} \right]. \tag{4.17}$$

Based on physical considerations of the problem, box-type inequality constraints are imposed on the model parameters, such that $\mathbf{p}_{\min} \leq \mathbf{p} \leq \mathbf{p}_{\max}$. The presence of these constraints precludes the existence of a closed-form analytical solution and motivates the use of an iterative method capable of explicitly handling inequalities.

For this purpose, the Projected Gradient Method is adopted. At each iteration k, the method initially performs a descent step along the direction opposite to the gradient of the objective functional (Bertsekas, 1999; Nocedal and Wright, 2006), according to

$$\mathbf{p}^{k+1} = \mathbf{p}^k - \alpha_k \nabla \mathbf{J}(\mathbf{p}^k), \tag{4.18}$$

where α_k denotes the step length. For convex quadratic functionals, this step length can be determined analytically by means of an exact minimization along the gradient direction, resulting in

$$\alpha_k = \frac{\nabla \mathbf{J}(\mathbf{p}^k)^T \nabla \mathbf{J}(\mathbf{p}^k)}{2\nabla \mathbf{J}(\mathbf{p}^k)^T \left(\mathbf{A}^T\mathbf{A} + \lambda\,\Theta\right) \nabla \mathbf{J}(\mathbf{p}^k)}. \tag{4.19}$$

Subsequently, the updated parameter vector is orthogonally projected onto the admissible set defined by the inequality constraints, ensuring that all estimated parameters remain within the prescribed physical bounds throughout the entire iterative process.

4.4 Fluid Substitution

The production or injection of fluids in a reservoir induces changes in fluid saturation, which directly modifies the average density of the saturated rock. Variations in fluid content alter the effective bulk density of the porous medium, leading to a redistribution of subsurface mass. This mass redistribution produces measurable variations in the gravitational field at the surface, forming the physical basis for time-lapse gravimetric monitoring of reservoirs.

Assuming a porous medium composed of a solid rock matrix and pore fluids, the effective density of the saturated rock at time t can be expressed as

$$\rho_{\text{eff}}(t) = (1-\phi)\,\rho_{\text{matrix}} + \phi\left[S_w(t)\,\rho_w + S_o(t)\,\rho_o\right], \tag{4.20}$$

where ϕ denotes the porosity of the rock, $S_w(t)$ and $S_o(t)$ represent the water and oil saturations, respectively, and ρ_{matrix}, ρ_w, and ρ_o are the densities of the rock matrix, water, and oil. The saturation terms satisfy the constraint $S_w + S_o = 1$ for a two-phase system.

Temporal changes in fluid saturation, driven by injection or production processes, result in variations of $\rho_{\text{eff}}(t)$, which can be mapped into gravity changes through forward gravimetric modeling. Consequently, time-lapse gravimetry provides a non-invasive tool to monitor fluid migration and mass balance within hydrocarbon reservoirs.

4.4.1 Synthetic MATLAB reservoir model: water injection in an oil reservoir

The synthetic reservoir model was developed in MATLAB using the Automatic Differentiation modules of the MATLAB Reservoir Simulation Toolbox (MRST).

This framework enables the simulation of multiphase flow in porous media while ensuring numerical robustness and consistency in the solution of the governing flow equations.

The computational grid consists of $50 \times 50 \times 5$ cells, representing a three-dimensional domain of $8000 \times 8000 \times 60$ cubic meters. This discretization provides a compromise between spatial resolution and computational efficiency, allowing the capture of large-scale flow patterns and saturation changes within the reservoir.

A layered stratigraphy is imposed by assigning distinct permeability values to three vertical zones, representing heterogeneities commonly observed in sedimentary reservoirs. Here, "mD" denotes millidarcy, a unit of permeability commonly used in reservoir engineering ($1 \text{ mD} = 10^{-3}$ Darcy). The permeability distribution is defined as follows:

- 500 mD in the upper layer;
- 100 mD in the intermediate layer;
- 300 mD in the lower layer.

This configuration promotes preferential flow paths and vertical contrasts in fluid movement, which significantly influence the spatial distribution of saturation changes.

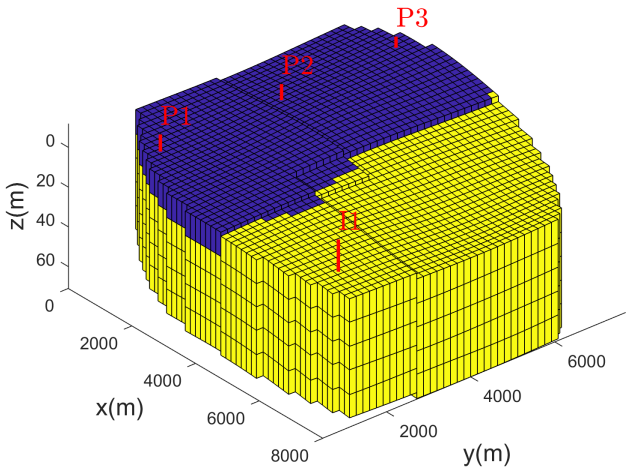

Figure 4.9: Synthetic reservoir model showing the spatial configuration of the grid and the location of injection and production wells. . Wells P_1, P_2, and P_3 correspond to production wells, where oil is extracted from the reservoir, while I_1 denotes the injection well, through which water is injected into the reservoir.

Figure 4.9 illustrates the initial fluid distribution, where blue prisms correspond to oil-containing regions and yellow prisms indicate water-saturated zones, as well as the location of the production wells P_1, P_2, and P_3 and the injection well I_1. Oil is extracted through the production wells, while water is simultaneously injected into the reservoir, progressively replacing it within the pore space. The resulting evolution of fluid saturation is shown in Figure 4.10, highlighting the propagation of the water front and its interaction with reservoir heterogeneities. For the physical modeling of the system, it is further assumed that the reservoir rock matrix has a density of $2650\,\mathrm{kg/m^3}$, while the oil and water exhibit densities of $700\,\mathrm{kg/m^3}$ and $1030\,\mathrm{kg/m^3}$, respectively.

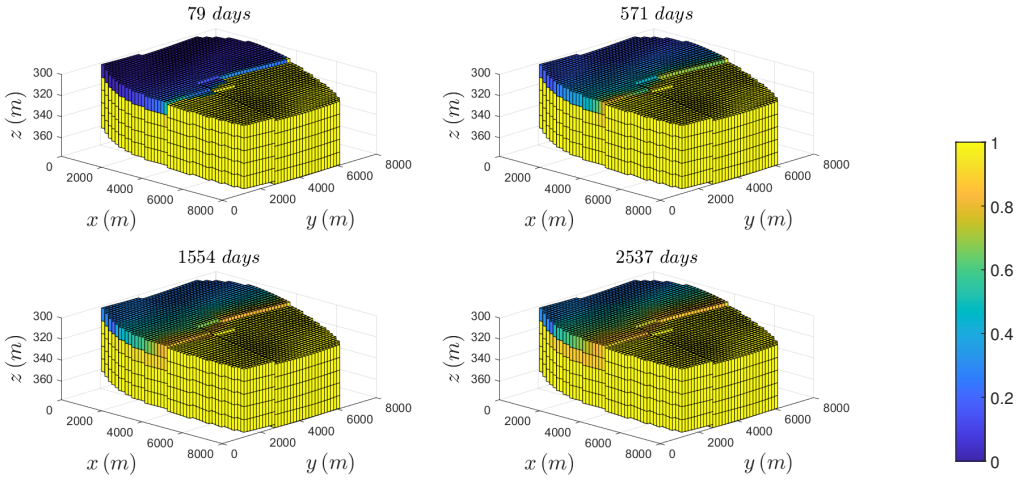

Figure 4.10: Water saturation distribution resulting from injection, obtained from the MRST simulation.

As the water and oil saturations evolve due to injection and production processes, the density distribution within the reservoir is progressively modified, in accordance with the expression defined in (4.20). The corresponding gravimetric response, computed through forward modeling using the time-dependent density distribution, is shown in Figure 4.11. The gravity signal exhibits localized anomalies associated with the injected water plume, with amplitudes on the order of microgals.

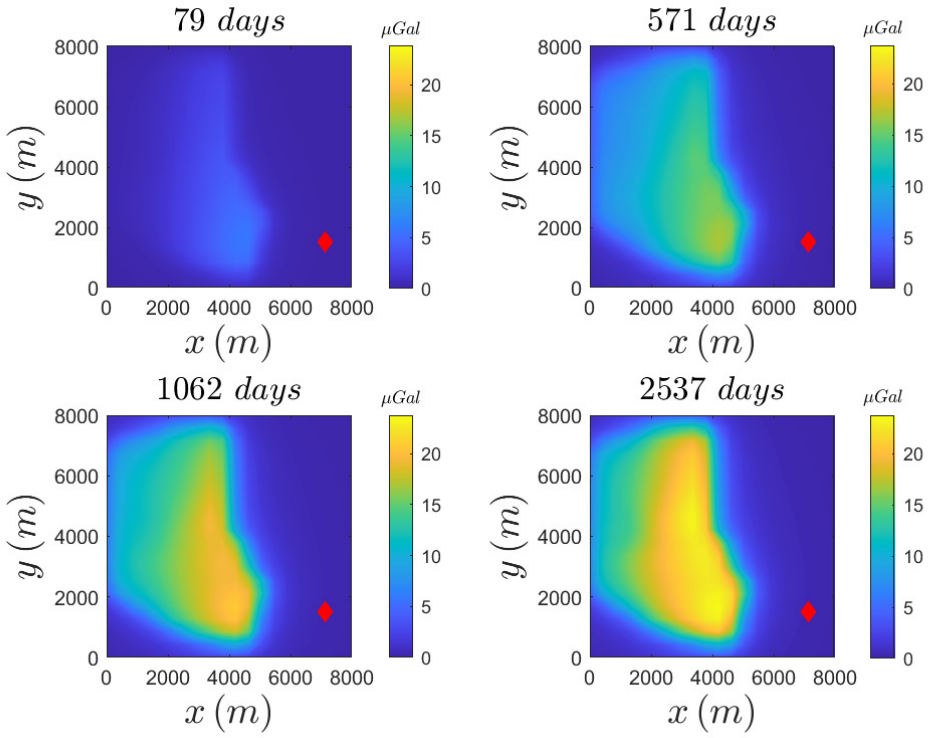

Figure 4.11: Variation in the gravimetric signal (in μGal) resulting from water injection into the reservoir. The red dot indicates the location of the injection well.

The variations observed in the gravimetric signal are directly related to the subsurface density distribution, as discussed in Section 4.3, and therefore contain information about the density structure of the subsurface medium. Figure 4.13 presents the density variation within the reservoir after 2537 days of fluid replacement, which is responsible for the variation in the gravimetric signal observed in the contour plot located in the lower right corner of Figure 4.11. It is observed that the amplitude of this variation is extremely small, on the order of μGal, which implies the need for gravimetric instruments of very high precision, as well as rigorous noise treatment, in order to reliably estimate density variations within the reservoir.

With the objective of assessing the feasibility of estimating density parameters, inversions were performed using two distinct methods: Tikhonov regularization and the generalized inverse. In addition, the gravimetric signal was contaminated with different noise levels in order to investigate the influence of noise on the estimates and to analyze the robustness of each method with respect to variations in the signal-

to-noise ratio.

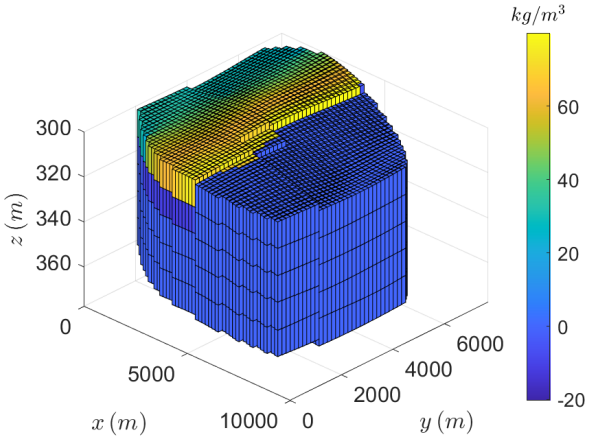

Figure 4.12: Density distribution within the reservoir after 2537 days of water injection into the reservoir.

Initially, both estimation methods were applied without contaminating the signal with noise (Figure 4.13). The results obtained from the two methods were similar, and it was possible to recover the overall shape of the density distribution shown in Figure 4.12. However, even in the absence of noise, a loss of amplitude is observed, indicating that the estimated parameter amplitudes are lower than the true values.

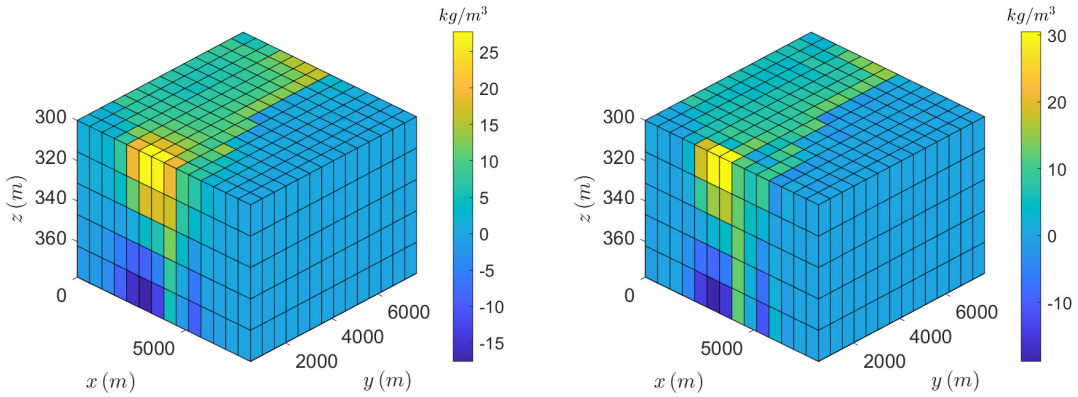

(a) (b) Estimated density (SVD)

Figure 4.13: Noise-free inversion results: (a) density estimated using Tikhonov regularization with a smoothness constraint, and (b) density estimated using the generalized inverse method.

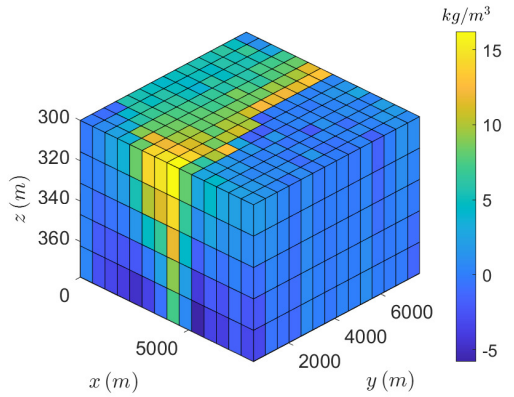

(a) Estimated density (smoothness constraint – $\lambda = 0.001$)

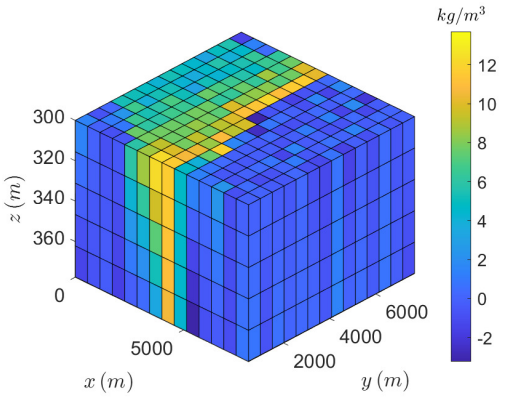

(b) Estimated density (SVD) – λ=0.5

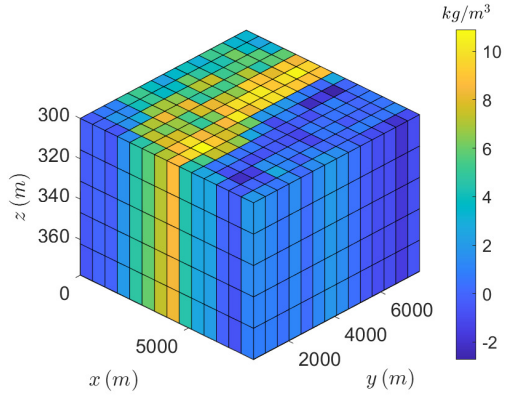

(c) Estimated density (smoothness constraint – $\lambda = 0.1$)

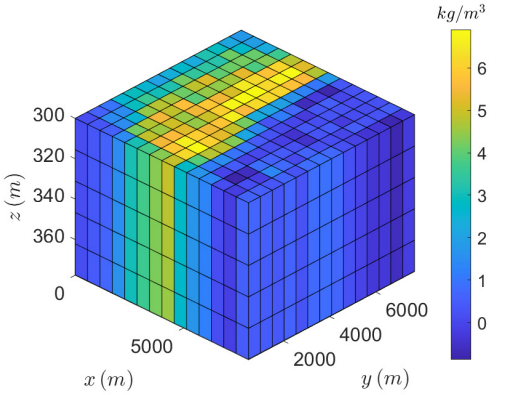

(d) Estimated density (SVD) – $\lambda = 1$

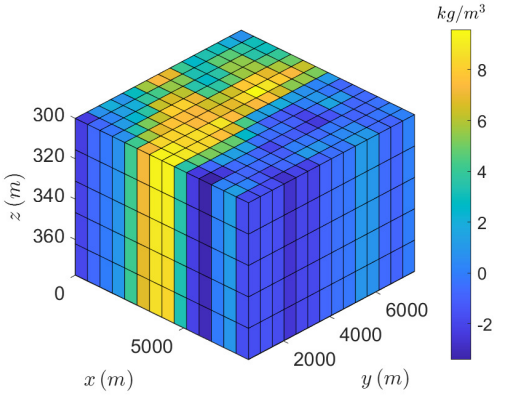

(e) Estimated density (smoothness constraint – $\lambda = 0.5$)

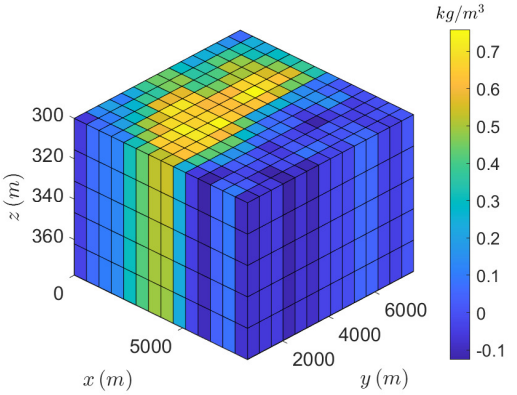

(f) Estimated density (SVD) – $\lambda = 5$

Figure 4.14: Estimated densities. In (a) and (b) the noise amplitude is $1\mu Gal$, (c) and (d) $10\mu Gal$, while in (e) and (f) $20\mu Gal$,

Figure 4.14 illustrates the estimated density distributions obtained using smoothness constrained Tikhonov regularization and Singular Value Decomposition (SVD) under increasing levels of gravimetric noise. Panels (a) and (b) correspond to a noise amplitude of 1 μGal, panels (c) and (d) to 10 μGal, and panels (e) and (f) to 20 μGal.

For the lowest noise level (1 μGal), both inversion strategies are able to recover the main features of the true density model. The smoothness-constrained solution (panel a) yields a spatially coherent density distribution with reduced high-frequency artifacts, while the SVD-based solution (panel b) preserves sharper contrasts but already exhibits localized oscillations associated with the amplification of small singular values.

As the noise level increases to 10 μGal (panels c and d), the impact of noise becomes more pronounced. The smoothness-regularized inversion requires a larger regularization parameter to stabilize the solution, resulting in increased smoothing and partial loss of resolution. In contrast, the SVD solution shows a stronger sensitivity to noise, with spurious oscillatory patterns emerging despite the increase in the truncation or damping level controlled by λ.

At the highest noise level (20 μGal), shown in panels (e) and (f), the degradation of the recovered density models is evident for both approaches. The smoothness-constrained inversion produces overly smoothed models that retain only the large-scale density trends, whereas the SVD-based solution becomes dominated by noise-induced artifacts, significantly compromising its physical interpretability.

These results demonstrate that the quality of density estimation in time-lapse gravimetric inversion is strongly dependent on the signal-to-noise ratio of the observations. They also highlight the critical role of regularization parameter selection, as increasing noise levels necessitate stronger stabilization at the expense of spatial resolution. In practical applications, this trade-off must be carefully balanced to ensure physically meaningful interpretations of subsurface density variations.

4.4.2 Kimberlina dataset: CO_2 storage

The Kimberlina dataset is a three-dimensional synthetic model developed to investigate and evaluate geophysical methods for monitoring geological CO_2 storage. This dataset is based on geological and hydrological information representative of the southern San Joaquin Basin, California (USA) (Alumbaugh et al., 2024).

The model represents a subsurface volume discretized into regular rectangular prisms, spanning approximately from -2 km to 4 km in the horizontal directions (x and y) and from 0 to 3.5 km in depth (z), with uniform spatial resolution. CO_2 injection is simulated over time within a deep reservoir, leading to time-dependent

variations in physical properties such as density, seismic velocity, and electrical resistivity. Based on these hydrological models, synthetic geophysical datasets are generated, including seismic, electromagnetic, and time-lapse gravity data, acquired both at the surface and in boreholes. The primary objective of the Kimberlina dataset is to provide a controlled and geologically realistic framework for the development, testing, and comparison of forward modeling and inversion methodologies applied to CO_2 reservoir monitoring.

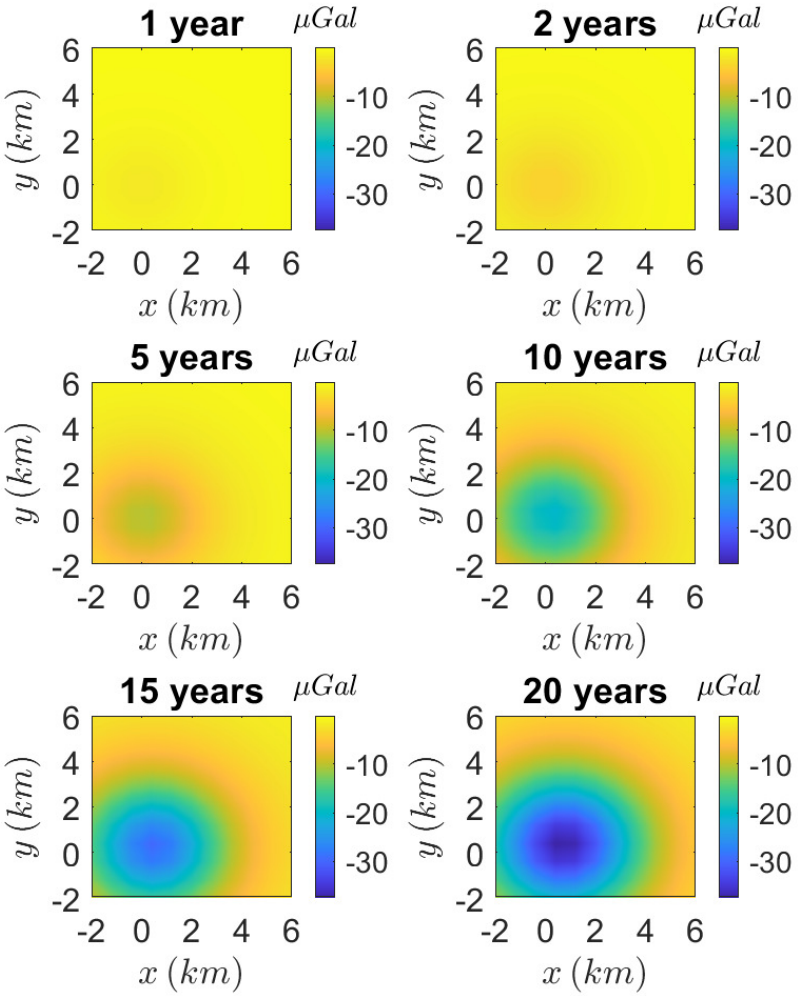

Figure 4.15: Gravimetric anomalies associated with CO_2 injection at different stages of reservoir evolution, corresponding to 1, 2, 5, 10, 15 and 20 years of injection.

Figure 4.15 presents the gravimetric anomalies calculated at the surface for different stages of reservoir evolution, corresponding to 1, 2, 5, 10, 15, and 20 years of CO_2 injection. The anomalies were obtained by applying Equation (4.1) to the density contrast models derived from saturation data provided in the "sim001_rhosat" dataset from the Kimberlina Data Set. A progressive development of a negative gravimetric anomaly over time is observed, in direct agreement with the increase in CO_2 saturation within the reservoir at each evaluated time step. This behavior is consistent with the replacement of denser fluids by CO_2, resulting in a local reduction of the average density and, consequently, in a negative gravimetric response.

The relationship between the gravimetric anomalies and the reservoir dynamics can be clearly established from Figure 4.16, which illustrates the spatial evolution of the CO_2 plume. During the initial stages of injection, the plume remains concentrated near the injection point. As time progresses, a gradual lateral spreading is observed, controlled by the properties of the medium, such as reservoir permeability.

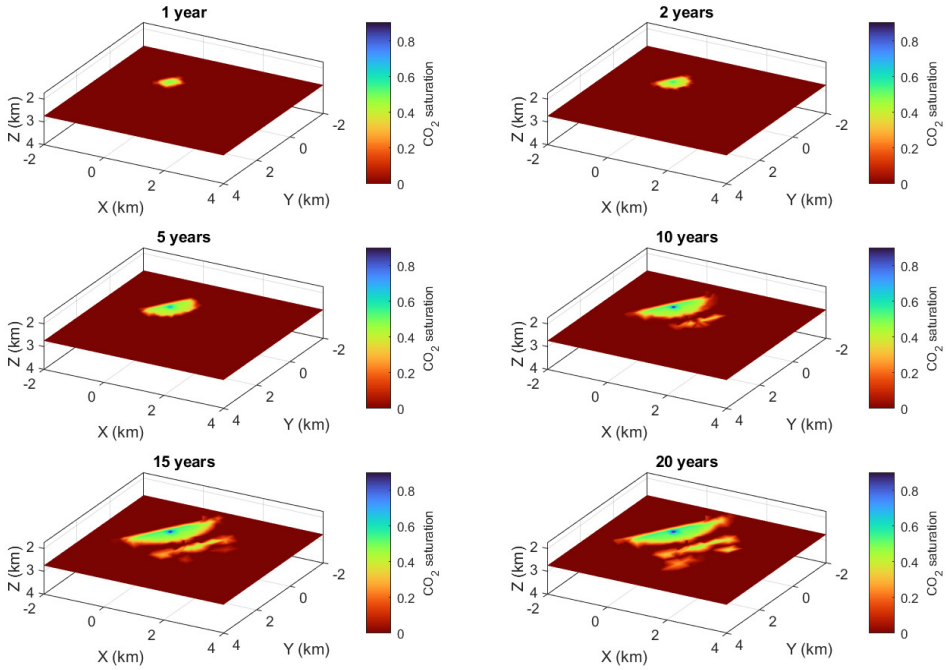

Figure 4.16: Horizontal slices of CO_2 saturation at a depth of 2.75 km, illustrating the spatial distribution of the plume after 1, 2, 5, 10, 15 and 20 years of injection.

According to Alumbaugh et al. (2024), the reservoir rock exhibits an approximate

thickness of 400 m in the vicinity of the injection well, with its upper boundary located at an average depth of about 2,750 m. Therefore, for the estimation of the density distribution associated with CO_2 injection, the first assumption adopted was that the reservoir could be adequately represented by a simplified single-layer model, discretized into 576 parameters.

For the estimation of these parameters, the *Projected Gradient Method* was applied, incorporating a spatial smoothness constraint and inequality constraints on the model parameters. Specifically, the estimated density contrasts were constrained to the interval

$$-500 \leq \mathbf{p}_{\text{est}} \leq 0,$$

ensuring that the parameters remain negative and confined within a physically plausible range, consistent with the replacement of denser fluids by CO_2. This constraint guarantees that the obtained solutions are both numerically stable and physically consistent with the geological context of the problem.

Figures 4.17, 4.19, and 4.21 present the density contrast models estimated from the inversion of gravimetric data contaminated, respectively, with Gaussian noise amplitudes of 1 μGal, 10 μGal, and 20 μGal. In all cases, the estimates corresponding to 1, 2, 5, 10, 15, and 20 years of injection are shown.

In the scenario with 1 μGal noise (Figure 4.17), an excellent recovery of the overall geometry of the density anomaly associated with the CO_2 plume is observed, particularly for injection times greater than 5 years (Figure 4.18). In all evaluated periods, it was possible to estimate a negative density contrast in the injection region. However, for years 1 and 2, the lateral extent of the estimated plume is not fully consistent with the reference model, presenting an affected area larger than expected. For the remaining periods, the spatial growth trend of the negative anomaly is consistent with the reference models, indicating that, for a noise level of 1 μGal, gravimetric inversion is capable of providing robust and physically coherent images of reservoir evolution over time.

Additionally, it is noteworthy that the inversion process converged for all evaluated periods. For each temporal stage, distinct regularization parameters were adopted and adjusted to ensure numerical stability and physical consistency of the solution, with values of 4.0, 0.7, 0.006, 0.004, 0.004, and 0.004, corresponding, respectively, to the years 1, 2, 5, 10, 15, and 20.

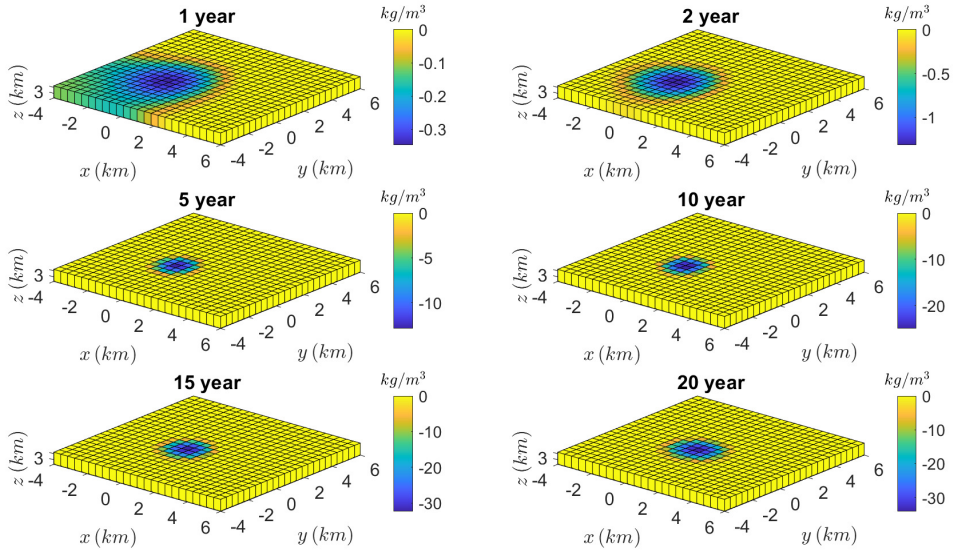

Figure 4.17: Density contrast estimates obtained from gravimetric observations contaminated by Gaussian noise with an amplitude of 1 μGal, for different injection durations: 1, 2, 5, 10, 15, and 20 years.

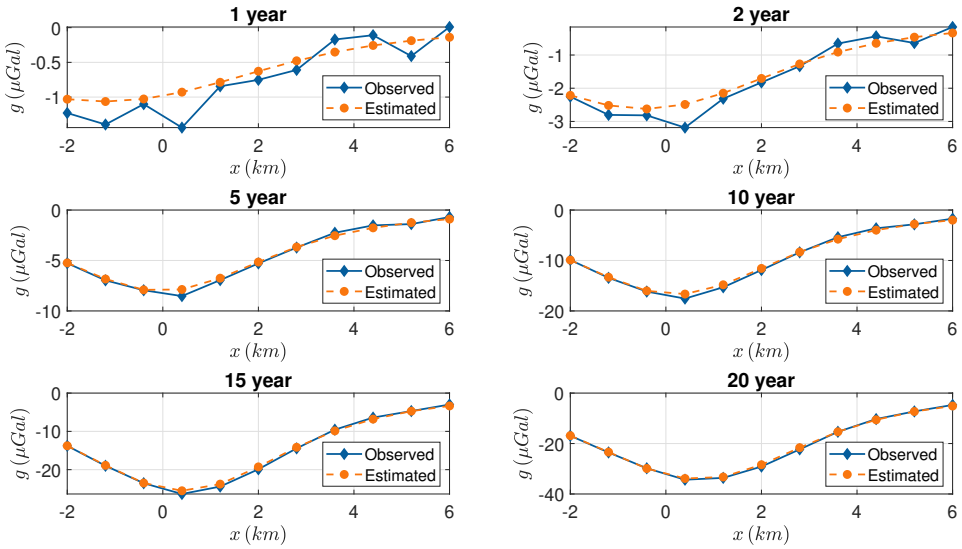

Figure 4.18: Comparison between observed and estimated gravity anomalies along a horizontal profile at $y = 1.2$ km, for different injection durations (1, 2, 5, 10, 15, and 20 years). The estimated responses are computed from the inverted density models obtained from gravimetric data contaminated with additive Gaussian noise of 1 μGal.

When the noise level is increased to 10 μGal (Figure 4.19), a significant degradation in the recovery of the density contrast distribution is observed, particularly for the periods corresponding to 1, 2, 5, and 10 years of injection. In these cases, the reduction in spatial resolution and the underestimation of the maximum estimated contrast become evident. During the early stages of injection, the gravimetric anomaly becomes more diffuse and partially masked by noise, hindering accurate identification of the CO_2 plume geometry.

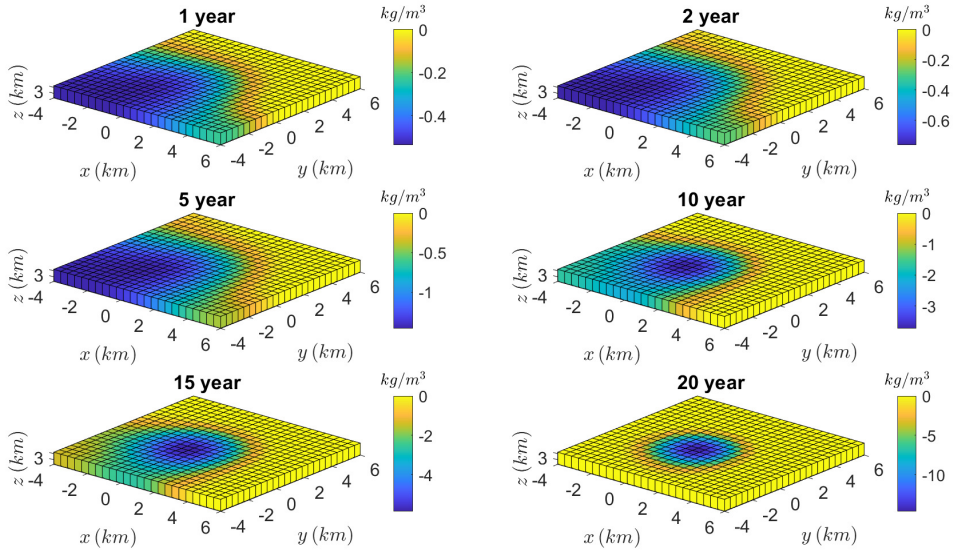

Figure 4.19: Density contrast estimates obtained from gravimetric observations contaminated by Gaussian noise with an amplitude of 10 μGal, for different injection durations: 1, 2, 5, 10, 15, and 20 years.

For injection times greater than 10 years, the main signature of the plume remains identifiable, although with strong spatial smoothing. This behavior is directly reflected in the mismatch between observed and estimated data, as illustrated in Figure 4.20, and is associated with the lack of convergence or numerical instability of the inversion solution for the first four evaluated periods.

For the noise level of 20 μGal (Figure 4.21), convergence of the inversion solutions was not achieved, even with the adoption of elevated regularization parameters exceeding 40.0. This behavior is a direct consequence of the high noise amplitude relative to the amplitude of the gravimetric anomaly associated with CO_2 injection, which prevents the extraction of physically coherent geophysical information, particularly during the early stages of injection.

As a result, when partially stable solutions are obtained, the estimated responses tend to exhibit significantly reduced amplitudes and a high degree of spatial smoothing, reflecting the limitations imposed by the elevated noise level. Nevertheless, for the scenario corresponding to 20 years of injection, the main signature of the gravimetric anomaly can be partially recovered, indicating that only density contrasts accumulated over long periods remain detectable under this noise regime.

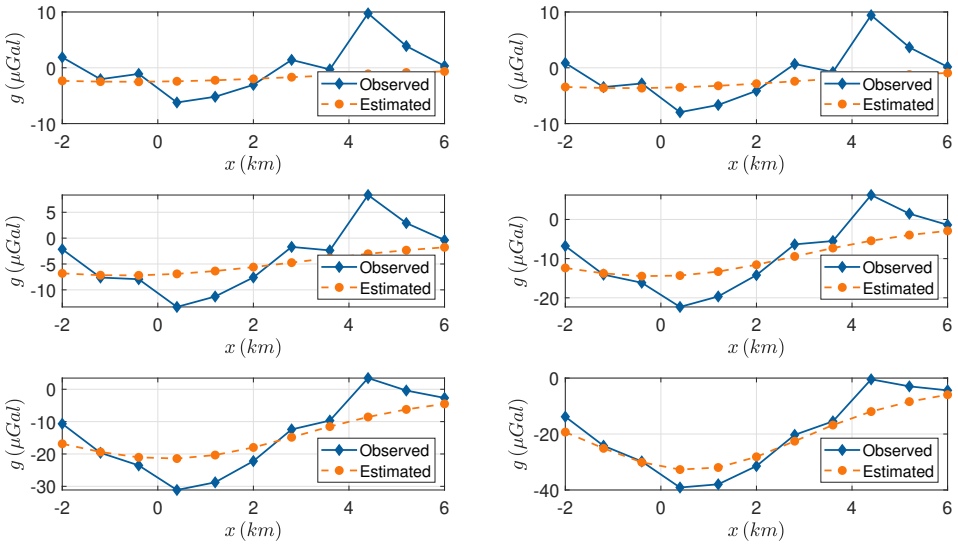

Figure 4.20: Comparison between observed and estimated gravity anomalies along a horizontal profile at $y = 1.2$ km, for different injection durations (1, 2, 5, 10, 15, and 20 years). The estimated responses are computed from the inverted density models obtained from gravimetric data contaminated with additive Gaussian noise of 10 μGal.

Overall, the results demonstrate that the feasibility of gravimetric monitoring of CO_2 reservoirs is strongly dependent on the noise level of the data. Noise levels on the order of 1 μGal allow a robust and physically coherent characterization of reservoir evolution, whereas intermediate noise levels, around 10 μGal, restrict detection to more advanced stages of injection. Conversely, higher noise levels prevent the application of gravimetry for quantitative purposes. These results reinforce the importance of gravimetric instruments with high stability and sensitivity for long-term monitoring applications, highlighting the potential of quantum gravimeters as promising tools for geophysical studies associated with geological CO_2 storage.

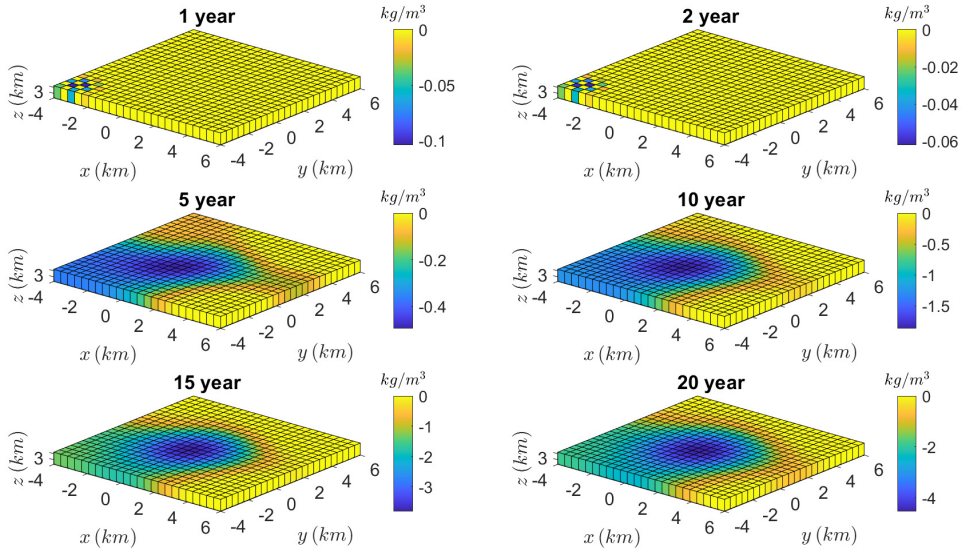

Figure 4.21: Density contrast estimates obtained from gravimetric observations contaminated by Gaussian noise with an amplitude of 20 μGal, for different injection durations: 1, 2, 5, 10, 15, and 20 years.

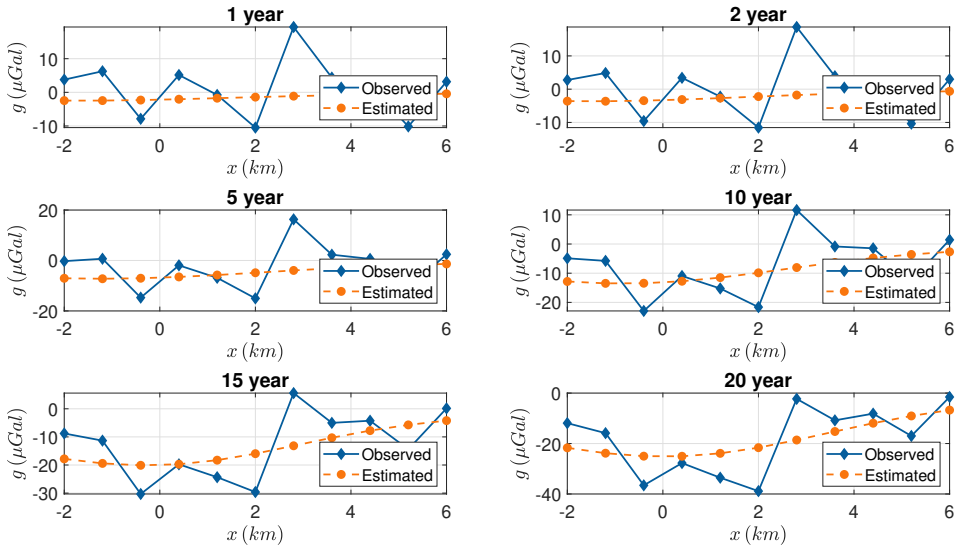

Figure 4.22: Comparison between observed and estimated gravity anomalies along a horizontal profile at $y = 1.2$ km, for different injection durations (1, 2, 5, 10, 15, and 20 years). The estimated responses are computed from the inverted density models obtained from gravimetric data contaminated with additive Gaussian noise of 20 μGal.

4.4.3 Implications for quantum gravimetry in geophysical monitoring

The results presented in the previous sections demonstrate that gravimetric signals associated with 4D reservoir monitoring exhibit extremely small amplitudes, typically on the order of a few microgals. This characteristic imposes stringent requirements on data quality, since the amplitude of instrumental and environmental noise must be comparable to or lower than that of the signal in order to extract geophysically meaningful information. This dependence was evidenced by the numerical experiments discussed previously, in which increases in noise level resulted in a substantial degradation of the estimated density parameters.

In this context, instrumental drift emerges as a critical limiting factor for high-sensitivity gravimetric applications. In relative gravimeters, the presence of drift requires frequent calibration through repeated measurements at base stations, where the gravity value is assumed to be known or stable. Although this procedure is essential to ensure the temporal consistency of the observations, it imposes significant

operational limitations, such as increased acquisition time, the need for frequent instrument relocation, and the introduction of additional uncertainties associated with the applied corrections.

This limitation is particularly relevant for spring-based gravimeters, which typically exhibit relatively high drift rates. For example, in the study of Braitenberg et al. (2016), conducted using a spring gravimeter, a drift on the order of 12 μGal per hour was reported. This limitation becomes especially evident when the magnitude of the gravimetric signal associated with the Kimberlina dataset is considered. As illustrated in Figure 4.23, gravity variations induced by fluid injection over a period of up to 20 years reach maximum amplitudes on the order of 30–35 μGal. It is further observed that, during the early stages of the process, corresponding to the first years of injection, the variations in g are restricted to only a few microgals. In this context, an instrumental *drift* of approximately 12 μGal h^{-1}, such as that reported by Braitenberg et al. (2016) for spring gravimeters, would be sufficient to completely mask the gravimetric signal of interest on time scales of only one hour. Even when the long-term evolution of the reservoir is considered, the accumulated drift amplitude becomes comparable to the total gravity variation observed over several decades of injection, thereby significantly compromising the reliable estimation of density parameters and the physical interpretation of fluid substitution processes.

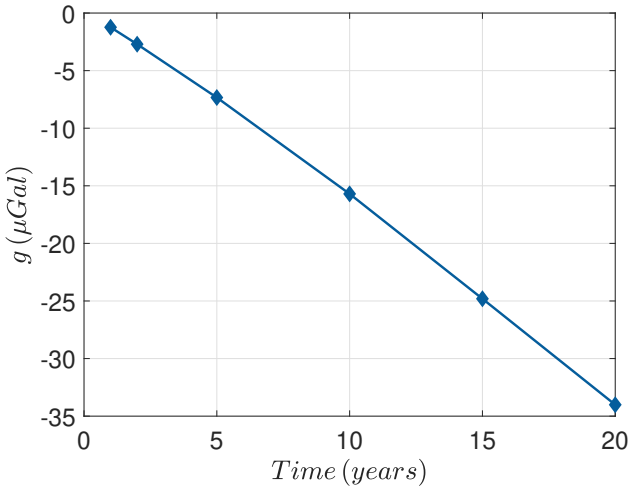

Figure 4.23: Temporal evolution of the gravity variation (Δg) induced by fluid injection in the Kimberlina model, evaluated at the observation point located at $(x, y) = (1.2 \text{ km}, 1.2 \text{ km})$.

Among relative gravimeters, the instrument that exhibits the greatest long-term

stability is the superconducting gravimeter. Long-term observations, such as those carried out with the iGrav-043, indicate that the instrumental drift in these devices is characterized by a composite behavior consisting of an initial phase of exponential relaxation followed by an approximately linear trend, with rates on the order of tens of nm s^{-2} per year. This behavior is consistent with the theoretical model of instrumental drift for superconducting gravimeters proposed by Hinderer et al. (2022), which was used to generate the drift curve presented in Figure 4.24. According to this model, a superconducting gravimeter would require approximately 1500 days to accumulate a drift on the order of 20 μGal. Despite this high stability and very high sensitivity, these instruments still require periodic calibration, although less frequently than spring gravimeters.

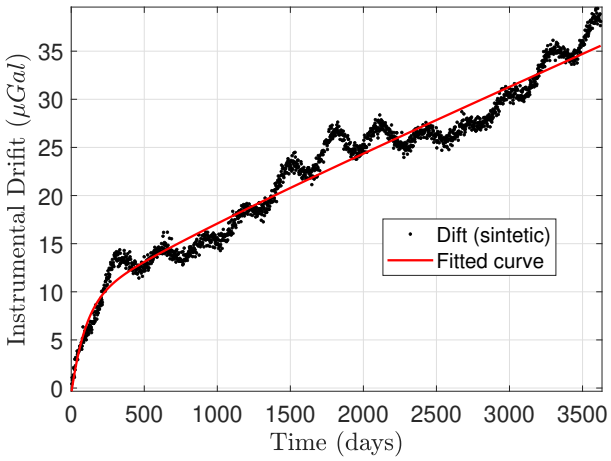

Figure 4.24: Synthetic instrumental drift over time (black dots) and the corresponding fitted curve (red line), representing the long-term trend observed in superconducting gravimeters. The drift is modeled as a slow component, following the metrological approach adopted in Hinderer et al. (2022).

In addition, superconducting gravimeters are designed for continuous operation at fixed stations, which constitutes an important practical limitation. This characteristic prevents their use in mobile campaigns or field surveys, restricting their application to permanent observatories. In contrast, quantum gravimeters are absolute instruments based on atom interferometry and are not subject to the classical drift mechanisms associated with mechanical components. This characteristic represents a decisive advantage in real geophysical applications, particularly in 4D gravimetry studies, in which subtle temporal variations must be detected and interpreted

reliably.

Therefore, the combination of absolute measurement capability, low instrumental drift, and high sensitivity makes quantum gravimeters particularly well suited for geophysical problems that require microgal-level precision over long time scales. The results of this study reinforce the conclusion that quantum gravimetry represents a promising – and in many cases necessary – technological advancement for the quantitative monitoring of subsurface density variations associated with fluid substitution and geological CO_2 storage.

Recent advances in atom interferometry further expand the geophysical potential of quantum gravimeters by enabling the simultaneous measurement of gravity acceleration and vertical gravity gradients using differential interferometric configurations without significant additional hardware complexity. As demonstrated in Janvier et al. (2022), dual-cloud or spatially separated atomic ensembles can be interrogated within the same experimental apparatus, allowing direct estimation of gravity gradients through differential phase measurements while preserving the intrinsic stability of absolute atom interferometry. This capability is particularly relevant for geophysical inversion problems, since gravity gradient information enhances spatial resolution and reduces non-uniqueness in density reconstruction (Capriotti and Li, 2021). In the context of 4D reservoir monitoring, the incorporation of gradient measurements could improve the sensitivity of the inversion to density contrasts and mitigate the ambiguity associated with regional trends. Therefore, beyond their intrinsic stability and absolute character, quantum gravimeters equipped with gradient measurement capability offer a framework for improving the robustness and reliability of gravity-based subsurface imaging.

Conclusions

This Thesis explored the physical principles, sensitivity analysis, and geophysical applicability of quantum gravimeters based on atom interferometry. The objective was to provide a description accessible to both physicists and geoscientists.

In addition, the geophysical context in which gravimetric measurements are applied was addressed, and it was demonstrated how gravity data can be quantitatively related to subsurface density variations. Starting from the physical basis of gravimetry, the relationship between geological structures and gravimetric anomalies was discussed, emphasizing the role of density contrasts associated with different lithologies and fluid distributions.

Forward gravimetric modeling based on rectangular prism discretization was presented as a fundamental tool for establishing the connection between subsurface density distributions and the observed gravity field. The analytical formulation of the gravitational response of prismatic elements highlighted the linear nature of the gravimetric problem and provided the basis for subsequent inversion strategies. Through simple numerical experiments, it was shown how the amplitude of gravimetric anomalies decays with depth, illustrating the intrinsic limitations imposed by instrumental sensitivity.

The inversion of gravimetric data was formulated as a linear inverse problem. Two widely used regularization approaches were investigated in the context of the MRST model: Tikhonov regularization with the imposition of a smoothness constraint, and the generalized inverse based on singular value decomposition. Synthetic inversion experiments demonstrated that, although both methods are capable of recovering the large-scale features of the true density model under low-noise conditions, their performance progressively degrades as the noise level increases.

In addition, for the case of the Kimberlina synthetic data set, the iterative Projected Gradient Method was applied to estimate the model parameters within predefined bounds. Similarly to what was observed for the MRST model, the results of this second experiment indicated that, in the CO_2 injection problem—which is characterized by extremely small variations in the gravimetric field—even minor noise

perturbations are sufficient to mask the cumulative effect of several years of injection. Consequently, as the noise component becomes more dominant in the signal, the ability to extract physically meaningful information from gravity measurements is significantly reduced.

The inversion results highlighted the stringent requirements on instrumental precision and noise control necessary to reliably interpret such small-amplitude signals. These resultsreinforce the relevance of high-sensitivity gravimetric instruments for four-dimensional geophysical studies.

The analysis demonstrated that the absolute measurements provided by quantum gravimeters may represent a significant advantage over conventional relative gravimeters, particularly for applications requiring long observation times or the detection of low-frequency gravitational signals. The investigation of noise contributions highlighted the importance of understanding the temporal structure of the measurement and the role of different noise sources in limiting sensitivity. A comparative analysis of classical and quantum gravimeters demonstrated that improvements in sensitivity directly translate into increased detectability of deep or low-density-contrast targets. In particular, the higher sensitivity and absolute measurement capability of quantum gravimeters extend the depth range over which subsurface bodies can be detected, compared to conventional spring gravimeters.

The role of instrumental drift was discussed as a major limitation in long-term gravimetric monitoring when using relative gravimeters. The fact that quantum gravimeters operate as absolute measurement instruments constitutes a significant advantage. Moreover, when compared with classical spring–mass gravimeters, quantum gravimeters exhibit superior long-term temporal stability. In terms of sensitivity, the only relative instrument that surpasses the sensitivity of quantum gravimeters is the superconducting gravimeter. However, the latter presents an important limitation, as it is designed to operate at fixed measurement stations, which restricts its applicability as a portable instrument.

In conclusion, quantum gravimeters emerge as versatile instruments for geophysical applications, offering improvements in accuracy, stability, and interpretability of gravity measurements. As these sensors continue to mature technologically and become more widely available, they are expected to play a significant role in future studies of the Earth's interior, environmental monitoring, and space-based gravity missions.

Bibliography

Allan, D., 1966, Statistics of atomic frequency standards: Proceedings of the IEEE, **54**, 221–230.

Alumbaugh, D., E. Gasperikova, D. Crandall, M. Commer, S. Feng, W. Harbert, Y. Li, Y. Lin, and S. Samarasinghe, 2024, The kimberlina synthetic multiphysics dataset for co2 monitoring investigations: Geoscience Data Journal, **11**, 216–234.

Antoni-Micollier, L., M. Arnal, R. Gautier, C. Janvier, V. Ménoret, J. Richard, P. Vermeulen, P. Rosenbusch, C. Majek, and B. Desruelle, 2024, Absolute quantum gravimeters and gradiometers for field measurements: IEEE Instrumentation & Measurement Magazine, **27**, 4–10.

Arzi, A., 2006, Microgravimetry for engineering applications. geophys prospect: Geophysical Prospecting, **23**, 408 – 425.

Barbosa, V. C. F., J. B. C. Silva, and W. E. Medeiros, 1999, Gravity inversion of a discontinuous relief stabilized by weighted smoothness constraints on depth: Geophysics, **64**, 1429–1437.

Bertsekas, D., 1999, Nonlinear programming: Athena Scientific.

Bhardwaj, K., S. Singh, S. P. Ram, B. Jain, V. Kumar, A. Pathak, S. Tiwari, V. B. Tiwari, and S. R. Mishra, 2024, Measurement of gravitational acceleration in a single laser operated atomic fountain. (arXiv preprint arXiv:2405.04223. https://arxiv.org/abs/2405.04223).

Bidel, Y., N. Zahzam, A. Bresson, C. Blanchard, A. Bonnin, J. Bernard, M. Cadoret, T. Jensen, R. Forsberg, C. Salaun, S. Lucas, M. Lequentrec-Lalancette, D. Rouxel, G. Gabalda, L. Seoane, D. Vu, S. Bruinsma, and S. Bonvalot, 2023, Airborne absolute gravimetry with a quantum sensor, comparison with classical technologies: Journal of Geophysical Research: Solid Earth, **128**.

Blakely, R. J., 1995, Potential theory in gravity and magnetic applications.

Bowin, C., 1991, The earth's gravity field and plate tectonics: Tectonophysics, **187**, 69–89. (Silver Anniversary of Plate Tectonics).

Boyd, S. P., and L. Vandenberghe, 2004, Convex optimization: IEEE Transactions on Automatic Control, **51**, 1859–1859.

Braitenberg, C., and A. Pastorutti, 2024, Detectability of seamount eruptions through a quantum technology gravity mission mocast+: Hunga tonga, fani maoré and other smaller eruptions: Surveys in Geophysics, **45**, 1331–1361.

Braitenberg, C., D. Sampietro, T. Pivetta, D. Zuliani, A. Barbagallo, P. Fabris, L. Rossi, J. Fabbri, and A. H. Mansi, 2016, Gravity for detecting caves: Airborne and terrestrial simulations based on a comprehensive karstic cave benchmark: Pure and Applied Geophysics, **173**.

Capriotti, J., and Y. Li, 2021, Joint inversion of gravity and gravity gradient data: A systematic evaluation: GEOPHYSICS, **87**, 1–93.

Cavendish, H., 1798, Xxi. experiments to determine the density of the earth: Philosophical Transactions of the Royal Society of London, 469–526.

Cheinet, P., B. Canuel, F. Pereira Dos Santos, A. Gauguet, F. Yver-Leduc, and A. Landragin, 2008, Measurement of the sensitivity function in a time-domain atomic interferometer: IEEE Transactions on Instrumentation and Measurement, **57**, 1141–1148.

Chen, G., T. Liu, J. Sun, Q. Cheng, B. Sahoo, Z. Zhang, and H. Zhang, 2015, Gravity method for investigating the geological structures associated with w–sn polymetallic deposits in the nanling range, china: Journal of Applied Geophysics, **120**, 14–25.

Chen, J., 2023, Analysis of the principle and state-of-art facilities of mobile atom interferometry gravity: Highlights in Science, Engineering and Technology, **72**, 511–521.

Chu, S., 2001, Atom interferometry: Coherent atomic matter waves, Springer Berlin Heidelberg, 317–370.

Cohen-Tannoudji, C., B. Diu, and F. Laloë, 1977, Quantum mechanics: Wiley. (Trans. of : Mécanique quantique. Paris : Hermann, 1973).

Cooke, A.-K., C. Champollion, and N. Le Moigne, 2021, First evaluation of an absolute quantum gravimeter (aqg#b01) for future field experiments: Geoscientific Instrumentation, Methods and Data Systems, **10**, 65–79.

Dirac, P. A. M., 1930, The principles of quantum mechanics, 1st ed.: Oxford University Press.

Doyle, H. A., 1990, Geophysical exploration for gold; a review: Geophysics, **55**, 134–146.

Exail, 2023, Absolute quantum gravimeter: Technical brochure, Exail. (Accessed: 2025-01-18).

———, 2025, Exail – empowering critical missions: https://www.exail.com/. (Accessed: 8 December 2025).

Fang, J., W. Wang, Y. Zhou, J. Li, D. Zhang, B. Tang, J. Zhong, J. Hu, F. Zhou,

X. Chen, J. Wang, and M. Zhan, 2024, Classical and atomic gravimetry: Remote Sensing, **16**, 2634.

Feynman, R., A. Hibbs, and D. Styer, 2010, Quantum mechanics and path integrals: Dover Publications. Dover Books on Physics.

Foot, C. J., 2007, Atomic physics: Oxford University Press. Oxford master series in atomic, optical, and laser physics.

Freier, C., M. Hauth, V. Schkolnik, B. Leykauf, M. Schilling, H. Wziontek, H.-G. Scherneck, J. Müller, and A. Peters, 2016, Mobile quantum gravity sensor with unprecedented stability: Journal of Physics: Conference Series, **723**, 012050.

Glässel, J., H. Wziontek, E. Antokoletz, E. Brachmann, R. Falk, and J. Müller, 2025, Evaluation of the exail absolute quantum gravimeters aqg-a02 and aqg-b10 by comparison to a precise gravity reference: Journal of Geodesy, **99**, 73.

Goodkind, J. M., 1999, The superconducting gravimeter: Review of Scientific Instruments, **70**, 4131–4152.

Griffiths, D. J., 2018, Introduction to quantum mechanics (2nd international edition), 2nd ed.: Pearson.

Gutenberg, B., 1914, über erdbebenwellen [on seismic waves]: Nachrichten von der Gesellschaft der Wissenschaften zu Göttingen, Mathematisch-Physikalische Klasse, 125–176. (In German. Title translation: On seismic waves).

Hinderer, J., R. Warburton, S. Rosat, U. Riccardi, J.-P. Boy, F. Forster, P. Jousset, A. Güntner, K. Erbas, F. Littel, and J.-D. Bernard, 2022, Intercomparing superconducting gravimeter records in a dense meter-scale network at the j9 gravimetric observatory of strasbourg, france: Pure and Applied Geophysics, **179**, 1701–1727.

Jackson, J. D., 1999, Classical electrodynamics, 3rd ed. ed.: Wiley.

Janvier, C., V. Ménoret, B. Desruelle, S. Merlet, A. Landragin, and F. Pereira dos Santos, 2022, Compact differential gravimeter at the quantum projection-noise limit: Phys. Rev. A, **105**, no. 2, 022801.

Junior, I. R. D. S., A. Trombettoni, and C. Braitenberg, 2026, Ultracold quantum gravimeters: An introduction for geophysicists.

Kasevich, M., and S. Chu, 1991, Atomic interferometry using stimulated raman transitions: Phys. Rev. Lett., **67**, no. 2, 181–184.

Kok, P., 2018, A first introduction to quantum physics: Springer International Publishing. Undergraduate Lecture Notes in Physics.

Kumar, M., 2011, Melting glaciers can change earth's gravity field: Eos, Transactions American Geophysical Union, **92**, 324–324.

Kusche, J., C. Strohmenger, H. Gerdener, B. Uebbing, A. Springer, Y. Ewerdwalbesloh, A. Eicker, C. Braitenberg, A. Pastorutti, R. Pail, P. Zingerle, M. Schlaak, M. Reguzzoni, L. Rossi, F. Migliaccio, and I. Daras, 2025, Benefit of

magic and multipair quantum satellite gravity missions in earth science applications: Geophysical Journal International, **242**.

Lafehr, T., 1980, Gravity method: Geophysics, **45**, 1634–1639.

Lamporesi, G., A. Bertoldi, L. Cacciapuoti, M. Prevedelli, and G. M. Tino, 2008, Determination of the newtonian gravitational constant using atom interferometry: Physical Review Letters, **100**.

Le Gouët, J., T. Mehlstäubler, J. Kim, S. Merlet, A. Clairon, A. Landragin, and F. Pereira Dos Santos, 2008, Limits to the sensitivity of a low noise compact atomic gravimeter: Applied Physics B, **92**, 133–144.

LeDesma, C., K. Mehling, and M. Holland, 2025, Vector atom accelerometry in an optical lattice: Science Advances, **11**, eadt7480.

Love, A. E. H., 1911, Some problems of geodynamics: Cambridge University Press.

Micro-g LaCoste, 2024, A-10 portable absolute gravity meter.

Miffre, A., M. Jacquey, M. Büchner, G. Trénec, and J. Vigué, 2006, Vibration-induced phase noise in mach–zehnder atom interferometers: Applied Physics B, **84**, 617–625.

Migliaccio, F., M. Reguzzoni, K. Batsukh, G. M. Tino, G. Rosi, F. Sorrentino, C. Braitenberg, T. Pivetta, D. F. Barbolla, and S. Zoffoli, 2019, Mocass: A satellite mission concept using cold atom interferometry for measuring the earth gravity field: Surveys in Geophysics, **40**, 1029–1053.

Migliaccio, F., M. Reguzzoni, G. Rosi, C. Braitenberg, G. M. Tino, F. Sorrentino, S. Mottini, L. Rossi, Ö. Koç, K. Batsukh, T. Pivetta, A. Pastorutti, and S. Zoffoli, 2023, The MOCAST+ Study on a Quantum Gradiometry Satellite Mission with Atomic Clocks: Surveys in Geophysics, **44**, 665–703.

Mohieldain, A. A., M. Dobróka, M. A. Mohammed, and N. P. Szabó, 2025, Gravity-based structural and tectonic characterization of the shendi-atbara basin, central sudan: Journal of African Earth Sciences, **225**, 105571.

Müller, J., and H. Wu, 2020, Using quantum optical sensors for determining the earth's gravity field from space: Journal of Geodesy, **94**.

Ménoret, V., P. Vermeulen, N. Le Moigne, S. Bonvalot, P. Bouyer, A. Landragin, and B. Desruelle, 2018, Gravity measurements below 10-9 g with a transportable absolute quantum gravimeter: Scientific Reports, **8**.

Nabighian, M. N., M. E. Ander, V. J. S. Grauch, R. O. Hansen, T. R. LaFehr, Y. Li, W. C. Pearson, J. W. Peirce, J. D. Phillips, and M. E. Ruder, 2005, Historical development of the gravity method in exploration: Geophysics, **70**, 63ND–89ND. (Geology, Geophysics, and Geochemistry Science Center).

Nagy, D., G. Papp, and J. Benedek, 2000, The gravitational potential and its derivatives for the prism: Journal of Geodesy, **74**, 552–560.

Niebauer, T., 2007, Gravimetric methods – absolute gravimeter: Instruments concepts and implementation, *in* Treatise on Geophysics: Elsevier, 43–64.

Nocedal, J., and S. Wright, 2006, Numerical optimization: Springer New York. Springer Series in Operations Research and Financial Engineering.

Orszag, M., 2024, *in* Atom–Field Interaction: Semiclassical Approach: Springer International Publishing, 13–23.

Pendiuk, J., M. F. Degano, L. Guarracino, and R. E. Rivas, 2023, Superconducting gravimeters: A novel tool for validating remote sensing evapotranspiration products: Hydrology, **10**.

Peres, A., 1995, Quantum theory: Concepts and methods: Springer, volume **57** *of* Fundamental Theories of Physics.

Perez-Gracia, V., S. Fontul, S. assunção, and V. Marecos, 2016, *in* Geophysics: Fundamentals and Applications in Structures and Infrastructure: CRC Press, 59–88.

Peters, A., K. Y. Chung, and S. Chu, 2001, High-precision gravity measurements using atom interferometry: Metrologia, **38**, 25.

Pethick, C., and H. Smith, c2008, Bose-einstein condensation in dilute gases / c. j. pethick, h. smith, 2. ed ed.: Cambridge University Press.

Pettersen, B. R., 2016, A historical review of gravimetric observations in norway: History of Geo- and Space Sciences, **7**, 79–89.

Pitaevskij, L. P., and S. Stringari, 2016, Bose-einstein condensation and superfluidity / lev pitaevskii, sandro stringari, reprinted with corrections ed.: Oxford University Press. The international series of monographs on physics.

Pivetta, T., C. Braitenberg, and A. Pastorutti, 2022, Sensitivity to mass changes of lakes, subsurface hydrology and glaciers of the quantum technology gravity gradients and time observations of satellite mocast+: Remote Sensing, **14**, 4278.

Reich, E. S., 2010, G-whizzes disagree over gravity: Nature, **466**, 1030.

Riley, W., and D. Howe, 2008, Handbook of frequency stability analysis.

Romeshkani, M., J. Müller, A. Knabe, and M. Schilling, 2025, Quantum gravimetry for future satellite gradiometry: Advances in Space Research, **75**, 1653–1664.

Rossi, L., M. Reguzzoni, Ö. Koç, G. Rosi, and F. Migliaccio, 2023, Assessment of gravity field recovery from a quantum satellite mission with atomic clocks and cold atom gradiometers: Quantum Science and Technology, **8**, 014009.

Rovny, J., Z. Yuan, M. Fitzpatrick, A. I. Abdalla, L. Futamura, C. Fox, M. C. Cambria, S. Kolkowitz, and N. P. de Leon, 2022, Nanoscale covariance magnetometry with diamond quantum sensors: Science, **378**, 1301–1305.

Rubiola, E., 2008, Phase noise and frequency stability in oscillators: Cambridge University Press. The Cambridge RF and Microwave Engineering Series.

Sakurai, J. J., and J. Napolitano, 2020, Modern quantum mechanics, 3 ed.: Cam-

bridge University Press.

Schilling, M., É. Wodey, L. Timmen, D. Tell, K. Zipfel, D. Schlippert, C. Schubert, E. Rasel, and J. Müller, 2020, Gravity field modelling for the hannover 10 m atom interferometer: Journal of Geodesy, **94**.

Schrödinger, E., 1983, The present situation in quantum mechanics, *in* Quantum Theory and Measurement: Princeton University Press, 152–167. (English translation of "Die gegenwärtige Situation in der Quantenmechanik" (1935)).

Scintrex, 2019, CG-6 Autograv Survey Gravity Meter. Scintrex Limited. (Accessed: 2025-12-01).

Scully, M. O., and M. S. Zubairy, 1997, Quantum optics: Cambridge University Press.

Shankar, R., 1980, Principles of quantum mechanics: Plenum.

Smith, R. J., 1985, Geophysics in australian mineral exploration: Geophysics, **50**, 2637–2665.

Sorrentino, F., Q. Bodart, L. Cacciapuoti, Y.-H. Lien, M. Prevedelli, G. Rosi, L. Salvi, and G. M. Tino, 2014, Sensitivity limits of a raman atom interferometer as a gravity gradiometer: Physical Review A, **89**.

Storey, P., and C. Cohen-Tannoudji, 1994, The feynman path integral approach to atomic interferometry: A tutorial: Journal de Physique II, **4**, 1999–2027.

Sun, H., X. Chen, H. Houtze, and W. Yong, 2001, Accurate determination of calibration factor for tidal gravity observation of a gwr-superconducting gravimeter: **23**, 657–658.

Tan, X., Q. Wang, J. Feng, Y. Huang, and Z. Huang, 2021, Fast modeling of gravity gradients from topographic surface data using gpu parallel algorithm: Geodesy and Geodynamics, **12**, 288–297.

Teixeira, W., T. R. Fairchild, M. C. M. d. Toledo, and F. Taioli, 2009, Decifrando a terra, 2 ed.: Oficina de Textos.

Telford, W., L. Geldart, and R. Sheriff, 1990, Applied geophysics: Cambridge University Press.

Tikhonov, A. N., and V. Y. Arsenin, 1977, Solutions of ill-posed problems: V. H. Winston & Sons. (Translated from the Russian, Preface by translation editor Fritz John, Scripta Series in Mathematics).

Tinsley, J. N., 2019, Construction of a rubidium fountain atomic interferometer for gravity gradiometry: PhD thesis, University of Liverpool. (DOI: https://doi.org/10.17638/03046742).

Villalobos, M., A. Avila-Forcada, and M. Gutiérrez ruiz, 2008, An improved gravimetric method to determine total petroleum hydrocarbons in contaminated soils: Water Air and Soil Pollution, **194**, 151–161.

Wang, G., Y. Wei, and S. Qiao, 2018, *in* Equation Solving Generalized Inverses: Springer Singapore, 1–64.

Weng, K., Y. Zhou, D. Zhu, K. Wang, B. Wu, B. Cheng, and Q. Lin, 2021, High-accuracy gravity measurement with miniaturized quantum gravimeter: SCIENTIA SINICA Physica, Mechanica & Astronomica, **51**, 74204.

Wu, X., Z. Pagel, G. D'Amico, M. Prevedelli, F. Sorrentino, Q. Bodart, L. Amand, K. Bongs, and M. A. Kasevich, 2019, Gravity surveys using a mobile atom interferometer: Science Advances, **5**, eaax0800.

Young, B., M. Kasevich, and S. Chu, 1997, Precision atom interferometry with light pulses, *in* Atom Interferometry: Academic Press, 363–406.

Zemp, M., L. Jakob, I. Dussaillant, S. Nussbaumer, N. Gourmelen, S. Dubber, G. Aa, S. Abdullahi, L. M. Andreassen, E. Berthier, A. Bhattacharya, A. Blazquez, L. Vock, T. Bolch, J. Box, M. Braun, F. Brun, E. Cicero, W. Colgan, and W. Zheng, 2025, Community estimate of global glacier mass changes from 2000 to 2023: Nature, **639**.

Zingerle, P., M. Romeshkani, J. Haas, T. Gruber, A. Güntner, J. Müller, and R. Pail, 2024, The benefits of future quantum accelerometers for satellite gravimetry: Earth and Space Science, **11**, e2024EA003630.

Appendix A

Eigenvectors of $\hat{H}_R$

The eigenvectors corresponding to the Hamiltonian

$$\hat{H}_R = \frac{\hbar}{2}\begin{pmatrix} -\delta & \Omega_{ba}\, e^{-i\phi} \\ \Omega_{ba}^{*}\, e^{+i\phi} & +\delta \end{pmatrix} \tag{A.1}$$

are determined, with eigenvalues $\lambda_{\pm} = \pm\frac{\hbar\Omega_R}{2}$.

The eigenvector $|\lambda_+\rangle = \begin{pmatrix} a \\ b \end{pmatrix}$, associated with the eigenvalue $\lambda_+ = +\frac{\hbar\Omega_R}{2}$, satisfies the eigenvalue equation:

$$\left(\hat{H}_R - \lambda_+ \boldsymbol{I}\right)|\lambda_+\rangle = \mathbf{0}. \tag{A.2}$$

Thus,

$$\begin{pmatrix} -(\delta+\Omega_R) & \Omega_{ba}\, e^{-i\phi} \\ \Omega_{ba}^{*}\, e^{+i\phi} & (\delta-\Omega_R) \end{pmatrix}\begin{pmatrix} a \\ b \end{pmatrix} = \begin{pmatrix} 0 \\ 0 \end{pmatrix}. \tag{A.3}$$

Consequently,

$$b = \frac{\Omega_R+\delta}{\Omega_{ba}}\, e^{+i\phi}\, a \tag{A.4}$$

From Eq. (A.10), we obtain

$$b = \sqrt{\frac{\Omega_R+\delta}{\Omega_R-\delta}}\, e^{+i\phi}\, a. \tag{A.5}$$

Considering Eqs. (3.17), and using the trigonometric half-angle identities, we have:

$$\sin\frac{\theta}{2} = \sqrt{\frac{\Omega_R+\delta}{2\,\Omega_R}}, \qquad \cos\frac{\theta}{2} = \sqrt{\frac{\Omega_R-\delta}{2\,\Omega_R}} \tag{A.6}$$

Therefore,

$$b = \frac{\sin\frac{\theta}{2}}{\cos\frac{\theta}{2}}\, e^{+i\phi}\, a \tag{A.7}$$

and the eigenvector $|\lambda_+\rangle$ can be written as:

$$|\lambda_+\rangle = \begin{pmatrix} a \\ b \end{pmatrix} = \frac{a e^{+i\frac{\phi}{2}}}{\cos\frac{\theta}{2}} \begin{pmatrix} \cos\frac{\theta}{2}\, e^{-i\frac{\phi}{2}} \\ \\ \sin\frac{\theta}{2}\, e^{+i\frac{\phi}{2}} \end{pmatrix} \tag{A.8}$$

(with a fixed by the normalization).

To determine the eigenvector $|\lambda_-\rangle$, we use the same procedure with the eigenvalue equation given by $\left(\hat{H}_R - \lambda_- \boldsymbol{I}\right)|\lambda_-\rangle = \mathbf{0}$, from which

$$-b = \frac{\Omega_R - \delta}{\Omega_{ba}}\, e^{+i\phi}\, a \tag{A.9}$$

and

$$-b = \sqrt{\frac{\Omega_R - \delta}{\Omega_R + \delta}}\, e^{+i\phi}\, a. \tag{A.10}$$

and $b = -\frac{\cos\frac{\theta}{2}}{\sin\frac{\theta}{2}}\, e^{+i\phi}\, a$. Therefore, with a fixed by the normalization, the eigenvector $|\lambda_-\rangle$ can be expressed as:

$$|\lambda_-\rangle = \begin{pmatrix} a \\ b \end{pmatrix} = -\frac{a e^{+i\frac{\phi}{2}}}{\sin\frac{\theta}{2}} \begin{pmatrix} -\sin\frac{\theta}{2}\, e^{-i\frac{\phi}{2}} \\ \\ \cos\frac{\theta}{2}\, e^{+i\frac{\phi}{2}} \end{pmatrix} \tag{A.11}$$

Appendix B

Phase Arising from the Classical Action (S_{Cl})

When one considers the propagation of a particle from a position x_a at time t_a to a position x_b at time t_b, the wave function associated with this motion can be described by the quantum propagator. This propagator, $K(x_b, t_b; x_a, t_a)$, contains all the information about the system and describes how the wave function evolves between the points x_a and x_b. This evolution is governed by the evolution operator $U(t_b, t_a)$, acting on the wave function at the initial time t_a, it yields the wave function at the later time t_b:

$$|\psi(x_b, t_b)\rangle = U(t_b, t_a)\,|\psi(x_a, t_a)\rangle.$$

To project this equation onto the position basis, one applies the projection of the state $|\psi(x_b, t_b)\rangle$ onto the position eigenstates $|x_b\rangle$:

$$\langle x_b|\psi(x_b, t_b)\rangle = \langle x_b|U(t_b, t_a)\,|\psi(x_a, t_a)\rangle.$$

For the completeness relation $\mathbf{I} = \int dx_a |x_a\rangle\langle x_a|$, the previous expression can be rewritten as

$$\langle x_b|\psi(x_b, t_b)\rangle = \langle x_b|U(t_b, t_a)\,|x_a\rangle\langle x_a|\psi(x_a, t_a)\rangle.$$

Defining the propagator as

$$K(x_b, t_b; x_a, t_a) = \langle x_b|U(t_b, t_a)|x_a\rangle,$$

the equation that expresses the wave function $\psi(x_b, t_b)$ in terms of the propagator is then given by

$$\psi(x_b, t_b) = \int dx_a\, K(x_b, t_b; x_a, t_a)\,\psi(x_a, t_a).$$

Within the framework of Feynman path integrals, the propagator can be interpreted as a sum over all possible paths Γ connecting the points (x_a, t_a) and (x_b, t_b) (Shankar, 1980; Feynman et al., 2010):

$$K(x_b, t_b; x_a, t_a) = \mathcal{N} \sum_{\Gamma} e^{\frac{i}{\hbar} S(\Gamma)},$$

where $S(\Gamma)$ denotes the classical action associated with the path Γ,

$$S = \int_{t_a}^{t_b} L(x, \dot{x})\, dt,$$

is the action with L the Lagrangian of the system, and $\mathcal{N}$ is a normalization factor.

In the semiclassical regime, characterized by $S \gg \hbar$, the path integral is dominated by classical trajectories. As a consequence, the evolution of the wave function can be approximated by

$$\psi(x_b, t_b) \simeq e^{\frac{i}{\hbar} S_{\mathrm{cl}}}\, \psi(x_a, t_a), \tag{B.1}$$

where S_{cl} is the action evaluated along the classical trajectory connecting the two events. Eq. (B.1) indicates that the wave function at the point (x_b, t_b) can be approximated by the wave function at the point (x_a, t_a) multiplied by a phase factor associated with the classical action, $e^{iS_{\mathrm{cl}}/\hbar}$. Thus, the phase associated with the atomic trajectory is

$$\Delta_{\mathrm{path}} = \frac{S_{\mathrm{cl}}}{\hbar}.$$

UNIVERSITÀ
DEGLI STUDI
DI TRIESTE

La borsa di dottorato è cofinanziata con risorse dell'Unione europea, NextGeneration EU - Piano Nazionale di Ripresa e Resilienza, Missione 4 – Componente 2 – Investimento 3.3 CUP J93C22001510006